Normandie Université

THÈSE

Pour obtenir le diplôme de doctorat

Spécialité MECANIQUE DES FLUIDES, ENERGETIQUE, THERMIQUE, COMBUSTION, ACOUSTIQUE

Préparée au sein de l'Université de Rouen Normandie

Analysis of liquid sheet thickness and perforation kinematics using conventional and time-gated optical diagnostics

Présentée et soutenue par
DILIP SUNIL SANADI

Thèse soutenue le 23/09/2022 devant le jury composé de		
M. YANNICK BAILLY	PROFESSEUR DES UNIVERSITES, UNIVERSITE BESANCON FRANCHE COMTE	Rapporteur du jury
M. HENDA DJERIDI	PROFESSEUR DES UNIVERSITES, INP (Grenoble)	Rapporteur du jury
MME CAMILLE HESPEL	MAITRE DE CONFERENCES, UNIVERSITE ORLEANS	Membre du jury
M. LOIC MÉÈS	CHARGE DE RECHERCHE, ECOLE CENTRALE LYON	Membre du jury
M. FABIEN THIESSET	CHARGE DE RECHERCHE, Université de Rouen Normandie	Membre du jury
MME FRANÇOISE BAILLOT	PROFESSEUR DES UNIVERSITES, Université de Rouen Normandie	Président du jury
M. JEAN-BERNARD BLAISOT	PROFESSEUR DES UNIVERSITES, Université de Rouen Normandie	Directeur de thèse

Thèse dirigée par JEAN-BERNARD BLAISOT (COMPLEXE DE RECHERCHE INTERPROFESSIONEL EN AEROTHERMOCHIMIE)

UNIVERSITÉ DE ROUEN NORMANDIE

ED 591 PSIME

CORIA UMR 6614

Normandie Université

THÈSE

Pour obtenir le diplôme de doctorat

Spécialité MECANIQUE DES FLUIDES, ÉNERGETIQUE, THERMIQUE, COMBUSTION, ACOUSTIQUE

Préparée au sein de l'Université de Rouen Normandie

Analysis of liquid sheet thickness and perforation kinematics using conventional and time-gated optical diagnostics

Présentée et soutenue par
Dilip Sunil SANADI

Thèse soutenue le 23/09/2022 devant le jury composé de		
M. YANNICK BAILLY	Professeur des Universités, Université de Besançon Franche Comté	Rapporteur du jury
MME. HENDA DJERIDI	Professeure des Universités, INP Grenoble	Rapporteuse du jury
MME. FRANÇOISE BAILLOT	Professeure des Universités, Université de Rouen Normandie	Membre du jury
MME. CAMILLE HESPEL	Maître de Conférences, Université d'Orléans	Membre du jury
M. LOÏC MEES	Chargé de recherche, CNRS, Ecole Centrale Lyon	Membre du jury
M. FABIEN THIESSET	Chargé de recherches, CNRS, Université de Rouen Normandie	Membre du jury
M. JEAN-BERNARD BLAISOT	Professeur des Universités, Université de Rouen Normandie	Directeur de thèse

Thèse dirigée par Jean-Bernard BLAISOT et co-encadrée par Fabien THIESSET, laboratoire CORIA (UMR 6614 CNRS)

UNIVERSITÉ DE ROUEN NORMANDIE

ED 591 PSIME

CORIA UMR 6614

Acknowledgments

I am very happy to have got this opportunity to thank all those known and unknown people who have directly or indirectly, contributed to the final shape of this work.

First and foremost, I express my utmost gratitude to the director of CORIA laboratory, Prof. Armelle Cessou, not only for giving me the opportunity to work here but also for creating a wonderful lab environment and relaxed intellectual atmosphere. I am equally thankful to the secretary of laboratory, Valerie Lequesne, Christophe Letailleur, Florence Fradet, Nathalie Delahaye and Theirry Bessac, who took appropriate care of all the paperwork that allowed me to focus on the research. I would also like to thank IT department,especially Cedric Chamberlan and Alexis Boulet who were always available to fix the computer related issues. I express my heartfelt gratitude to members of the workshop of CORIA – especially Benjamin Quevreux, Bruno Mille, Romain Guillot, and Thierry Muller for their timely help in installations of experimental setup and for building various kinds of optical mounts which were required for experiments included in this work; members of the metrology and instrumentation group – especially Gilles Godard, Alexandre poux, Franck Lefebvre and Alexandre Robcis who made sure that all the instruments in the lab function properly at all times. It was this excellent administration and keen cooperation among the members that led to which have facilitated the success of my work on a daily basis.

I am extremely thankful to the jury members who devoted their precious time to my thesis and came all the way to Rouen for my PhD defense. I am highly obliged to Prof. Henda Djeridi of the Institut polytechnique de Grenoble and Prof. Yannick Bailly of the Universite de Franche Comte UFC- UFR France, for an in-depth review of my thesis and their insightful comments about my work. I am full of gratitude and heartily thank Prof. Francoise Baillot of the Universite de Rouen, Dr. Loic Mees of the Ecole Centrale de Lyon, and Camille Hespel of the Universite d'orleans, for examining my work and their thoughtful suggestions for its further improvement.

I am overwhelmed with reverence and do not find words to pay my esteemed respect and deep gratitude to my two supervisor Prof.Jean-Bernard Blaisot and Dr. Fabien Thiesset without whose affectionate guidance, invaluable support, encouragement and utmost help, I would have not even survived in France, let alone my research. I am blessed that I got academic genealogy of both of them. In my mind, I consider Prof. Jean-Bernard Blaisot as my academic father and Dr. Thiesset as my academic elder brother. Their deep knowledge, sustained interest, meticulous observations, subtle criticism and timely advice were the motivating force that guided me throughout this work. In moments of extreme testing and challenge, they provided me the best possible solace and comfort- perhaps the manner in which only a father or elder brother can interface with his son or younger brother. I will never forget the sessions of brain-storming meeting

that we used to have every week Thursday, these sessions will really be missed. It has been a great pleasure working with both of you Sir and I hope that I will have your support and guidance in future as well.

I am extremely grateful to my esteemed colleague, Dr. Said Idlahcen, his self-less help during experiments helped me to learn, think and implement. His experience, understanding and personal guidance has provided a very strong basis for this work. Every time I used to get amazed with his Brain and hand coordination during the experiments. I really admire his sharp observations and valuable criticism, something that motivated my pace and passion to work harder.

It is with deep sense of gratitude and respect that I express my thanks to Prof. Christophe Dumouchel and Dr.Marie-Charlotte Renault for all the support, help, motivation and fruitful discussions from time to time played a pivotal role in this work.

Life at CORIA would have been incomplete without the presence of dear friends - Michael Ovando, Kuppuraj, Chetan, Clement Petat, Jose, Teodor,Mohamed, Rafael, Leandro and Rajlaxmi. I would like to make a special mention to my office-mate Michael Ovando, for his selfless help. I gratefully acknowledge the frequent discussions I had with Michael during the entire research work. I would also like to thank Chetan Vegad for helping me with the experiments. My dear friend Dr. Kuppuraj needs a special mention, who is a remarkable person and a great friend. Through countless discussions during this stay at Rouen, he helped me to make my life easier at Rouen. Special thanks to all my friends from outside the lab Late Santanu (Passed away in October 2021), Vikram, Lalit, Ankur, Maeva, Yanne, Hasna and Abhishek for their support and encouragement to embark on this beautiful and enriching journey at CORIA.

Last but not the least; The role of my family is too big to be acknowledged in so less words. I dedicate my work and all that I have achieved so far in life to my parents. I would like to thank my parents, for all the support, encouragement and consistent belief in me throughout my stay at France. I am thankful to my elder brother Deepak, and younger sister Sonali for their love and guidance in both good and bad times.

Contents

List of Tables

List of Figures

Nomenclature

Multiphase flows

We	Liquid Weber number based on hydraulic diameter of nozzle
We_h	Liquid Weber number based on thickness
$2\alpha_t$	Sheet expansion angle
λ_{opt}	Wavelength of sheet instability at ω_{max}
$\langle D \rangle$	Average diameter of ligaments
ω	Growth rate of instability
$\overline{U_c}$	Mean convection velocity of the hole
ρ	Density of the concerned liquid
σ	Surface tension of the concerned liquid
θ_s	Jet impingement angle
Bo	Liquid Bond number
Fr	Liquid Froude number
h	Liquid sheet thickness
K	Thickness parameter
Oh	Ohnesorge number
P_i	Injection pressure
Q	Flow rate
r_c	radius of curvature
R_s	Taylor radius of circular sheet
Re	Liquid Reynolds number
U_b	Liquid bulk velocity
u_p	Taylor-Culick speed
w	Tangential velocity of liquid along the rim
z	streamwise distance from nozzle exit
z_0	distance from virtual origin to nozzle exit
z_d	centroid vertical position of hole

Optics

χ	Susceptibility order of light
λ	Wavelength of the light
E	Electric field of light
P	Electric polarization field of light
ν	Frequency of the light
θ	Angle between imaging and gating pulse
θ_n	Angle between imaging and gating pulse inside BBO crystal
$\vec{k}_1, \vec{k}_2$	Wave vectors of SHG signal

C_{mag} Magnification Factor

d_{eff} Effective nonlinear optical coefficient

K_{cal} Calibration optical constant

N Number of passes of the imaging pulse

n Refractive index of air

n_{BBO} Refractive index of BBO

n_l Refractive index of concerned liquid

x, y Optical axis coordinates

$\Delta\tau^{\text{delay}}$ Time delay obtained by adjusting delay line

$\Delta\tau^{\text{Object}}$ Time delay computed between object and air

Δx^{camera} Spatial shift computed between object and air on camera

Δx^{delay} Spatial shift obtained by adjusting delay line

Constants

c Speed of light in vacuum

k_B Boltzmann constant

T_l Liquid temperature

Geometrical

$2a$ Major axis of nozzle orifice

$2b$ Minor axis of nozzle orifice

ϵ Inter-hole distance between perforation

ϵ_h Circularity of perforation

$\vec{n}, \vec{s}$ Unit vectors

A Area of nozzle

A_p Area of perforation

D_h Hydraulic diameter of nozzle

P Perimeter of nozzle

P_p Perimeter of perforation hole

r_{eq}^{A} A_p based radius of hole

r_{eq}^{P} P_p based radius of hole

Image processing

$\eta(\nu)$ Frequency Fourier transform

κ Shot to shot correction factor

C Contrast of image

I_b Background image

I_m Raw image

I_n Normalized image

I_o Obscurity image

$N_{background}$ Normalization factor for image

Statistics

μ_x, μ_y Position of maximum of 2d Gaussian distribution

$\overline{h}$ Mean liquid sheet thickness

σ_x, σ_y Dispersion of 2d Gaussian distribution

Θ Rotation angle of 2d Gaussian distribution

A Amplitude of Gaussian distribution

h_{rms} rms liquid sheet thickness

N_{im} Number of images

$\sigma_{\overline{I}}$ Mean standard error associated with mean intensity

Abbreviations

BBO beta Barium Borate, β-BaB_2B_4

CCD charge-coupled device

fs femto-second

FWHM Full width half maxima

HgCdTe Mercury admium telluride

LISTD Laser Induced Surface Tension Driven flows

L Linear

MR Momentum flux ratio

NL Non-linear

OD Optical depth

OKE optical Kerr effect

ps pico-second

rms Root mean square

ROI Region of interest

semi Semi-theoretical

SE Standard error

SLIPI Structured laser illumination planar imaging

STD Standard deviation

theo Theoretical

THz – TDS Terahertz time-domain spectroscopy

CS_2 liquid carbon disulfide

Introduction

General overview

Many industrial processes, domestic applications and natural phenomena involve two-phase flows, i.e flows revealing at least 2 immiscible phases separated by an interface. Liquid/gas flows are generally found as dispersed phases or sprays, rather than as continuous flows [32–34]. At sufficiently high injection velocity, such flows reveal liquid volumes emanating from the atomizer in the form of liquid sheets or jets, which disintegrate into to a myriad of ligaments, successively breaking-up into a stream of dispersed droplets in a gaseous atmosphere. This process of successive disintegration of a bulk liquid flow into a stream of drops is referred to as liquid atomization. To emphasize the importance of this process, we list a number of situations taken from various fields. As we will discuss, in all these situations, the drop-size distribution plays a key role in the efficiency of the process.

(A) ***Liquid propulsion, liquid fuel combustion***: The 26th session of the Conference of the Parties (COP26) to the United Nations Framework Convention on Climate [35] has been held in the Scottish Event Campus (SEC) in Glasgow, UK (from 31 October to 12 November 2021). With the aim of establishing a new international climate agreement, participating governments have tried to agree to limit carbon emission and keep global warming below 2^o C. Figure 2 shows a global increase in the surface temperatures since 1984 [10]. Global warming is mainly due to excessive greenhouse gas (GHG) emission. Many chemical compounds present in Earth's atmosphere behave as greenhouse gases, the primary GHG are, carbon dioxide (CO_2), nitrous oxide (N_2O), methane (CH_4), water vapor (H_2O), plerfluorcarbons (PFCs), hydrofluorocarbons (HFCs). Atmospheric concentrations of both the natural and anthropic gases have been rising over the last few centuries due to the industrial revolution. As the global population has increased and our reliance on

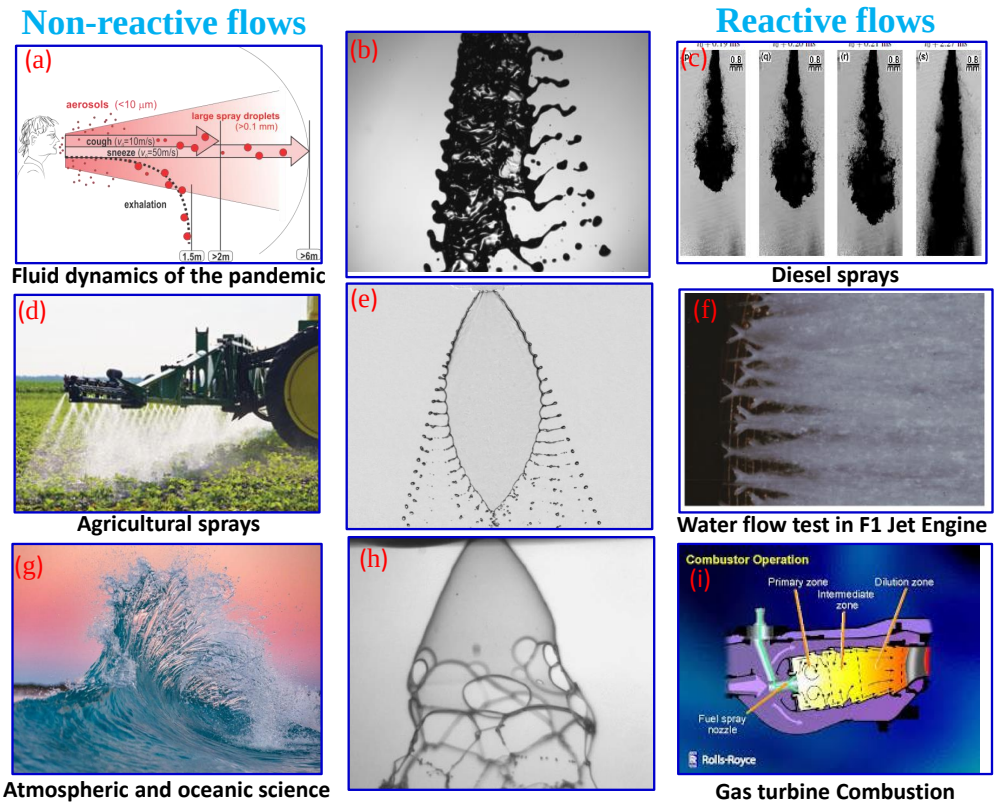

Figure 1: Application of sprays, jets, liquid sheets in different domains of day to day life, Images courtesy :(a) Cough droplet dispersion [1], (b) Liquid sheet [2]),(c) Diesel jet [3],(d) Agriculture sprays [4],(e) Flat liquid sheet [5],(f) Impinging jets in F1 jet engines [6],(g) Ocean waves [7], (h) Hollow cone liquid sheets[8], (f) Rolls-Royce engine[9]

fossil fuels (such as coal, oil and natural gas) has been firmly solidified, emissions of these gases have risen. To list a few examples, combustion in automotive (figure 1c), aeronautical (figure 1i) and rocket propulsion industries (figure 1f), burning forest lands, or mining and burning coal in industrial power plants is main source of GHG emissions.

We artificially move carbon from solid+liquid storage to its gaseous state thereby increasing atmospheric concentrations. The fossil fuels have unequaled physical properties which explains why they are largely used in all modern human activities, directly or indirectly. Attempts to use other energies sources (like batteries, hydrogen) in transport are still marginal and in any case, the question of the primary source used to produce electricity or hydrogen still remains. In their liquid state, fossile fuels have large energy density (the amount of energy per unit volume). The most common way to convert the chemical energy stored in the fossil fuels into mechanical energy for transport is combustion, i.e. a chemical reaction in gas phase between air and fuel vapors. For example, in the case of aircraft

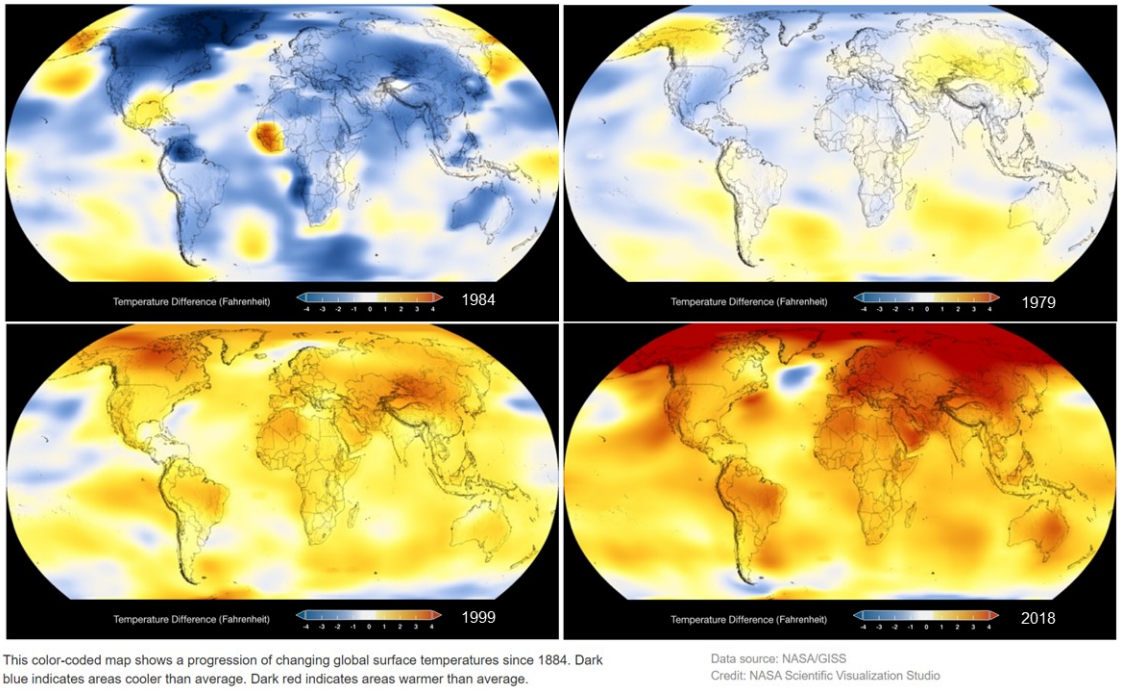

Figure 2: Color-coded map showing progression of changing surface temperatures from 1984 to 2018. Dark blue indicates areas cooler than average and dark red indicates areas warmer than average [10]

engines, the combustion consists following steps:

- **Injection.** The liquid fuel emanating from nozzle is injected into the combustion chamber.
- **Primary Atomization.** The process in which the liquid core or sheet is attached to the nozzle and the liquid is composed of many big and small droplets, ligaments, thin filaments, non-spherical droplets etc. This process is generally associated with the near orifice region.
- **Secondary atomization.** The process of the spray formation due to sequential break up of ligaments and second generation non-spherical droplets, which eventually form smaller daughter droplets.
- **Evaporation.** Phase change of liquid atomized droplets to gaseous state.
- **Mixing.** The fuel vapor is mixed with the surrounding air down to molecular level.
- **Ignition.** Depositing the required amount of energy for chemical reactions to be initiated.
- **Heat production** . All aforementioned processes are made to ultimately produce heat

which is associated with exothermic chemical reactions occurring within the flame front. The flames can be of either premixed or of diffusion type, or a combination of both.

In general, the first three stages are common in most of the reactive and non-reactive flows. All the processes can occur simultaneously, as in aeronautical engine, or sequentially like in a car engine. It is nevertheless often the fate of an individual liquid droplet which is of practical interest. For instance, the bigger droplets take more time to evaporate, mix and burn [36, 37]. Conversely, fine droplets can burn too soon after their formation, and may damage the injectors. In reality, the complete control of atomization has not yet been possible, but remains one of the ways to improve car engine fuel consumption [38].

(B) ***Agricultural spraying, spray-painting and ink-jet printing, dust control***: Spray drift is becoming an increasingly important concern in agriculture field as shown in figure 1d. It is the dispersion of drops through the air, during or after application, to a site other than the intended target. If these drops contain some pesticide concentration, it may cause damage on the surroundings and on the people's health. Standard flat fan atomizers used to spray fields with fertilizers and pesticides produce broad drop size distributions, with a notable fraction of diameter below 100 μm (called fine drops). Droplets less 100 microns are particularly prone to spray drift [39, 40]. On the other side of drop size distribution, the biggest droplets are too heavy to hook on plants leaves or rebound on them, splash like raindrops, and increase the probability of plant-to-plant contamination [41]. Strategies to reduce spray drift and avoid too large drops need the droplet size distribution to be controlled. This remains the subject of active research [42, 43].

For similar reasons, the rotary atomizers used in the surface coating industries produce many droplets that fail to reach the targeted surface [44].

Water spray is one of the chief methods employed to control airborne dust in industrial operations with a capturing efficiency depending critically on the droplet sizes [45].

In commercial inkjet printers, the droplets produced are very small 50 μm and traveling at high speeds $\sim$ 5 – 20 m/s. In this situation, satellite drop production is undesirable and causes notorious difficulties in inkjet printing [46, 47].

(C) ***Exhalations, disease transmission, inhaled medicine***: The pathogens responsible for COVID-19, severe acute respiratory syndrome coronavirus 2 (SARS-CoV-2) are transported by the respiratory droplets exhaled by an infected person [48–51] (see figure

1a). One key mechanism for the generation of respiratory droplets is the visco-elastic instabilities [52] and eventual breakup and fragmentation of the mucus lining due to the shear stress induced by the airflow. The key factors that have implications for transmission of pathogens through expiratory events are drop number density, velocity and size distributions and numerous studies have attempted to measure these characteristics ([53–55]. This well known fact is currently re-examined in the light of modern methods and ideas which shows that, small respiratory drops are transported farther than larger drops, because they are suspended by the gas flows associated with exhalation [56–58]. There is a yet unexplored question which is that of most dangerous long-lived droplets in the exhaled spectrum. It has been suggested that the finest are the nastiest, through a collective evaporation delay mechanism [59].

Some therapies rely on inhaled aerosols or droplets (e.g. for lung diseases) which carry drugs. Here again, particles size is critical. Too large droplets will not reach the finest lung alveoli while too small droplets will escape due to the lung's natural clearance mechanism. Controlling particles sizes, and density is thus vital in this context [60].

Atomization and sprays

The aforementioned examples suggest that sprays are ubiquitous in our everyday life. Whatever the process or application, its efficiency depends on the spray characteristics and its optimization requires the spray formation to be controlled. Most of the mechanical atomizers/nozzles used for spray production proceed in three main steps: the ejection of a liquid flow due to pressure energy, then conversion of this pressure energy into kinetic energy and finally into interfacial energy. During this process, deformations appear on the liquid interface, these deformations grow in space and time and eventually result in the formation of liquid fragments from the main liquid bulk, called as primary atomization. In the next step, secondary atomization is where liquid fragments formed during primary atomization further undergo breakup to form smaller droplets. This process being repeated until these drops become stable drops. Stable drops are obtained when the surface tension force is strong enough to ensure the cohesion of the liquid fragment [32, 34, 61].

From a general point of view, two major factors control the primary atomization mechanism, namely, the presence of initial disturbances in the flow and a mechanism allowing for perturbations to grow. Theoretical analyses have been carried out by many researchers on the initial distortion and disintegration of liquid streams. These approaches

are based on the determination of most unstable modes that grow on the liquid–gas interface and therefore dominate its breakup. For example, one of the earliest work on disintegration of flat liquid sheets which reveals the mechanism of initial distortion and disintegration is due to Squire (1953). He developed a linear stability theory for a liquid sheet of constant thickness evolving in a gaseous environment [62]. Hydrodynamic sheet instability is controlled by two main sources of disturbance: aerodynamic forces at the interface (Kelvin–Helmholtz instability) and the capillary instability (Rayleigh-Plateau) by virtue of surface tension forces acting on the edges of the liquid sheet. Hagerty and Shea [63] (1955) demonstrated that aerodynamic forces produce growing transverse waves across the width of the sheet causing only two modes of Kelvin–Helmholtz instabilities, namely, the sinuous mode (where both interfaces oscillate in phase) and the varicose mode (where interfaces are in opposite phase), resulting in the formation of unstable ligaments and droplets.

Dimensionless numbers: Any physical system can be most succinctly described in terms of dimensionless variables. Atomization depends on many physical parameters: density, viscosity, surface tension, characteristics length scale, velocity and gravitational field. These parameters can be expressed in terms of three fundamental units: mass (M), length (L) and time (T). One can then group these variables into dimensionless numbers, some of which are given bellow:

$$We = \frac{\rho_l U_l^2 a}{\sigma} \tag{0.0.1}$$

$$We_g = \frac{\rho_g (U_g - U_l)^2 a}{\sigma} \tag{0.0.2}$$

$$Re = \frac{\rho_l U_l a}{\mu_l} \tag{0.0.3}$$

$$Oh = \frac{\mu_l}{\sqrt{\rho_l a \sigma}} = \frac{\sqrt{We}}{Re} \tag{0.0.4}$$

where ρ_l and ρ_g are the liquid and gas densities, respectively, μ_l is the liquid dynamic viscosity, σ is the surface tension acting on the interface, a is a characteristic length scale and U_l is the fluid speed. In practice, the liquid Weber number We (0.0.1) is used for jet instability analysis and gaseous Weber number We_g (0.0.2) and air-assist/ annular flows respectively. The Weber number indicates the relative magnitudes of inertial and surface tension forces. The Reynolds number (Re) in equation (0.0.3) describes the relative magnitude of inertial and viscous forces. Finally, the Ohnesorge number (Oh equation 0.0.4) emphasizes the relative magnitude of viscous and surface tension forces. It can be

recast in terms of a combination of Re and We. These dimensionless numbers are used to identify different atomization regimes. In particular, the different breakup mechanisms are often categorized in a Weber-Reynolds numbers diagram.

Depending on the situations, further dimensionless numbers can be useful, such as momentum flux ratio (MR), the Froude number(Fr) and the Bond number (Bo) which are given below:

$$MR = \frac{\text{Liquid momentum flux}}{\text{Gas momentum flux}} = \frac{\rho_l U_l^2}{\rho_g U_g^2} \tag{0.0.5}$$

$$Fr = \frac{\text{Inertia}}{\text{Gravity}} = \frac{U_0^2}{ga} \tag{0.0.6}$$

$$Bo = \frac{\text{Gravity}}{\text{Surface tension}} = \frac{\rho_l g a^2}{\sigma} \tag{0.0.7}$$

For the configuration of interest in the present work, i.e. a flat fan liquid sheet, one distinguishes two main breakup regimes. 1) At low-Weber numbers, the liquid sheet is smooth and liquid beads are formed along the rim periphery and eventually detach from the sheet (An illustration of this regime is shown in figure 3a-b). In rim-driven disintegration capillary instability causes the pinching of beads from the rim to droplets. 2) For high liquid Weber numbers, a large amplitude sinuous Kelvin–Helmholtz (K-H) instability grows on the liquid sheet and causes its disintegration (see figure 3c-d). The wave-driven instabilities are created by the flapping of the sheet, induced by the ambient air. Squire (1953) [62] established a criterion for the (K-H) instability to develop. When the perturbation wavelength is greater than the thickness h of the sheet (kh >0.5, where, k is the wavenumber of the disturbance) the wave tends to grow. In terms of liquid Weber number (defined using h as characteristic length-scale), that means that the perturbation will grow when

$$We_h = \frac{\rho_l U_l^2 h}{\sigma} > 2 \tag{0.0.8}$$

This condition shows that a minimum difference of velocity between the two fluids is required for an instability to develop. When $We_h > 20$, Squire (1953) found that the characteristics of the optimum sinuous wave of wavelength are:

$$\lambda_{opt} = \frac{4\pi h}{We_h}; \quad \omega_{max} = \frac{\rho_g U_l^2}{\sqrt{2h\rho_l\sigma}}, \tag{0.0.9}$$

where ω_{max} is maximum growth rate which occur at a wavelength (λ_{opt}). A review of these

theoretical approaches of break-up regime in other flows can be found in Sirignano and Mehring (2000) [64]).

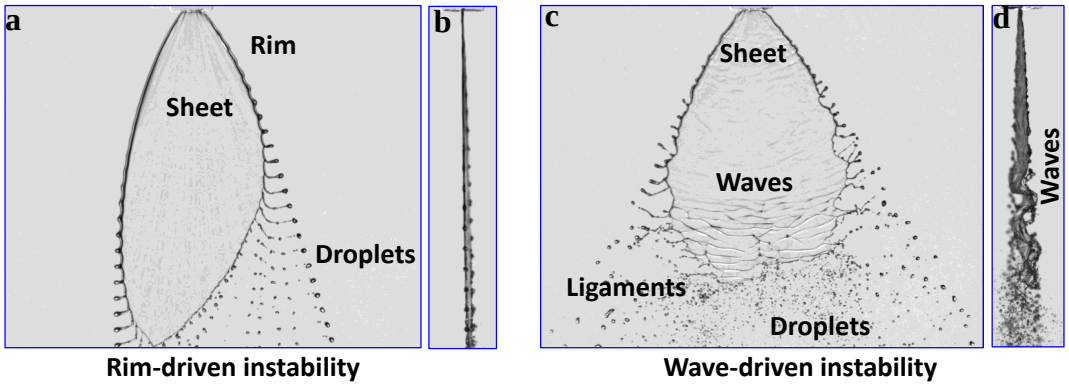

Figure 3: Disintegration regimes of flat liquid sheet. (a) Front view (b) side view of smooth regime (regime 1), (c) Front view (d) side view flapping regime showing Sinuous mode of disintegration of a fan-nozzle liquid sheet (regime 2)

From an experimental point of view, the primary atomization step has often been ignored, and atomization analyses have consisted in developing correlations between spray characteristics (such as cone angle, breakup length or mean drop diameter) and selected parameters (such as liquid properties, selected nozzle dimensions, injection pressure, etc.). This was due to the fact that experimental approaches have suffered from a lack of specific and powerful diagnostics. Things have been changing since the past few years with the emergence of advanced experimental optical techniques and now efforts should be concentrated the primary atomization step, which links the injection zone to the fully developed spray zone [34].

There are two main types of measurable spray characteristics: macroscopic and microscopic (see figure 4). The macroscopic level includes anything seen with the naked eye (cone angle, intact core length, etc) while the microscopic level is more related to some scale-dependent properties (such as the drop size distribution). Probing transparent or semi-transparent media to extract the measurable characteristics is a constant preoccupation in multiphase flows. There are wealth of optical techniques to measure what happens in the downstream dilute spray (secondary atomization) or liquid sheet far-field region using various conventional imaging techniques such as back-light illumination [14, 65–67], light scattering [68], structured laser illumination planer imaging (SLIPI) [69, 70]. The abovementioned techniques are efficient enough to extract interesting information about the spray characteristics, such as the sheet expansion angle [14, 66, 67, 71], the liquid

sheet intact length [67, 71–73], the wavelength of liquid sheet [11, 74], and droplet size distribution [75, 76]. All this information can be used to understand further downstream complex phenomenon.

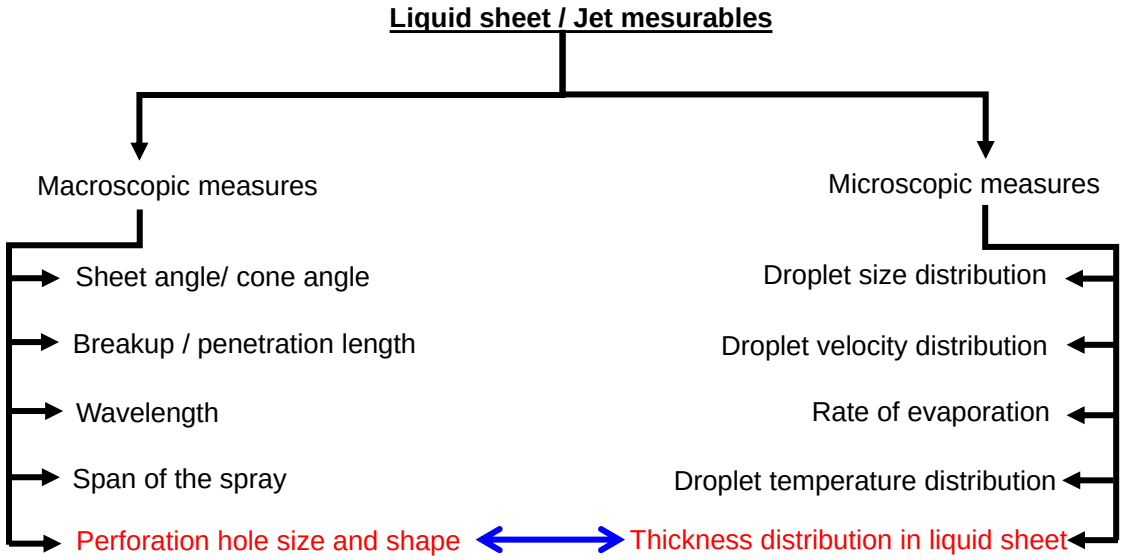

Figure 4: Macroscopic and microscopic measurable characteristics for liquid sheet or jet

Much work has been done on the optimization of drop sizes in sprays, but most research so far only deals with a few specific aspects of the droplet formation without considering primary atomization or liquid intact zones, and a more complete and generic understanding is lacking. There is a yet unexplored relationship between interconnected mechanism of primary and secondary atomization which determines the droplet size.

Objective of the current research

From the previous general overview, one readily grasps that a specific exploration of the primary atomization process is required. The study presented in this PhD report lies in this context and aims at providing a quantitative analysis of the process at play in the particular case of a liquid sheet flowing into quiescent air. As already mentioned and as we will see in forthcoming chapters, the liquid sheet thickness is pivotal quantity on which depend many other macroscopic and microscopic features of the flow. One of the main objective of this thesis is to develop a new optical technique for measuring the absolute values for local liquid sheet thickness. These measurements are believed to help in providing insights into the physics of liquid sheet. For instance, the measured thickness data will be used to deduce physical or empirical relations between various parameters governing the behavior

of liquid sheet atomization, for example, understanding the kinematics of single perforation hole and collision of perforation holes. In addition, because liquid sheets appear transparent to conventional back-light illumination techniques, we will aim at proposing a new method for enhancing the image contrast between the liquid and gas phase.

These optical tools are here applied to a canonical injection bench using different flat fan spray atomizers and various values for the fluid and flow parameters. This thesis aims at addressing the following questions:

Experimental test bench: Can we construct a canonical test bench which can allow the various stable and unstable regimes of liquid sheet to be observed? When the liquid sheet produced by a flat fan atomizer, does it retain some similarities with the one produced by two impinging jets? What are the flow parameters and test fluids required to obtain the stable and unstable regimes?

Optical technique: Can we develop a new technique for measuring the evolution of the liquid sheet thickness? What is its sensitivity? What are the differences are there with existing optical techniques?

Analytical comparisons: Does the measured evolution of the liquid sheet thickness comply with the established theoretical relations? Can we deduce the growth rate of perforation in liquid sheet? How does it compare to theory?

To answer these questions we have developed or used different techniques which are listed below:

- **Conventional backlight illumination:** to study the different topological structures of the liquid sheet with the goal of appraising the various stable and unstable regimes of such flow in the nozzle near-field region (Chapter 3).
- **Femtosecond time gated measurements:** the development and application of a non-invasive technique for measuring the local thickness of a flat liquid sheet (Chapter 4)
- **Femtosecond time-gated imaging:** This time-gated optical configuration with large field of view yields enhanced contrasted images of the liquid sheet when compared with conventional backlight images under same flow conditions (Chapter 3)
- **High-speed backlight illumination imaging:** to study the kinematics of perforation appearing on liquid sheet, high-speed back-light illumination experiments were

performed (Chapter 4).

The results obtained for each of these optical diagnostics are analyzed meticulously using appropriate post-processing tools and will be discussed in forthcoming chapters of the thesis.

Organization of the manuscript

This manuscript consists of five chapters including the current introduction. A brief summary of each chapter given below:

- **Chapter 2**:
  This literature review aims at discussing the physical picture of the different flow structures in flat liquid sheets when the flow rate is increasing. It starts with a brief review of different regimes of these flow structures based on classical non-dimensional numbers used in the atomization and spray literature. Particular emphasis will be given to the dependence of the flow structures to the local liquid sheet thickness. Next, it presents a brief review of the most common class of optical techniques that are utilized for liquid sheet thickness characterization, their shortcomings and need for development of new optical tools. Lastly, we briefly review the working principal of time-gated imaging which is at basis of the proposed liquid sheet thickness measurement technique.

- **Chapter 3**:
  The purpose of this chapter is to describe the different thickness measurement optical methods which are designed and developed during this thesis. At first, we begin this chapter by explaining the flow bench configuration with details about test facility and test conditions. Next, we consider a detailed discussion on various stable and unstable sheet visualization using complementary techniques such as classical backlight illumination. Then we introduced a high speed imaging for preliminary characterization of perforation hole appearing on liquid sheet. After exploring the prospects of classical imaging techniques, in context of liquid sheet, using various frame rate detectors (cameras), we move on to our novel thickness measurement techniques. A brief review of the working principle of non-linear optics, in particular, Second harmonic generation (SHG) is discussed. Followed by a discussion on how we can measure the time delay using SHG and thus thickness of the probed medium. Then, for testing measurement

protocol, we have designed a first optical setup referred to as single pass arrangement. Next, we propose another configuration for the optical time-gate with multi-pass setup, thereby solving most of the issues with the single pass configuration. Moreover, the possibility of using multi pass setup for liquid sheet thickness measurement is limited by reduction of intensity of the imaging beam compared to gating beam. Thus to overcome imaging beam attenuation, two pass inline setup is designed and discussed. The data extracted from each of these methods has been analyzed meticulously to compute probed medium thickness, by developing in house code with use of numerical tools. A particular effort is devoted to the y-averged intesity of time-gated images in terms computing the slope of spatio-temporal diagrams and computation of time delay between probed medium and air.Towards the end of this chapter, Towards the end of this chapter, it was demonstrated that with slight modifications in two pass in-line configuration how one can acquire enhance contrasted images of liquid sheet.

- **Chapter 4**:

  The liquid sheet thickness distribution measured for various stable and unstable regions and test cases of sheet is now compared with the semi-analytical sub-model of Dombrowski et.al. The observance of non-monotonic behavior in thickness distribution is explained using scaled front and side view images of the liquid sheet. We noticed that for few test cases perforation in liquid sheet is at play. For this reason, high speed imaging is performed with the goal of capturing holes at measured location condition. The algorithm for detection and tracking of the hole is explained. The hole geometric and kinematic features are then studied as a function of the the area, perimeter and location of the hole. In the latter part the comparison between experimental, semi-theoretical and purely theoretical growth rate of perforation is highlighted. The area evolution of the hole and its convection velocities are also discussed towards the end of this chapter.

- **Chapter 5**:

  This chapter is dedicated towards the central conclusions emerging out of the present study with future directions and perspectives.

1 | Literature Review

The present chapter presents a historical review of liquid sheets, their types and related physical phenomena. We specifically outline a parameter study of the flow and describe the rich variety of forms observed for the liquid intact region in fan like liquid sheets.

Section 1.2 gives an overview of liquid sheet flow structures reported in the literature through experimental or numerical visualizations. Section 1.3 reports the prior works done on fluid sheets, to include terms arising from the variation of the sheet thickness and perforation holes. Next, we present the existing intrusive and non-intrusive techniques for thickness measurements and their shortcomings in section 1.4. We conclude in section 1.5 by presenting the time-gated imaging technique and its working principal.

1.1 Liquid sheets

1.1.1 Flat Savart sheets by jet impingement on solid surface

Research on fluid sheets was first considered by the early exploratory experiments of Savart (1833) [77], who investigated the sheets formed when a vertical fluid jet strikes a small horizontal circular impactor as shown in figure 1.2i-ii (images adapted from Bremond, Clanet and Villermaux (2007) [11]). Sheet formation by jet impingement can be characterized on the basis of non-dimensional numbers, specifically the Froude and Weber numbers given by equations (0.0.6) and (0.0.8), respectively. For instance, a flat sheet will be generated by a vertical jet striking a horizontal impactor provided that the Froude number is large, i.e. $Fr >> 1$:

Surface tension force acts on the sheet surface. Consider an interfacial surface S bounded by a contour C as a shown in figure 1.1. For a 2D sheet, the magnitude of this

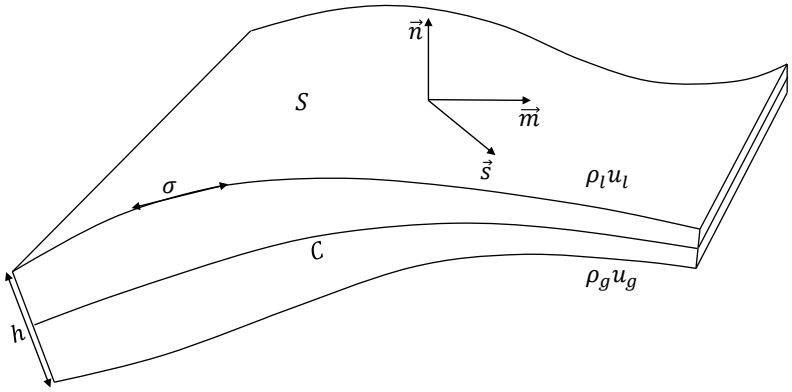

Figure 1.1: A surface S and bounding open contour C on an interface between two fluids. Local unit vectors are the normal vector $\vec{n}$ and the two tangential vectors $\vec{m}$ and $\vec{s}$.

surface tension force is given by:

$$\vec{F_c} = \int_C \sigma \, (\vec{\nabla} \cdot \vec{n}) \, \vec{n} \, \mathrm{d}l \tag{1.1.1}$$

Here l indicates arc-length and so dl a length increment along the curve C. Using the first Frenet-Serret equation [21]

$$(\vec{\nabla} \cdot \vec{n}) \, \vec{n} = \frac{d\vec{s}}{dl}, \tag{1.1.2}$$

where $\vec{s}$ is the unit tangent vector to the interface aligned with C, F_c can be written as

$$|\vec{F_c}| = \left| \int_C \sigma \frac{d\vec{s}}{dl} \, \mathrm{d}l \right| = \sigma(s_1 - s_2) = \sigma l \tag{1.1.3}$$

Thus by considering geometry of the end points 1 and 2, a net force on an interface per unit length, σ, along the length of the sheet rim acting to contain fluid in the rim.

Equation 1.1.3 may be applied to understand the dynamics of the Savart sheet and its topology. The mass and momentum of the incident jet are radially distributed, forming radially expanding sheet. This occurs up to a critical radius R_s, where a rim forms, and the liquid eventually disintegrates into small satellite drops. Savart observed two distinct regimes: below a critical liquid Weber number, $We_c \sim 1000$ (Jet diameter is used as characteristic length-scale for computing We_c), the sheet remains smooth up to the rim (figure 1.2ia) and as We_c is exceeded, the capillary waves starts appearing and liquid sheet begins to flap violently (figure 1.2ic).

Savart's observations were subsequently examined for expanding sheets. Taylor (1959), in the series of papers [78, 79], deduced the critical radius R_s in the smooth sheet

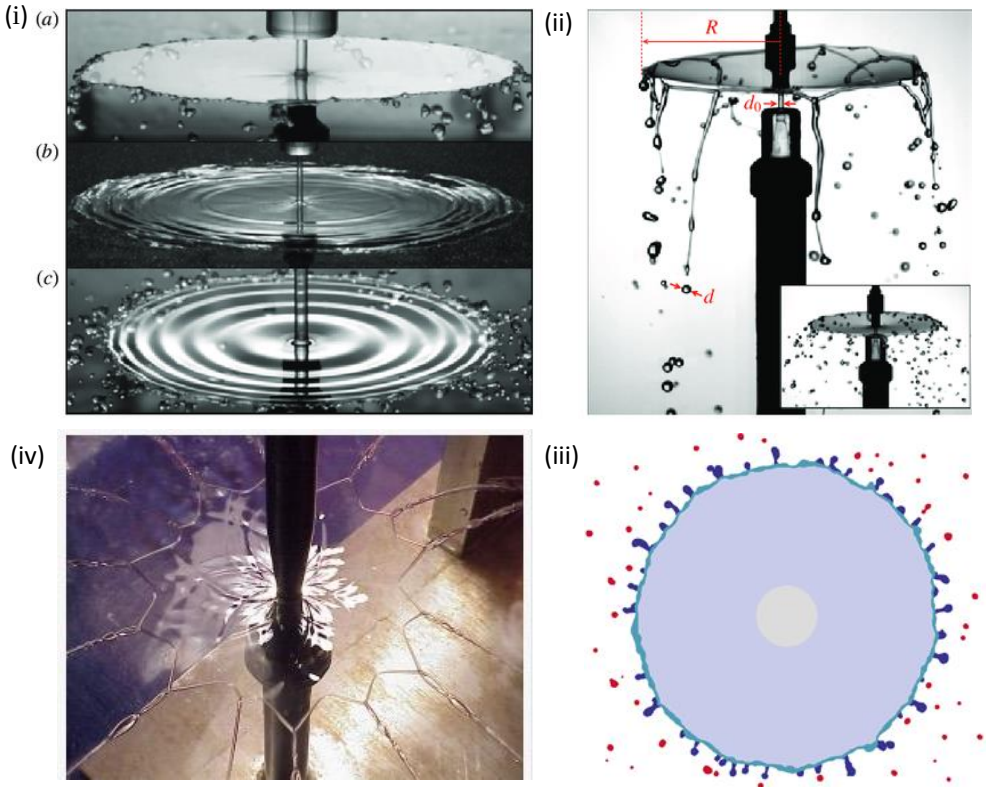

Figure 1.2: Different topologies of flat liquid sheets (i) Savart circular sheets, axisymmetric liquid sheet states: (a) smooth regime. (b) Flapping regime for larger Weber number (We_c higher than 1000). Capillary waves created by imposing vertical oscillations of the impact rod. [11] (ii) Close-up views of the free rim of a smooth liquid sheet, for cases (a) and (b) above, adapted from Bremond, Clanet and Villermaux (2007) [11], (iii) Liquid sheet produced upon drop impact on a surface of comparable size to that of the drop, a sheet is produced that evolves freely in the air, bounded by a rim from which ligaments and droplets are continuously shed[12], (iv) A polygonal fluid sheet (Buckingham and Bush 2001) [13] generated by extruding a glycerine–water solution of viscosity 10 cS from a circular annulus of diameter 1 cm. Fluid chains are seen to emerge from the corners of the polygon.

regime. R_s is prescribed by a balance of radial forces; specifically, the inertial force must balance the surface tension force by assuming a constant sheet speed U_b up to the rim, he obtained

$$\rho_l U_0^2 h \sim 2\sigma \tag{1.1.4}$$

Where h is film thickness and can be obtained by conservation of mass flux Q_m which is conserved at any radial position R in the sheet,

$$h = \frac{Q_m}{2\pi R U_0} \tag{1.1.5}$$

Consequently, the sheet thickness decreases as $1/R$. Substituting the form 1.1.5 for h into the force balance 1.1.4 yields the sheet radius, or so-called Taylor radius:

$$R_s = \frac{\rho_l Q U_0}{4\pi\sigma} \tag{1.1.6}$$

The critical sheet radius increases with source flux and sheet speed, but decreases with surface tension. The rim that develops at this radius becomes unstable to azimuthal perturbations and pinches-off due to capillary instability, often referred to as the Rayleigh-Plateau-Savart instability, as it was first observed on a sheet edge by Savart. Additional work done in the context of circular sheet atomization can be found in the articles by, Crapper et al. [80], Clanet et al. [81], Savva et.al [20], Villermaux et al.[82] and the references therein.

1.1.2 A sector or fan-like liquid sheets with different topologies

In the recent years, particular attention has been paid to liquid sheets both numerically and experimentally. They are believed to retain the essential breakup dynamics of other sheets such as hollow cone liquid sheets issuing from swirl atomizers. A simple method for forming liquid sheet is to use a fan nozzle, a device which enables the topological properties and dimensions of the sheet to be easily controlled by varying the approach passages to the nozzle orifice [24].

The orifice of this nozzle is formed by the intersection of a V groove with a hemispherical cavity communicating with a cylindrical liquid inlet [32] as shown in the figure 1.3ia-ib. Under this geometry, the flow through the orifice is confined in only one plane and the streamlines of the liquid converge to form a region of higher pressure behind the orifice exit. A flat sheet is produced as the liquid freely spreads through the orifice limited only by

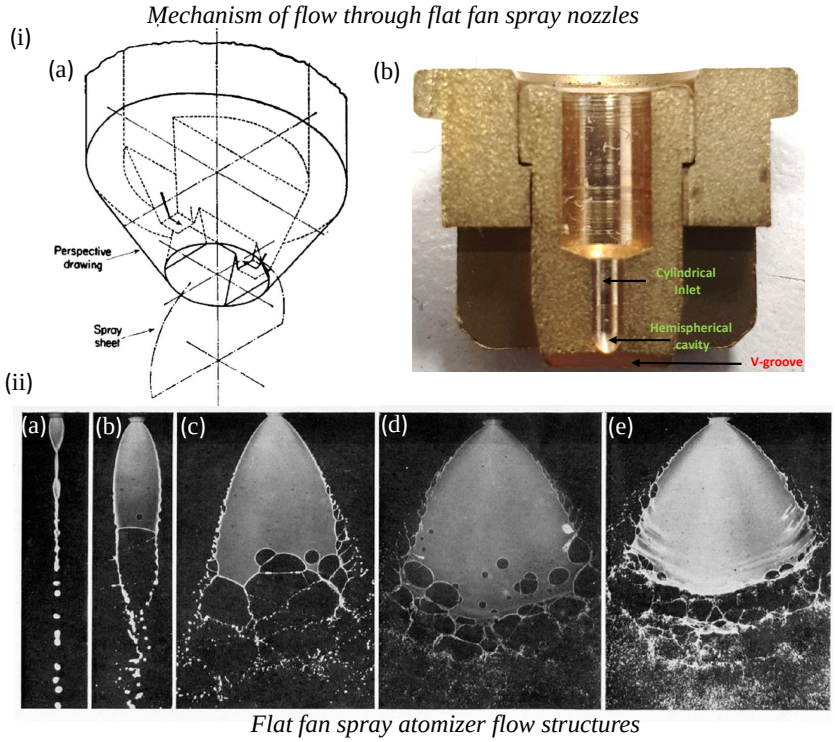

Figure 1.3: (ia) Mechanism of liquid flow through fan spray nozzles [14], (ib) cut-section of the flat spray nozzles for the present study (ii) A typical flash photograph of a low viscosity with a characteristic development of a liquid sheet with increase of pressure [15]

the side walls. The spreading angle of the sheet can further be increased by extending the opening to the sides of the orifice. Figure 1.3ib is the cut section of a commercial nozzle, designed on this principle, which has been used in the present work. It is made of brass and contains an elliptical orifice. The variation in design of these type of nozzle is responsible for marked differences in the topology of spray/ sheet distribution.

Dombrowski and co-workers investigated the behavior of flat liquid sheet produced by such fan nozzles in the series of papers [14, 15, 24, 80, 83, 84]. The sheets issuing from fan nozzle are bordered by two thick curved edges. Due to the surface tension, the edges of the sheet contract and a curved boundary is produced as the sheet develops further downstream. At low injection pressure, the edge contraction lasts until the edge of the sheet coalesce. During the contraction, drops can be emitted from the edge of the sheet, which is somewhat analogous to a cylindrical liquid jet. At higher injection velocities, the contraction is less pronounced, and the sheet eventually starts flapping and disintegrates before the two edges coalesce.

Dombrowski et al. (1954) [15] carried out photographic investigations of liquid

sheets. During their experiments, several liquids were tested ($\sigma \in [0.02; 0.073$ N/m], $\mu \in [10^{-3}; 50 \times 10^{-3}$ kg/ms]) and the injection pressure was varied from 0.06 to 0.34 MPa. By taking photographs of the sheet, they observed the effect of surface tension, viscosity, and density on the stability of the sheet and observe different topological structures, see figure (1.3ii). In addition, by using, the suspended particles in the sheet, they observed that the sheet streamlines are straight and unaffected by the curved boundary. Therefore, the drops produced at the edge are emitted in a direction that is different from that of the local sheet streamlines. By taking double exposure photographs, Dombrowski et al. (1960) [14] also reported that the streamwise velocity is constant along the sheet and depends only on the injection pressure. This conclusion of constant sheet velocity leads them to derive the expression for the sheet thickness as a function of the streamwise distance and compare with measured thickness by applying a method based on light interference (the detailed working principle of this method is described in section 1.4.2).

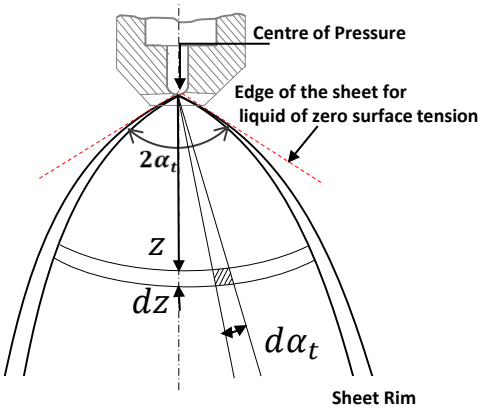

Figure 1.4: Flow pattern in liquid sheet showing elemental area of length dz

For the theoretical analysis of the liquid sheet thickness, they considered an element of the sheet, of length dz, subtending an angle dα_t at the orifice, and at a distance z from the center of pressure. With U_b, the liquid sheet velocity and h the thickness of the sheet, then the volume of the liquid flowing through the element $d\alpha_t$ in unit time is given by:

$$dQ = z.d\alpha_t.h.U_b \Rightarrow h = \frac{dQ}{d\alpha_t}\frac{1}{zU_b} \tag{1.1.7}$$

Since the liquid streamlines are straight and the stream velocity is constant throughout

the sheet, $dQ/d\alpha_t$ and U_b are constant, and thus

$$h = \frac{K}{z} \tag{1.1.8}$$

where K is called the sheet thickness parameter, which uniquely represents the variation of sheet thickness with downstream distance from center of pressure. Note that the position of the center of pressure might not coincide with the nozzle exit. We will see in the chapter 4 that the overall thickness distribution should account for a virtual origin (z_0) which represents the downstream position for this center of pressure. Dombrowski et al. (1960)[14] observed that for injection pressure $P_i > 0.15$ MPa, the thickness parameter K is independent of the surface tension and is inversely proportional to $(\rho_l \Delta P_i)^{1/2}/\mu_l$. In contrast, at low injection pressure, the parameter K decreases as surface tension increases.

Fraser et al. (1962) [24] examined the behavior of flat water sheets produced by a set of fan nozzles in which the thickness parameter K is varying from 10×10^{-4} to 31×10^{-4} cm^2. The injection pressure was varied from 0.17 to 5 MPa. The objective of varying the pressure was to identify its influence on the sheet stability and study the dynamics of perforation hole appearing on liquid sheet (the detail discussion is presented in the section 1.2). The surrounding ambient conditions were also varied in order to investigate the influence of the aerodynamic forces on the sheet behavior. The air density covered a range from sub-atmospheric to atmospheric condition leading to $\rho_g \in \{0.05 - 1.2\}$ kg/m^3.

Fan like liquid sheets can also be formed by the impingement of two cylindrical liquid jets. Such a configuration is used notably for fuel atomization in rocket propulsion engines. The geometry, shown in the figure 1.5a was originally considered by Taylor (1960) [78, 79] who conducted early experimental investigations on the behavior of such lenticular sheets. Fluid is ejected radially from the origin into a sheet with flux distribution given by $Q(\theta_s)$, (where θ_s is the angle between each fluid streamline sector from the origin of impact as shown in figure 1.5a) so that the mass flux flowing into the sector between θ_s and $\theta_s + d\theta_s$ is $Q(\theta_s)d\theta_s$. As in the previous case of the circular sheet explained in subsection 1.1.1, the sheet rims are unstable, and fluid drops are continuously ejected therefrom. The critical radius of the sheet can be computed similarly, but now depends explicitly on the flux distribution within the sheet $Q(\theta_s)$. The normal force balance now depends on the normal component on the sheet edge/rim and the normal sheet speed u_n is given by,

$$\rho u_n^2(\theta) h(\theta) \sim 2\sigma \tag{1.1.9}$$

The sheet thickness is again computed by equation 1.1.5, but now $Q = Q(\theta_s)$, so the sheet radius $R_s(\theta_s)$ is given by the Taylor radius

$$R_s = \frac{\rho Q(\theta_s) u_n^2}{4\pi\sigma U_0} \tag{1.1.10}$$

Where U_0 is bulk velocity of the jet. Computing sheet shapes thus relies on either experimental measurement or theoretical prediction of the flux distribution $Q(\theta_s)$ and thickness distributions $h(\theta_s)$ within the sheet which we will see in forthcoming section 1.3.

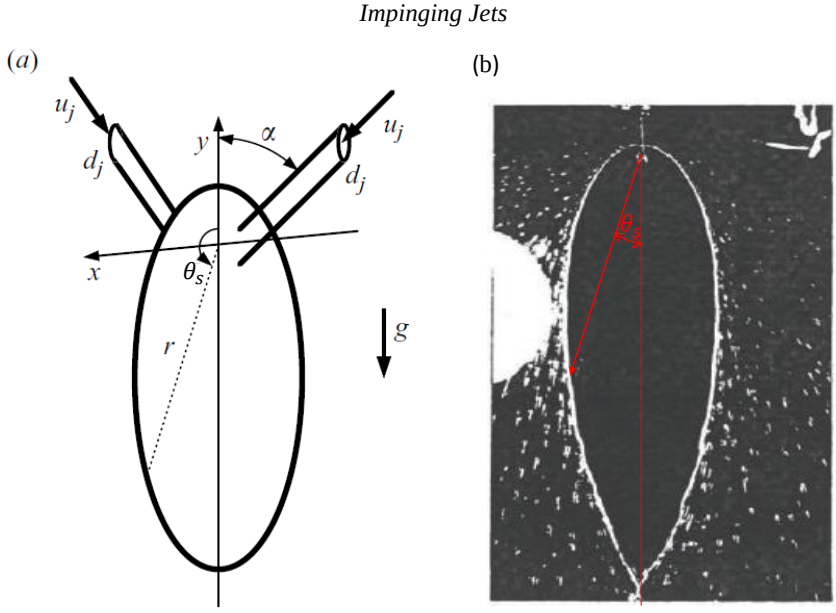

Figure 1.5: (a) schematic of two liquid jet impinging on each other [16]. (b) A sheet generated by the collision of water jets (G.I. Taylor (1960) [17].

1.1.3 Curved sheets

Liquid sheets are not always flat so that it is worth providing a brief overview of curved sheets. In this work, we have studied the process of sheet formation mostly with flat fan nozzle, but the process at play in curved sheet is mostly identical.

Curved sheets can take the form of hollow cones. They are most commonly produced by pressure swirl atomizer which consists of three main components: (1) inlet tangential ports (2) swirl chamber and (3) orifice. The process of hollow cone spray formation is as follows: (1) the tangential ports allow the flowing liquid to gain tangential momentum. (2) The liquid emanates from the orifice and exits in the form of a thin conical sheet as shown

in figure 1.6i. This sheet is subjected to growing perturbations leading to its disintegration into ligaments and fine droplets. (3) In such pressure swirl nozzles the rotational velocity is sufficiently high to cause the formation of an air core in the orifice and, also, in center of the swirl chamber before the orifice exit.

Basic pressure-swirl atomizer features (i.e., air core size, film thickness, cone angle, and discharge coefficient) are described in the pioneering analytical work of Taylor [85, 86] and in later work by Binnie and Harris [87], Dombrowski and co-workers [83, 88–90], Rizk and Lefebvre [91] and Yule and Chinn [92]. These works on pressure swirl atomizer revealed the basic mechanism involved in spray development when the injection pressure is increased. These include 1) dribble stage, 2) distorted pencil stage, 3) onion stage 4) tulip stage and 5) fully developed liquid sheet. The last three stages are susceptible to long wavelength breakup. Once the flow becomes fully developed, short wavelength break up becomes dominant [93]. At low injection pressures, the liquid first forms a closed bubble. With increasing pressure the bubble opens to form a hollow cone and the region of breakup moves away from the orifice. The pressure, at which the bubble opens to a hollow cone depends upon the design of the nozzle and the physical properties of the liquid, particularly on the viscosity and surface tension [15]. As the pressure is further increased, the region of disintegration of the sheet moves back towards the orifice. Bounding rim edge effects which are often marked in flat sheets do not, of course, arise in conical sheets. Additional work done in the context of primary and secondary atomization for hollow cone liquid sheets can be found out in the articles of Radcliffe et al. [94], Jasuja [95], Lefebvre [96], Santolya et al.[97], Hemmati et al.[98],[67].

All of the fluid sheets considered in the section 1.1.1 and 1.1.2 have been confined to 2D plane. In section 1.1.1, we considered circular sheets generated from a vertical jet striking a horizontal impactor. The sheet remains planar only if the flow is sufficiently fast for the fluid to reach its Taylor radius before sagging substantially under the influence of gravity. When either the angle of ejection is not 90° or when the flow rate is small, a jet impinging on an impactor gives rise to the so called fluid-bells 1.6ii. Decreasing the flow rate will make this sagging (1.6iii) more effective, and the sheet will no longer be planar. The bells close due to the azimuthal curvature and their shapes are essentially prescribed by the balance of inertial, gravitational and surface tension forces. Consequently, the sheet may close upon itself, giving rise to a fluid bell. A review on the dynamics of water bells has been carried out by Clanet [99] where he identified a regime where the bells become

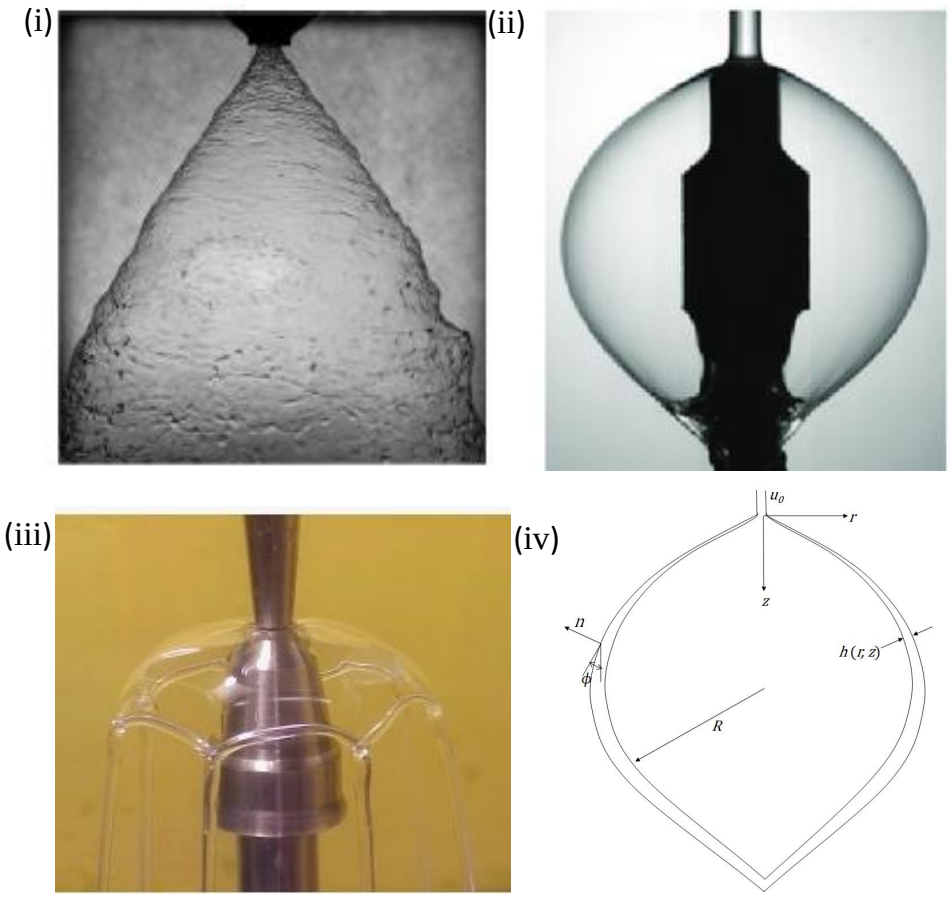

Figure 1.6: curved liquid sheets (i) Hollow cone liquid sheet produced by pressure-swirl atomizer[18] (ii) A stationary Savart fluid bell exhibiting the characteristic catenoid shape[19].(ii)sagging structures ressembling fluid umbrellas [20] (iv)schematic of water bell sheet element

unstable by progressively decreasing the flow rate of the impinging jet. We proceed by outlining a brief theory required to compute the shapes of water bells considered. This theory will make explicit the relation between the water bell shape and the liquid sheet thickness.

Consider a fluid sheet extruded radially by impacting of jet with velocity u_0 on a disc. The sheet is subsequently sagging under the influence of a gravitational field $\vec{g} = -g\vec{z}$. The inner and outer sheet surfaces are characterized by a constant surface tension σ. The sheet has constant density ρ_l and its thickness $h(r, z)$ is function of radial distance r and downstream direction z from center of impact. As shown in figure (1.6iv) the origin of the bell is the center of the impact plate. u is the local sheet speed, and ϕ the angle made between the sheet and the vertical. r_c is the local radius of curvature of a meridional line,

and s the arc length along a meridional line measured from the origin. Q is the total mass flux in the sheet and ΔP is the pressure difference between the outside and inside of the bell. Flux conservation writes:

$$Q = 2\pi rhu, \tag{1.1.11}$$

while energy conservation indicates that:

$$u^2 = u_0^2 + 2gz. \tag{1.1.12}$$

The sheet curvature reads

$$\vec{\nabla} \cdot \vec{n} = \frac{1}{r_c} + \frac{\cos\phi}{r} \tag{1.1.13}$$

The force balance takes the form:

$$\frac{2\sigma}{r_c} + \frac{2\sigma\cos\phi}{r} - \Delta P + \rho g h \sin\phi - \frac{\rho h u^2}{r_c} = 0 \tag{1.1.14}$$

The thickness of the sheet can be found out using equation 1.1.11 and equation 1.1.14 may be integrated to find the fluid bell shape. Additional work done in the context of atomization for fluid bells and swirling water bells are due to Taylor [100], Lance et al. [101], Parlange et al. [102], Clanet [99], Villermaux et al. [103], Bark [104] and reference therein.

1.2 Regimes of Liquid sheet flows

Figure 1.7 shows the different flow structure of sheets formed by flat fan spray atomizers [15], impinging liquid jets [21, 22]. It depicts the transition regimes of a liquid sheet with the progressive increase in flow velocity. Several flow patterns can be identified, namely (1) fluid chains [figure 1.7(ia, iia and iiia)], (2) fishbones structures [figure 1.7(ib, iib and iiib)], (3) stable sheet or open leaf structure without rim deformation [figure 1.7(ic, iic and iiic)], (4) flapping sheet with random holes appearance [figure 1.7 (id, iid and iiid)], (5) flapping unstable liquid sheet [figure 1.7(ie, iie and iiie)]. These regimes involving various topological structures were first discovered and studied by Heidmann et al.[105] and Dombrowski and Hooper [106]. Further implications remained uninvestigated until Bush and Hasha [21] focused on the flow structure which arises at various flow rates and reported the results of a combined experimental and theoretical investigation of the flow pattern.

Fluid chains: (Figure 1.7i,ii,iii a) At low flow rates ($We = 2000 - 4000$ and

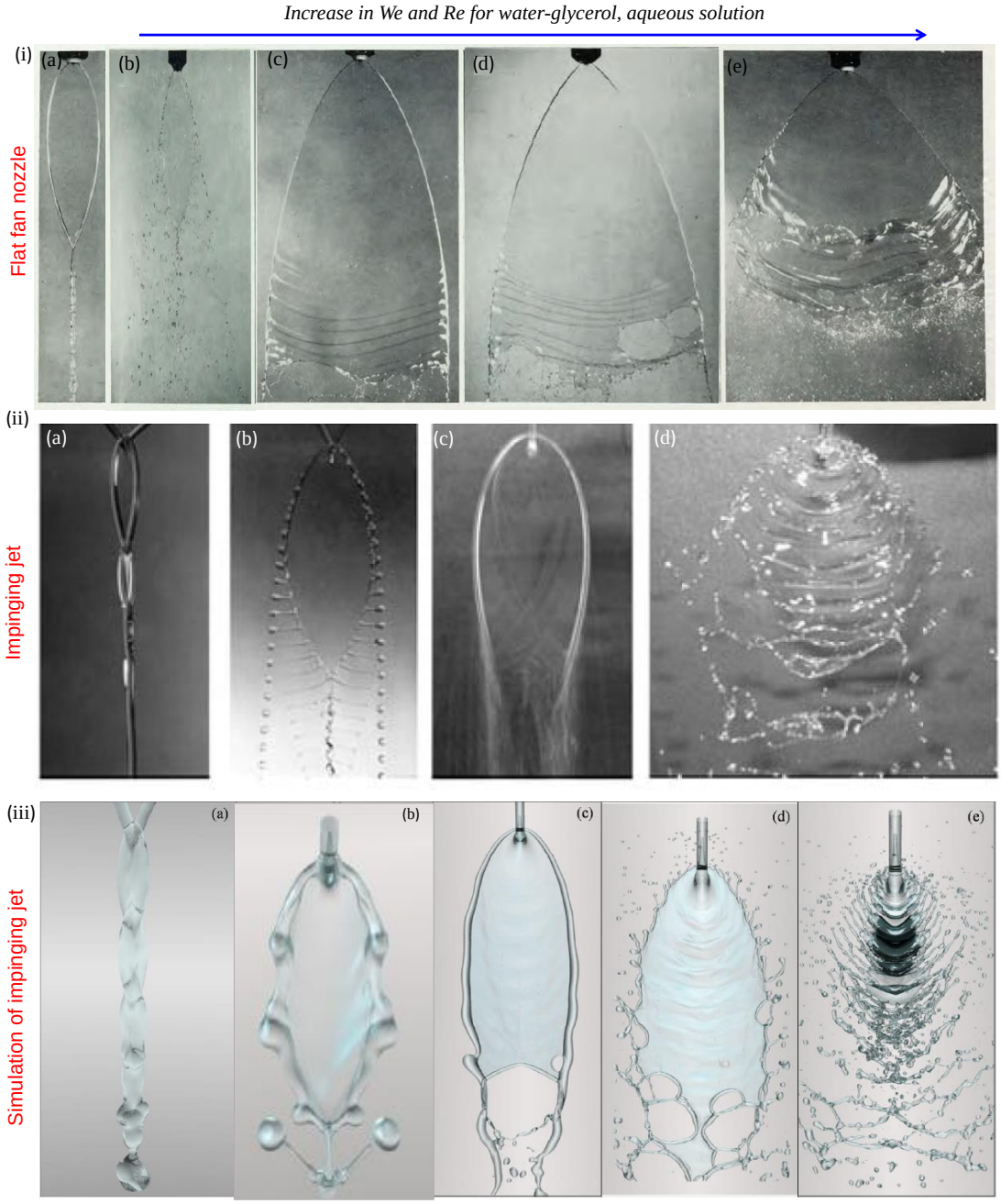

Figure 1.7: Single-flash images showing the evolution of the fluid patterns formed by (i) flat fan spray atomizer [15] (ii) impinging jet [21] (iii) simulation of impinging jets flow patterns using volume-of-fluid method [22]

$Re = 100 - 500$), impinging jets result in orthogonally linked sheets that finally forms liquid jet, which is referred to as fluid chain. The fluid chain pattern is a steady flow structure composed of thin fluid sheets bounded by relatively thick cylindrical rims. Fluid chains may occur in a variety of physical situations, for example, when water is poured from a lipped jug or when small stream of water flow off a leaf or sharp edge. For certain flow parameters, fluid chains were found to emerge from the corners of the polygonal sheet, as is shown in previous section 1.1.1, figure 1.2iv. Fluid chains have been first qualitatively observed by Rayleigh 1879 [61] and Dombrowski and Fraser 1954 [15] but no quantitative analysis of their form was done. In planar sheets, fluid is shot radially away from the point of injection at roughly uniform speed. Bush and Hasha [21] developed a theoretical model using a generalized version of Hasson predictions to predict the shape of the leaf/ first chain. The detailed theoretical model will be presented in later section 1.3.

Fishbones : Increasing the flow rate ($We = 2000 - 4500$ and $Re = 400 - 1200$) broadens the fluid chains as a long "spine" from which a regular succession of longitudinal ligaments and droplets emerge. This regime is referred to as "fluid fishbones" by Bush and Hasha [21] as the topological appearance resembles that of a fish skeleton with the fluid sheet representing its anatomical skull. Most importantly, they identified that the instability of the rim from the fluid tendrils can be rationalized by the Rayleigh-Plateau instability associated with centripetal force. They also noted that the fluid fishbones were not observed for all fluids, but arose exclusively for fluids with viscosities $5 < \nu < 39.5$ centi-stokes. Bremond and Villermaux (2006) [16] studied the shape of the sheet and size of fragmented droplets from fishbones of an ethanol sheet and demonstrated the formation of fishbone structures in this configuration. In their work, to produce a sheet with periodic atomisation, they implemented an unsymmetrical collison of two identical jets. Jung et al. [107] observed various fishbone patterns and examined the effect of difference in colliding jet length, jet alignment, and fluid viscosity on the development of the fishbone structure. Most of this aforementioned work on impinging jets so far has been carried out with Newtonian fluids (Dombrowski 1964 [106]; Bush and Hasha 2004 [21]; Bremond and Villermaux 2006 [16]; Bremond et al. 2007 [11]; Li and Ashgriz 2006 [108]; Villermaux 2007 [109]). Few studies have used non-Newtonian fluids. In this case, the fragmentation process is affected by elasticity and other non-Newtonian fluid properties (Cooper-White et al. 2002 [110]; Bazilevskii et al. 2005 [111]). Miller et al. (2005) [112] reported experimental observations of flow kinematics and stability of thin fluid sheets produced by the collision of obliquely aligned laminar jets of a series of viscoelastic worm-like micelle

solutions in which they found a new web-like flow structure. However, they did not show the entire evolution of the flow structure as the velocity was increased and paid no attention to periodic atomization. Jung et.al [113] used non-Newtonian polystyrene solutions in diethyl phthalate and polyethylene oxide solutions in glycerol-water mixture (60/40 % by weight). Both polymers were used with various molecular weights to investigate the effects of viscoelasticity on the fishbones patterns. The structures observed for these elastic fluids differ somewhat from those they previously reported [107] for Newtonian viscous fluids. They showed how the degree of viscoelasticity (concentration of the polymers) affects the evolution of fishbone pattern, its fragmentation, shape of ligaments and final drop sizes.

Stable sheet: Further weakly increasing the flowrate ($We = 3000 - 7000$ and $Re = 400 - 1400$) leads the fishbones sheet to revert into a stable and smooth sheet or chain with slight deformation of the rim. Int this regime, the flow is bistable: slight tuning in the flow rate may cause the structure to change from stable sheet to fishbones, or vice versa. At these flow rates, the bell leaf shape of the liquid sheet is partially developed with open rim and some capillary waves starts appearing far downstream of the nozzle exit. This flow pattern with partially open rims occurs for the upper limit of the flow rate for the stable liquid sheet regime. This regime is of particular importance in our work and the detail discussion of the application of this regime will be discussed in the next chapter. With similar range of flow velocity, the liquid sheet can also be unstable far downstream. This pattern can be referred to as the onset of disintegrating sheet or the open rim. Small random holes can be formed on the disturbed thin liquid sheet downstream. The hole can eventually reach the rim when it expands, thereby forming two horizontal liquid ligaments. The lower ligament can then breakup under capillary effect.

Flapping liquid sheet: As the jet velocity is further increased, the sheet becomes ruffled, forming a disintegrating sheet with unstable rim. Finally, at the highest flow rates, violent flapping ensues. Experimental work focusing on the high $Re - We$ regime, where sheets disintegrate by flapping can be found for example in Dombrowski and Fraser [15] and Dombrowski and Hooper [106]. Villermaux and co-workers [74, 114] explored further the destablization of sheets causing the catastrophic atomization and how the conditions near the source can affect the dynamics and the droplet size distributions.

Perforation holes: One of the important characteristic features of the sheets produced by fan nozzle or by impingement is that perforation holes appear on the sheet and extend

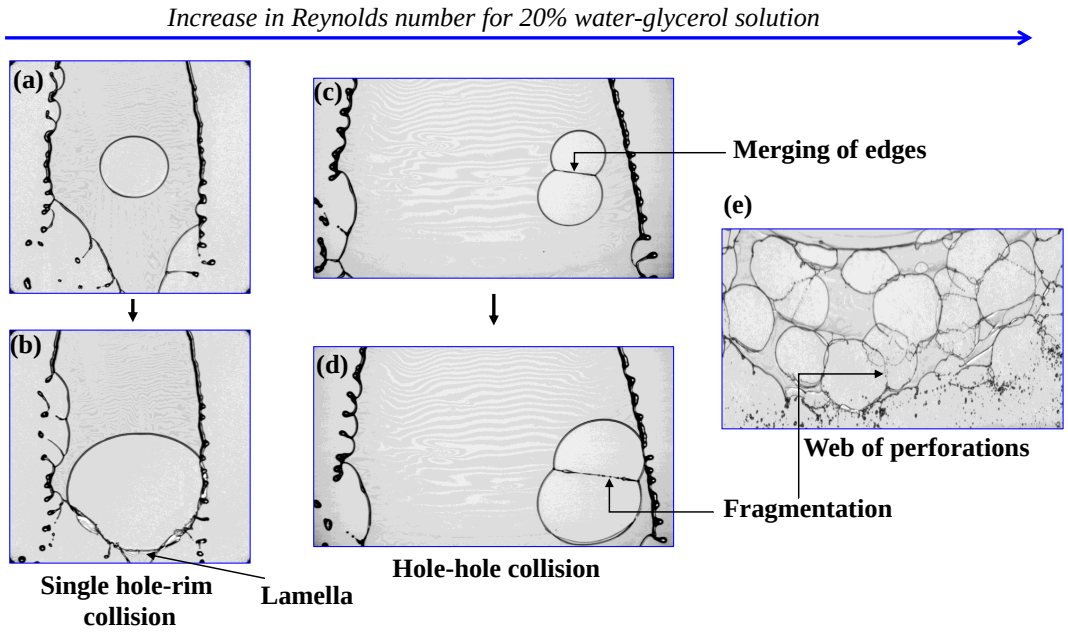

Figure 1.8: Representative instantaneous images of the flat spray liquid sheet showing different types of perforation collision mechanisms as a single hole rim collision, Hole-hole collision and interconnected web of holes.

up to the disintegration of the whole sheet to form ligaments and droplets [34] as shown in Figure 1.8.

The formation mechanism of these holes in the flat liquid sheets has been extensively investigated by various researchers. However, the fundamental question of the hole nucleation process itself has been less explored. As per Villermaux [19], there are many ways a film may puncture. Let us summarize four of them:

i) Temperature inhomogeneities (Marangoni 1878 [115]) at surface of a sheet can translate into gradient of surface tension by which a film may also rupture. For instance, Laser Induced thermocapillary flows are good examples of temperature inhomogeneities in liquid sheets. This Laser Induced Surface Tension Driven flows (LISTD) is utilized in microfluidic devices as an actuation mechanism. When a laser pulse heats the free surface of an optically absorbing liquid, non-uniform heating induces local surface tension gradients which in turn imparts tangential shear stresses causing the fluid motion and transport of heat. Several studies have highlighted the influence of laser beam (at various powers) on variable thickness liquid sheets [116, 117].

ii) Extremely small, thin objects are sensitive to thermal fluctuations. The minimal energy required to produce the rupture in the liquid film is of the order of σh^2, where σ

is surface tension and h is the liquid film thickness (the initial hole radius must be of the order of the film thickness h, or more). This surface energy can be supplied by the quantum thermal fluctuations due to the friction of the liquid through the small orifice. Thus, a scenario for the film to rupture leads to energy balance $h \sim \sqrt{k_B T_l/\sigma} \sim 0.1$nm. Where, T_l is liquid temperature and k_B is Boltzmann constant. After the rupture the expanding holes forms internal rim and these rims coalesce with each other to form intricate spider web kind of structure [8, 112].

iii) Internal impurities/dirt, chemical inhomogeneities in test fluid and defects in atomizer can also cause hole nucleation. For instance, solid hydrophobic anti-foaming agents can be taken to advantage for this effect [118] to be optimized and controlled. Immiscible oil droplets [15] or emulsion based liquid sheets can be responsible for the film piercing [43]. Neel et al. [25] have uncovered a mechanism of spontaneous puncture of thick liquid film by introducing ethanol droplet on moving liquid sheet which tends to alter the surface tension of the liquid.

iv) Effervescent or aerated atomization is a method of twin-fluid atomization that involves bubbling a small amount of gas into the liquid before it is ejected from the atomizer. As the liquid emanated from atomizer, the pressure suddenly drops, the gas bubble expands and liquid get perforated and fragmented into small volumes [15].

A sheet can also be punctured by an external source such as a needle which retracts liquid sheet due to unbalanced surface tension forces as shown in figure 1.9. This is in some sense the opposite configuration to the expanding sheet, but both share similar characteristics. Bursting phenomena arise in a wide range of physical settings, ranging from foams in the food industry to biological membranes (for an overview see [119]). Depending on the application vantage point, film rupture can be either desirable, as in spray formation [120], or undesirable, as in curtain coating [121]. The first observations of soap film rupture were delineated by Rayleigh [122] and Dupré [123] in the late 1800's. Their systematic study motivated the experimental work of Ranz in 1950 [124]. In his experiments he observed that following puncture, unbalanced surface tension forces at the hole edge set the hole into motion at a constant receding speed. In this process, fluid accumulates in a roughly circular rim as it is drawn away from the point of puncture. Dupré [123] did trivial mistake while deducing the retraction speed u_p of the film, based on false assumption that the surface energy associated with the consumed surface of liquid film due

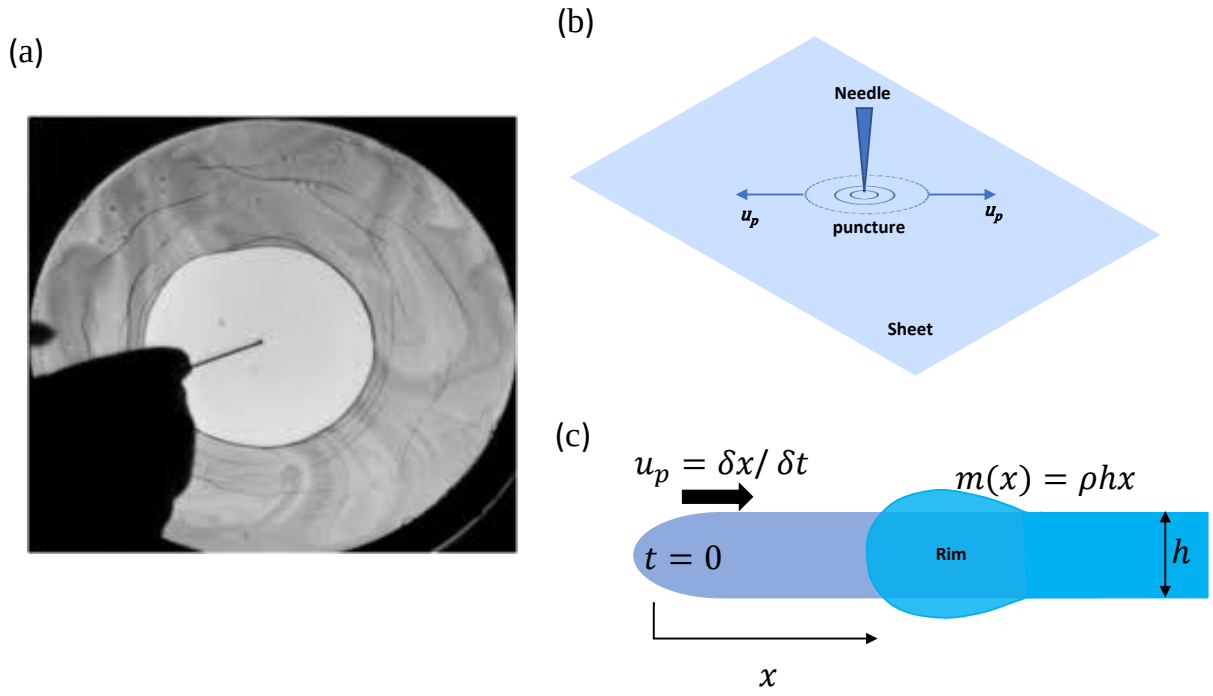

Figure 1.9: (a)Image of rupture in elastic soap film [23], (b)Schematic of rupture of the soap film with aid of needle (c) Surface tension induced retraction of planner film of uniform thickness released at time $t = 0$. The mass of the fluid (per unit length) accumulated in the rim during the time of rupture is $\delta m = \rho hx$

to retraction is converted purely into kinetic energy:

$$2\sigma\pi r^2 \approx \frac{1}{2}\pi r^2 \rho u_p^2 \Rightarrow u_p = \sqrt{\frac{4\sigma}{\rho h}} \tag{1.2.15}$$

Where, r is the radius of the rim and h is the thickness of the film.

In the late 50's, Taylor [79] and Culick [125] proved that even though Dupré's model contains good ingredients, it overestimates the retraction speed by factor $\sqrt{2}$. Taylor and Culick used another method for the conservation of momentum of the film and evaluated the retraction speed of the film. In particular, they considered a rupture in soap film and demonstrated that a hole radius, when large enough, grows in size at a constant retraction speed. The retraction speed can be obtained by simple force balance between, the curvature force associated with surface tension which pulls the rim radially outward and the rate of change of opposing momentum of the liquid mass (m) accumulated at the rim :

$$F_I = \frac{d}{dt}(mu_p) = u_p \frac{d}{dx} mu_p = u_p^2 \frac{dm}{dx} + mu_p \frac{du_p}{dx} = \frac{1}{2}u_p^2 \frac{dm}{dx} + \frac{1}{2}\frac{d}{dx}(mu_p^2) \tag{1.2.16}$$

The force balance between the curvature and the inertial force F_I reads

$$2\sigma = \frac{d}{dx}(\frac{1}{2}mu_p^2) + \frac{1}{2}\rho h u_p^2 \tag{1.2.17}$$

Integrating from 0 to x:

$$2\sigma x = \frac{1}{2}\rho h x u_p^2 + \frac{1}{2}\rho h \int_0^x u_p^2 dx \tag{1.2.18}$$

The term on LHS of equation 1.2.18 is surface energy per unit length, the first term on RHS is the kinetic energy of the rim and the rightmost term, the energy required to accelerate the rim. The important assumption in this model is that u_p is independent of x, thus $\int_0^x u_p^2 dx = x u_p^2$ and the force balance becomes

$$2\sigma x = \rho h x u_p^2 \tag{1.2.19}$$

Hence,

$$u_p = \sqrt{\frac{2\sigma}{\rho h}} \tag{1.2.20}$$

Equation 1.2.20 is known as Taylor-Culick speed [79, 125]. We note that the difference between the energy approach of Dupré' and the momentum approach of Taylor-Culick is a factor $\sqrt{2}$. In the Dupré's energy balance approach, there is no variation of the mass in the rim, whereas, Taylor-Culick considered the variation of mass in the momentum balance when the rim is moving. This is the origin of difference. Equation 1.2.20 is an important result, which will be useful for us when analyzing our experimental results (chapter 4).

Dombrowski and co-workers [24] extended the work of Taylor-Culick by considering flat liquid sheet produced by flat fan spray atomizer of uniform thickness and showed that growth rate of perforation strongly depends on local liquid sheet thickness and obtained an expression for the location of the origin of observed hole. Only after many years, Bremond and Villermaux [126] carried out an experimental study to understand the bursting of soap film by utilizing shock waves. They observed that modulations in liquid thickness amplifies and eventually the film is perforated, forming web of holes. They also demonstrated that the hole number density and the hole formation time depend on the film velocity and the thickness distribution along the soap film. Furthermore, a decade later, Altier et al. [127, 128] developed a simple model for collision and coalescence of two holes approaching each other in an emulsified liquid emanating from flat fan atomizer. More

recently, Asgarian et al. [129] carried out a comparative experimental and numerical study on turbulent flat liquid sheet and observed a bag breakup resulting from corrugation and perforation that appeared on the liquid sheet. The modified equation for growth rate of perforation has been introduced based on combined effect of Taylor-Culick speed and sheet expansion. Based on analytical and experimental study in understanding droplet formation due to collision of two holes, Villermaux and co-workers [130] showed that the holes rim collision is strong enough to trigger a new, splash-like mechanism, producing finer drops which ultimately changes mean drop size distribution.

1.3 Phenomenon related to the liquid sheet thickness

From the previous discussion, one understands that the liquid sheet thickness is a quantity of primordial importance. The above presented analytical studies yield the mathematical expression for the thickness evolution [14, 16, 131, 132], shape [14, 16, 131, 132] and velocity [16] of the liquid sheet, as well as the size of the fragmented droplets from the rim of the liquid sheet [21].

This section aims at emphasizing further the importance of the liquid sheet thickness in understanding the complex physics of liquid sheets flows. These include the dynamics of perforation holes, the formation of ligament from holes coalescence, and other phenomena.

Growth rate of perforation for single hole: The growth rate of perforation holes has a strong dependence on the local liquid sheet thickness and the thermophysical properties of the test fluid [19]. Dombrowski et al. [24] provided a theoretical explanation and an experimental proof for the growth rate of perforation (u_p) by considering a small puncture in an expanded flat fan liquid sheet (figure 1.10). Assuming uniform thickness h of the sheet, they hypothesized that if the hole diameter is greater than the thickness of the sheet, the perforation will continue to grow in size. Figure 1.10b show reasonable agreement with the curves calculated in accordance with the Taylor-Culick growth speed given by equation (1.2.20). They claimed that the experimental scatter arises from the irregularity in the contour of a perforation and its lack of sharpness in the photographs. In our study, we will see in chapter 5, how the measured thickness follows well established theoretical relations to characterize growth rate of perforation in liquid sheet.

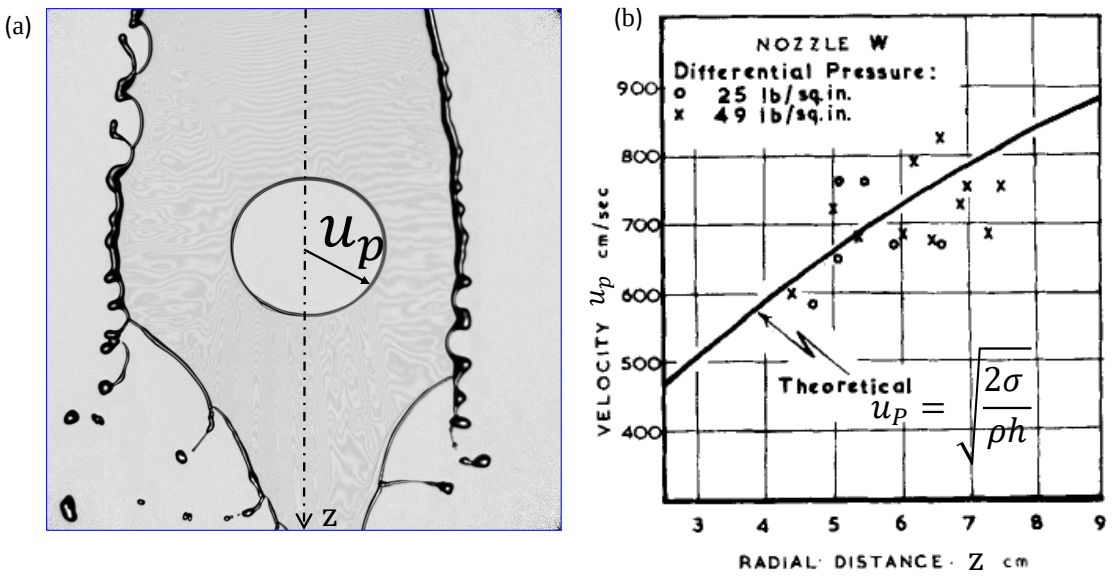

Figure 1.10: Representative instantaneous images of the flat spray liquid sheet for single hole with expansion velocity u_p in downstream direction z (b)Comparison of measured and calculated rates of growth of perforations [24].

Average diameter of ligaments for coalescence of holes: When two or more holes of distinct sizes originated from different locations on the sheet interact, the junction of the rims bordering them turns into a web of ligaments which concentrates all the liquid constitutive of the rim and breaks up into fine droplets (figure 1.11b). Occasionally, the rims collision is strong enough to trigger a new, splash-like mechanism, producing an expanding lamellae perpendicular to the main sheet, which destabilizes into finer drops. These finer droplets are produced from an auxiliary mechanism of coalescence besides the formation of the standard drops in atomization process. Recently, Villermaux et al. [19] showed that the average diameter $\langle D \rangle$ of the ligaments and droplets formed from a coalescence mechanism can be obtained by knowing the liquid sheet thickness h and rate of variation of hole center distances.

Lenticular sheets with stable rims shape prediction: Furthermore, when the liquid sheet thickness evolution is known, one can deduce the sheet shape theoretically and can compare with experimental stable and unstable liquid sheet rims (in liquid chains or fishbone structures). Bush and Hasha [21] developed a theoretical model by considering a stable rim to deduce the shape of the sheet.

It consists in a set of normal and tangential force balance equations (see figure

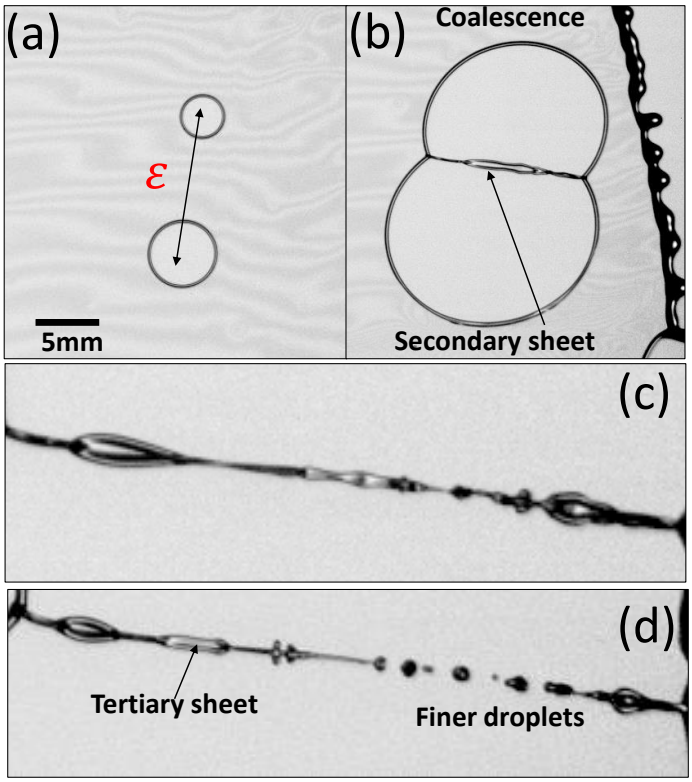

Figure 1.11: An example of the phenomenon of coalescence of two holes: rims of two holes expanding in a water film collide and eventually fragment into drop (b) the formation of a secondary sheet (c) tertiary sheet, which may itself breakup into finer droplets as in (d). Frames are separated by 0.6 ms.

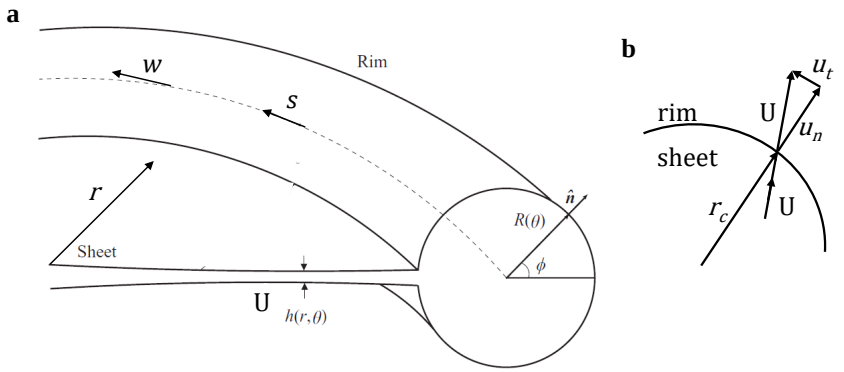

Figure 1.12: (a) A schematic illustration defining a cross-section of the rim and sheet used in Bush et.al [21] theoretical description of the fluid chain. (a) Free body diagram of the forces acting on the rim

1.12a-b) and a continuity equation which is written below

$$\frac{\partial}{\partial s}(\pi R^2 w) - u_n h = 0 \tag{1.3.21}$$

The continuity equation (1.3.21) leads a balance between the tangential gradient of volume flux swept along the rim of radius R due to tangential velocity (w) and the flux entering the rim from the sheet due to normal component of velocity (u_n). In case of unstable rims, such as those arising in fishbone instability, an additional sink term would appear in the continuity equation to consider the mass of tendrils (sub-jets coming out from rim) ([74]).

The balance equation between normal (equation 1.3.22) and tangential force (equation 1.3.23) is used to estimate the shape of the sheet. This balance equation requires the value of liquid sheet thickness. The normal force balance in equation 1.3.22 consists of the curvature force associated with the rim's surface tension balance, the force resulting from the normal flow into the rim from the fluid sheet and the centripetal force resulting with flow along the curved rim. The normal force balance is given by

$$\underbrace{\rho {u_n}^2 h}_{\text{Inertia}} + \underbrace{\frac{\rho \pi R^2 w^2}{r_c}}_{\text{Centripetal}} = \underbrace{2\sigma + \frac{2\sigma(\pi - 1)R}{r_c}}_{\text{Curvature}} \tag{1.3.22}$$

Note that the surface tension force has two component. The second term in equation 1.3.22, $2\sigma(\pi - 1)R/r_c$ can be neglected as the radius of curvature of the sheet is much greater than radius of the rim $R/r_c \ll 1$.

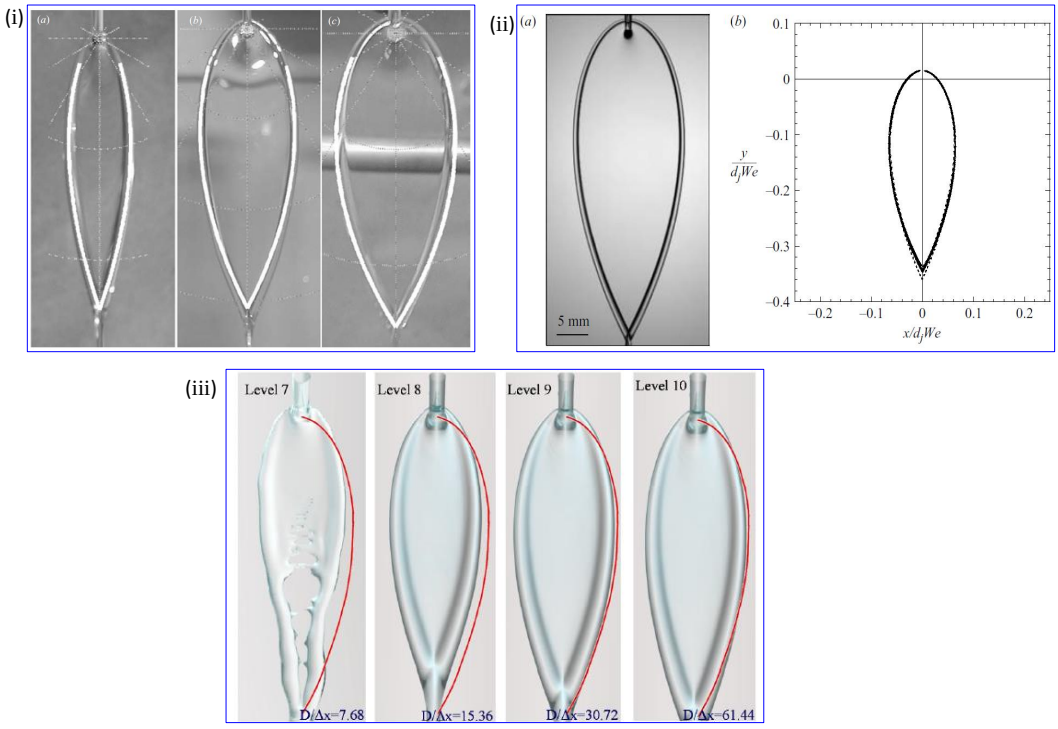

Figure 1.13: Comparisons of observed and theoretically predicted shapes of the sheets comprising the stable bell leaf shape for low *Re* and *We*. (i) Water-glycerol sheet (theoretical white line) [15] (ii) Ethanol sheet, experimental sheet contours normalized by the jet diameter and multiplied by the jet Weber number [16]. (iii) Numerical estimation for low velocity impinging jets, where a volume rendering has been used [22]

The equation for the tangential force is:

$$\rho \frac{\partial}{\partial s}(\pi R^2 w^2) = \rho h u_n u_t \tag{1.3.23}$$

Equation 1.3.23 indicates that the tangential force balance at the rim of the sheet consists in a contribution due to the tangential gradient of tangential momentum and the tangential momentum coming from the sheet.

The unknown variable in equations 1.3.22 and 1.3.23 is the tangential velocity (w) of the liquid in the rim and the liquid sheet thickness (h). The tangential velocity can be calculated using continuity equation 1.3.21 and the liquid sheet thickness can be obtained experimentally. Thus, by solving this system of equations and with the knowledge of liquid sheet thickness, one can deduce the sheet shape. Figure 1.13 presents a comparison of such an estimation with experimental or numerical results. It is observed that this theoretical analysis provides an accurate prediction for the liquid sheet shape.

1.4 Quantitative measurements of liquid sheet parameters

The above-mentioned literature review of section 1.2 reveals that, to predict phenomena such as surface waves, hydrodynamic instabilities, holes and ligament formation, it is crucial to have knowledge of the local liquid sheet thickness. From the numerical point of view, simulating liquid sheets is almost beyond the reach of available Direct Numerical Simulation codes because the ratio of the liquid sheet width and thickness is of the order of $10^2 - 10^4$ [129]. Also, there have been several theoretical efforts for predicting the sheet thickness but experimental results that can be used to compare with are very scarce. The measurement of the liquid sheet thickness is challenging because liquid sheets are almost transparent making it difficult to discriminate the liquid and gas phase with classical optical techniques. Another issue is given by the rims that are larger than the sheet thickness and prevent its measurement from lateral views. Consequently, there exists significant need to improve existing optical diagnostics or to develop new ones capable of providing these measurements. In the next section, we briefly review some conventional and advanced techniques for liquid sheet thickness measurements found in the literature, their advantages and shortcomings.

1.4.1 Intrusive technique for thickness measurements

To surmount theoretical modeling difficulties and for comparison with experimental results, Dombrowski et al. (1954) [15] were obliged to measure the thickness distribution in radial and circumferential directions of a flat fan spray sheet. For doing so, a small section of liquid sheet was collected through a narrow slit in a collection box.

The slit was formed by two thin blades attached to the tapering walls of the box on which were placed two outlets (figure 1.14a). When the slit is brought into contact with the liquid sheet, the razor blade splits the liquid sheet into two streams. The thickness of the sheet was then determined from the measured flux output and the known slit dimensions, assuming that the velocity of the sheet to be equal to $\sqrt{2gP/\rho}$.

The similar approach was used by Bush and Hasha [21] to measure the mass flux within a sheet produced by impinging jets. The apparatus used by Bush and Hashashown is shown in figure 1.14b. A razor blade mounted on a vertical and horizontal traverse splits the fluid chain into two streams. Measuring the partition of fluxes in a series of horizontal positions allows the flux profile $Q(\theta)$ to be reconstructed. The angle between the

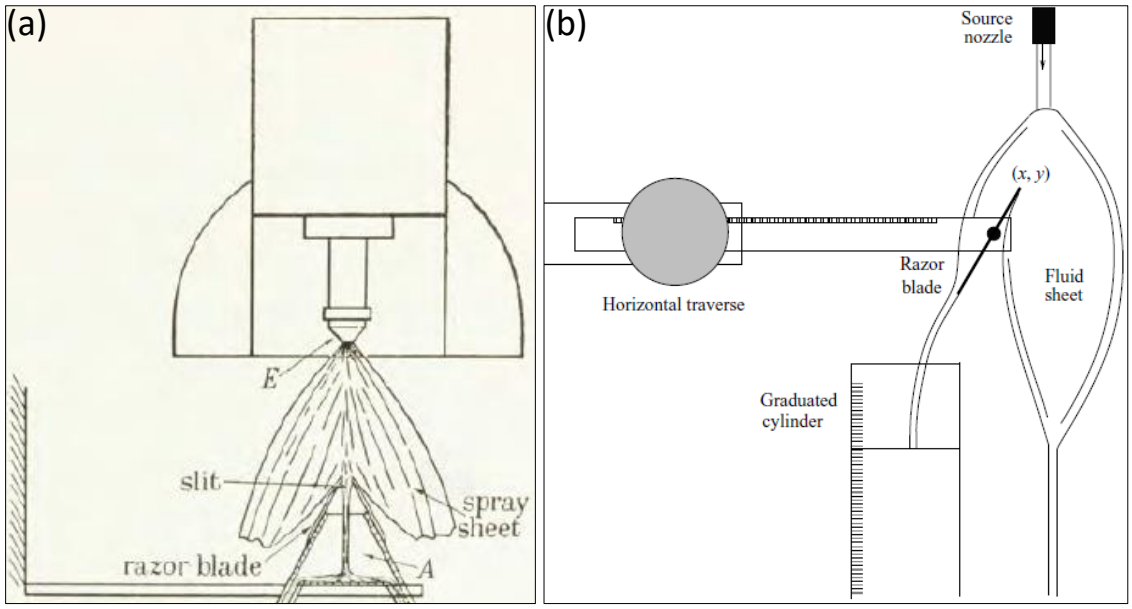

Figure 1.14: (a)Apparatus for determination of liquid sheet thickness. [15](b)The similar apparatus implemented by Bush and Hasha (2004) [21]

line joining the tip of the razor blade to the origin and the sheet centerline is defined to be θ.

Both methods are simple but also have disadvantages in the sense that the insertion of a flow measuring device disturbs the flow itself and additionally the liquid velocity must also be known or hypothesized to estimate the sheet thickness from these techniques.

1.4.2 Non-Intrusive technique for thickness measurements

Interferometry: The most common non-intrusive optical techniques utilized for liquid sheet thickness characterization are based spatial interferometry. Dombrowski et al. (1960) [14] used light interference phenomenon to measure the liquid sheet thickness distribution. The interferometric method entails that when a monochromatic light beam falls on a thin film, reflection takes place from the front and back surfaces, as shown in figure 1.15a. These reflections interfere with each other because of the difference in their optical paths. Consequently, interference fringes appear on the sheet surface, which are directly related to thickness distribution along the liquid sheet.

The film thickness increment Δh between two adjacent bright or dark fringes is given by

$$\Delta h = \frac{\lambda}{2n \cos \phi_r} \tag{1.4.24}$$

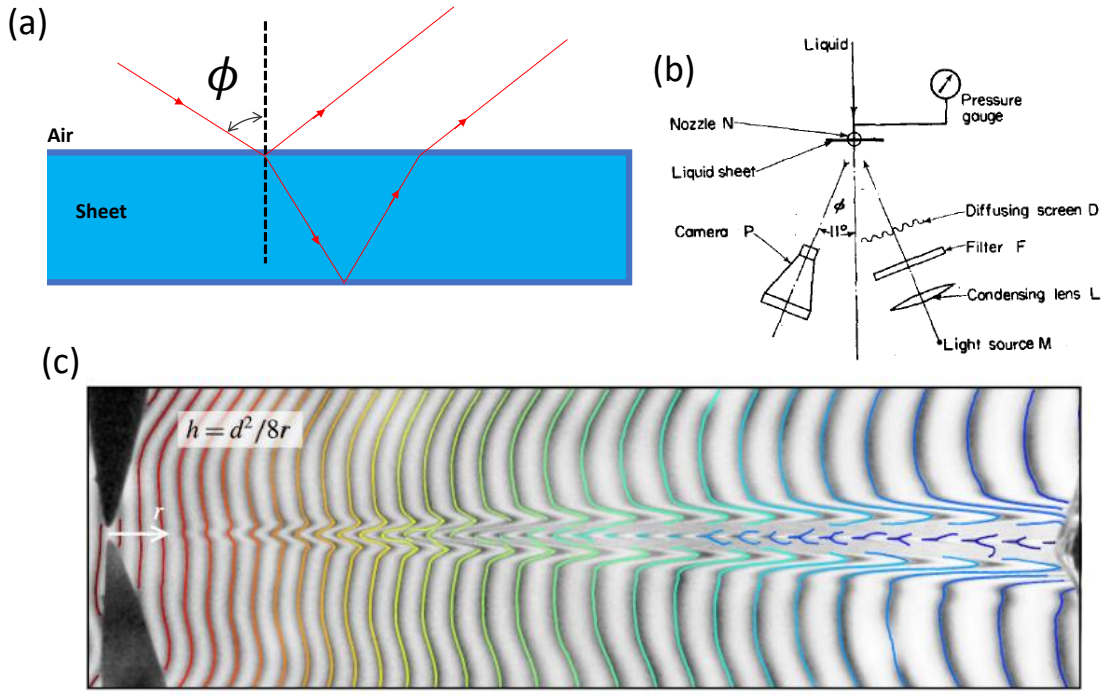

Figure 1.15: (a) Interference of light rays in a thin sheet. (b) The optical setup employed by Dombrowski et al. (1960) [14] to record the fringe patterns. (c) Typical interferometric picture. Each dark fringe is a line of iso-thickness, separating from the following by a constant $h \sim 0.25\ \mu$m. A reference is needed, generally where the film is unperturbed [25]

with n the refractive index of the liquid, λ is wavelength of the incoming light and ϕ_r the phase angle inside the sheet. The apparatus employed by Dombrowski et al. (1960) [14] to record the fringe patterns is shown in figure 1.15b. It consists of a mercury vapor lamp (250 W) as a light source, whose light is condensed by lens L and transmitted through a mercury yellow filter F and diffusing screen D to the liquid sheet. The reflected light is photographed by the camera P. The same approach was used by many researchers in recent years [25, 133]. The typical interferometric picture showing dark and bright fringes is displayed in figure 1.15c [25]. Shen et. al. (1998)[134] used the same principal of interferometry with holographic imaging for measuring thickness variation of a liquid sheet formed by two impinging jets.

The main constraint of this technique is that it is a relative measurement. One can obtain the variation of the thickness along some paths but not the absolute value of the thickness. Also, the interface must be smooth enough for the technique to work.

Terahertz time-domain spectroscopy (THz-TDS): With the recent advancement in optical diagnostic tools, researchers have developed new techniques. Kondoh and

Tsubouchi [26] developed a Terahertz time-domain spectroscopy (THz-TDS) technique. When the Terahertz (THz) pulse passes through a liquid film, the phase delay and the attenuation of intensity are detected in the transmitted THz electric field. By measuring the temporal profile of a THz pulse with and without the film [$E_S(t)$ and $E_R(t)$] respectively, the complex transmission spectrum η is.

$$\eta(\nu) = \frac{E_S(\nu)}{E_R(\nu)} = \frac{4n(\nu)}{\{n(\nu)+1\}^2} \exp\left\{-i\frac{2\pi\nu h}{c}(n(\nu)-1)\right\} \frac{1-\left[\frac{n(\nu)-1}{n(\nu)+1}\exp\left\{-i\frac{2\pi\nu h}{c}n(\nu)\right\}\right]^{2N}}{1-\left[\frac{n(\nu)-1}{n(\nu)+1}\exp\left\{-i\frac{2\pi\nu h}{c}n(\nu)\right\}\right]^{2}} \tag{1.4.25}$$

$E_S(\nu)$ and $E_R(\nu)$ are the frequency Fourier transform of the temporal profiles $E_S(t)$ and $E_R(t)$, respectively. The quantity $n^* = n - ik$ is the complex refractive index of the film, where $n(\nu)$ and $k(\nu)$ are the refractive index and the extinction coefficient, respectively. h is the thickness of the sheet and N is the number of the multiple reflections [135]. By knowing the spectra η of different measurements, the sheet thickness h can be determined from equation (1.4.25). Figure 1.16a shows the THz waveforms as a function of collision angle of two jets for THz pulse transmitted through a liquid sheet produced by the colliding-jet sheet. The corresponding thickness obtained from equation (1.4.25) is portrayed in figure 1.16b.

One of the major limitations of THz imaging is due to the high absorption rate of polar liquids, especially water. The absorption coefficient of water is as high as 250 cm^{-1} at 1 THz. Here, the absorption coefficient determines how far into a material light of a particular wavelength can penetrate before it is absorbed. The absorption coefficient depends on the material and also on the wavelength of light which is being absorbed. This property limits the sensing capabilities of thickness in the range of 50 to 120 μm. Another limitation is due to the very high technicalities associated with the emission and reception of THz waves.

Infrared spectromicroscopy : Recently, Koralek et al.[27] developed a technique for measuring the thickness of ultra-thin liquid sheets based on infrared imaging. They have imaged the liquid sheets using an Agilent Cary 620 FTIR microscope fitted with a $\times$15 all-reflective objective (NA = 0.62) and a 128×128 HgCdTe pixel-array detector. This system simultaneously captures Fourier transform infrared (FTIR) spectra on each detector pixel, giving us a spatial map of the IR spectra for the entire sheet. Figure 1.17a shows image of the total integrated IR transmission.

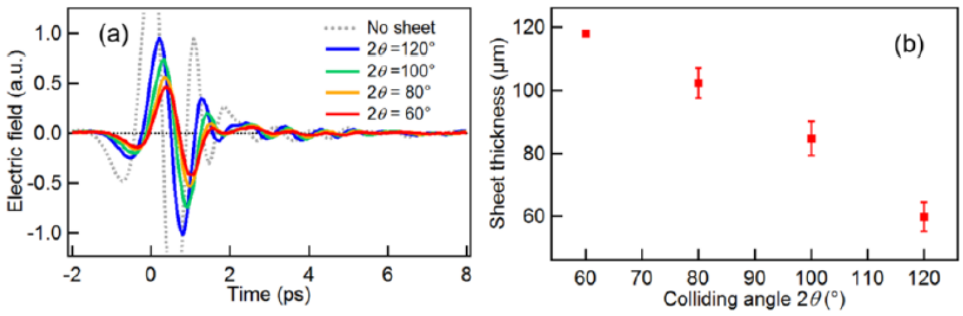

Figure 1.16: (a) THz waveforms as a function of collision angle for THz pulse transmitted through a liquid sheet produced by the colliding-jet sheet. The measurement point was 5 mm downstream from the impingement point for different colliding angle of the jet. (b) The sheet thickness as a function of the collision angle.[26]

With the use of Fourier transform infrared (FTIR) absorbance spectra, one can apply Beer-Lambert law to obtain the liquid sheet thickness.

$$\text{Absorbance} = \log\left(\frac{I_0}{I}\right) = \epsilon h c \tag{1.4.26}$$

where ϵ is the molar absorptivity, c is the molar concentration of water the (55.5 mol.l^{-1}), and h is the sheet thickness. The limitation of this method is that the sheet must be no more than a few microns thick (i.e. more precisely between say $10nm$ and $\sim 1\mu m$) in order to readily transmit IR radiation.

Summary: We therefore dispose of a panel of different intrusive and non-intrusive thickness measurement techniques. Each of these methods has advantages and disadvantages. We summarize their features in table 1.1.

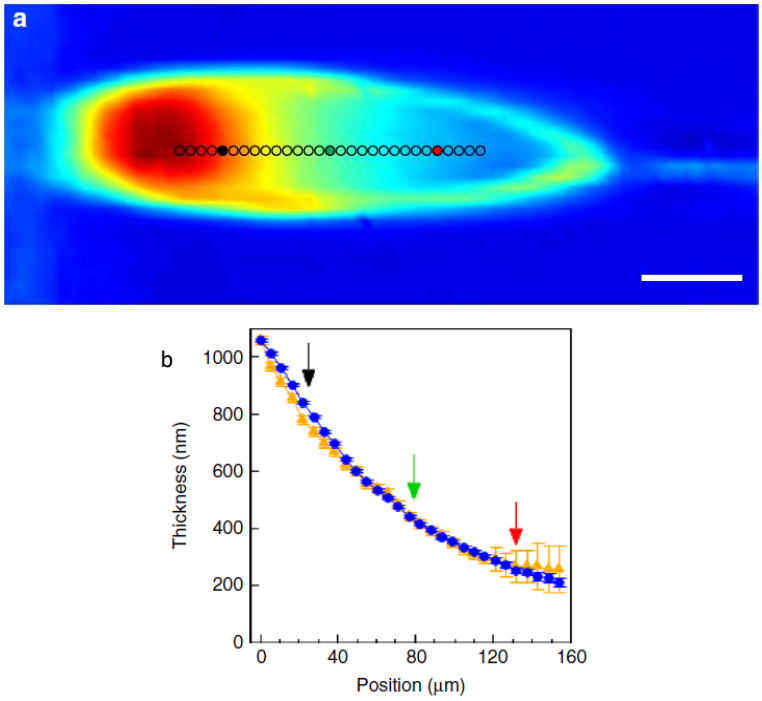

Figure 1.17: (a) Infrared spectro-microscopy of ultra-thin liquid water sheets, a color image of the integrated IR transmission through a water sheet. (b) The calculated sheet thickness along the central region of the water sheet with infrared spectro-microscopy. The error bars in (b) represent an estimate of the uncertainty on the absorption measurement based on the signal-to-noise ratio of the peaks of interest. [27]

1.5 Imaging

The development of optical diagnostics for dense sprays faces many obstacles: (i) off axis multiple scattering (ii) small field of view (or area of interest) (iii) high velocity of the liquid jet (iv) high optical depth. Measurements in the downstream dilute spray region are possible using various conventional imaging techniques such as back-light illumination [65], light scattering [68], structured laser illumination planar imaging (SLIPI) [69, 70]. Table 1.2 shows summary of classical imaging techniques with their advantages and disadvantages for spray characterization.

When spray is illuminated by transmission of light through it, the light undergoes different interactions (scattering, diffraction, reflection and refraction) as shown in figure 1.18a-b before arriving at the detector. Due to off-axis multiple scattering, the obtained images encounters reduced visibility. Until recently, it has been sometimes impossible to differentiate liquid and gas phase i.e. the local textural content of the images between the light transmitted directly to the camera which have very low textural content to the one

Table 1.1: Summary of conventional and advanced thickness measurement techniques in the context of flat liquid sheet characterization

Techniques	Advantages	Disadvantages
Flux distribution method	(i) Very simple setup (ii) not expensive	(i) intrusive method which disturbs the flow (ii) sheet velocity must be known a priori
Spatial interferometry	(i) simple non-intrusive method (ii) whole-field measurements of sheet thickness.	(i) absolute value of thickness cannot be obtained (ii) interface must be smooth enough for the technique to work (iii) sometimes clear fringes could not be obtained due to intrinsic speckle noises
Terahertz time-domain spectroscopy (THz-TDS)	(i) Advanced technique with absolute thickness measurement (ii) Thickness measurement in the range of 50-120 μm	(i) The absorbance of THz light limits the range of thickness measurement. (ii) very specific equipment
Infrared spectroscopy	(i) Advanced technique with absolute thickness measurement (ii) Thickness measurement in the range of 10 nm-1μm	(i) The method is applicable for extremely thin sheet in limited range. (ii) very specific equipment

which travelled through the liquid which have a larger textural content (see figure 1.18c). Subsequently, it is difficult to extract the flow characteristics such as liquid structures and their breakup dynamics through the obtained images.

Owing to complexities of these problems, during the last few decades, great efforts have been devoted to the development of advanced optical techniques featuring ultra-fast lasers and X-ray radiation to suppress the off axis multiple scattering. X-ray absorption based imaging technique used on dense spray formation region provides many parameters such as average mass distribution of liquid [136, 137], flow dynamics and velocity flow field [138, 139]. However, it is generally hard to locate liquid/gas interface with X-ray absorption since X-ray phase contrast interpretation is not straightforward.

Table 1.2: Summary of classical imaging techniques in the context of non reactive spray characterization

Classical imaging techniques	Advantages	Disadvantages
Imaging with continuous illumination and high speed camera	(i) Very simple optical setup (ii) Studying time evolution of spray characteristics for every single injection is possible.	(i) Motion blur for high speed sprays (ii) corrupted image due to multiple scattering of light.
Imaging with pulsed illumination and a CCD camera	(i) Motion blur could be reduced (ii) High image resolution.	(i) Acquisition rate limited by the repetition rate of the ultra-fast lasers. (ii) Laser speckle degrades clarity. (iii) Reduced visibility due to multiple scattering of light.
Imaging with ultrafast lasers and high speed camera	(i) Motion blur is suppressed (ii) Time-evolution of the spray characteristics could be studied. (iii) Acquisition rate not limited by the laser source anymore.	(i) Laser speckle degrades clarity. (ii) Reduced visibility due to multiple scattering of light

SLIPI. SLIPI (Structured Light Illumination Planar Imaging) consists in illuminating the flow with a spatially modulated laser sheet and detecting light which has kept its spatial signature [69, 70]. It is a method which allows the surface area to volume diameter (D_{32}) to be measured. However, SLIPI is ineffective when the optical depth of the spray, OD ≥ 6 [28]. Here, the optical depth can be obtained by using the Beer-Lambert law:

$$\kappa = \frac{I_l}{I_0} = e^{-OD}, \tag{1.5.27}$$

where κ is fractional transmission through medium ($\kappa \leqslant 100$), I_0 is the irradiance (in W/m^2) of the light before it enters the medium, I_l is the irradiance after the light has traveled through a distance l in the medium. OD can also be expressed as follows

$$OD \equiv N\sigma_e l. \tag{1.5.28}$$

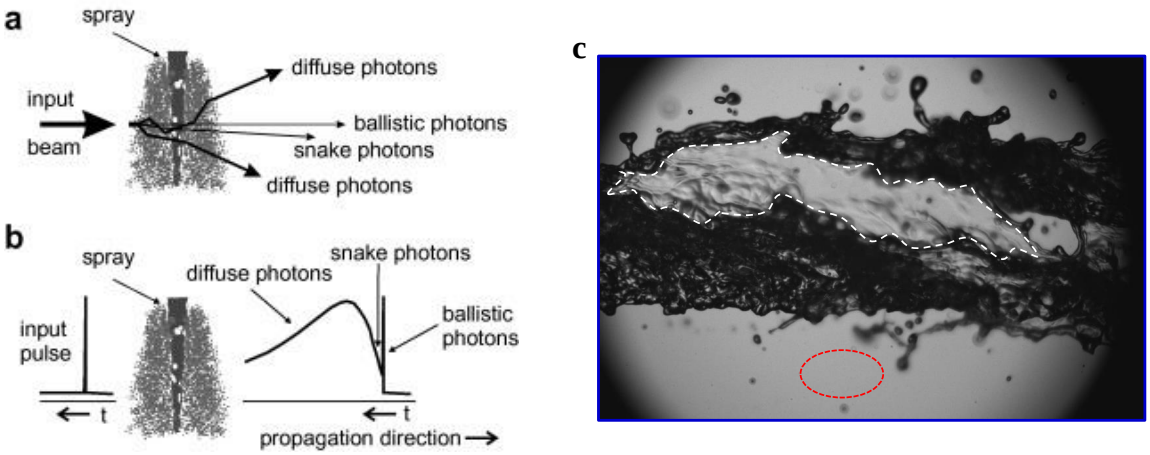

Figure 1.18: Schematic of ballistic, snake and diffuse photons. (a) Geometric dependence, and (b) time dependence [28]. (c) Instantaneous image of spray emanating from triple- disk atomizer showing the similarity of liquid and gas phase. The white dashed line indicates the contours of liquid lamella appearing in liquid core and red dashed line indicates gas phase, highlighting the similarity of grey level between the liquid and gas phase.

Here, N is is the number density of interacting drops and /or molecules per unit volume (scattering or absorption, in m^{-3}) encountered by the stream of photon, σ_e is the extinction cross section (scattering and/or absorption, in m^2)for each interaction. More generally, we write σ_e in terms of cross sections for absorption and scattering: $\sigma_e = \sigma_{absoption} + \sigma_{scattering} \simeq \sigma_{scattering}$ for a spray). l is the path length through the spray. The absorption coefficient for liquid fuel or water is very small at the wavelengths used in optical diagnostic methods. Therefore only scattering can be considered in extinction cross section. A typical value of OD for 1 cm human tissue is 11. However, in terms of spray application OD is defined by the mean number of interactions N also called the mean scattering order.

Table 1.3: Average scattering order for different scattering events

Average scattering order		
Single scattering	Intermediate scattering	Multiple scattering
≤ 1	2-9 (dense spray)	≥ 11 (highly dense spray)

Ballistic Imaging. Our method (which will be described in great details in chapter 3) relies on the working principle of non-linear optical process given by Idlahcen et. al [30] famously known as Ballistic imaging. In terms of spray imaging applications, the utilization of time-

gated ballistic imaging using non-linear optics is mainly focused on contrast enhancement for images of dense poly-disperse sprays. However, to our knowledge, this technique has never been applied to the measurement of the liquid sheet thickness. Hence we here briefly discuss Ballistic imaging, non-linear optical process and second harmonic generation (SHG).

The ballistic imaging is a method that consists in selecting light rays or photons which do not interact with the object and thus retaining their original optical properties. The photons which do not interact with scatterers at all are called ballistic photons and those photons get weakly perturbed into turbid medium in forward lobe scattering configuration are called as quasi ballistic or snake photons. These snake photons have same spatial signature and they reach the detector at the same time as the ballistic photons. This technique was developed by many researchers [30, 140–143] to visualize the liquid core of a dense spray despite of surrounding droplet cloud.

The imaging photons can be used to image scattering medium if one can sufficiently minimize the contribution of corrupted light. This can be done by emphasizing signatures of useful imaging photon as follows:

- **Spatial filtering:** Only photons with a given directional orientation are selected [144]
- **Polarization filtering:** Only photons with the same polarization as the incoming light are selected [145, 146]
- **Time filtering:** Only photons arriving at a given time are selected [147].

In terms of imaging applications, the latter approach based on time-gating remains the most popular in the literature and has had a renewed interest for imaging high speed phenomenon. The classical crossed-beam configuration for ballistic imaging consists in dividing the incoming laser pulses into a pump and a probe pulse [29]. A schematic of the optical setup proposed by [29] is reproduced in Fig. 1.19.

This technique adopts the special time shutter named the Optical Kerr Effect (OKE). It uses a non-linear optical material (liquid carbon disulfide CS_2 cell) which is capable of delivering 1.8 ps gating time. The probe pulses passes through the spray and then reaches the Kerr medium which is activated by the pump pulse. The temporal delay between the pump and probe pulses is adjusted using a delay stage to make sure that they arrive at the Kerr medium at the same time. The pump pulse induces a transient birefringence in the Kerr medium which rotates the polarization of the probe beam and allows a part of

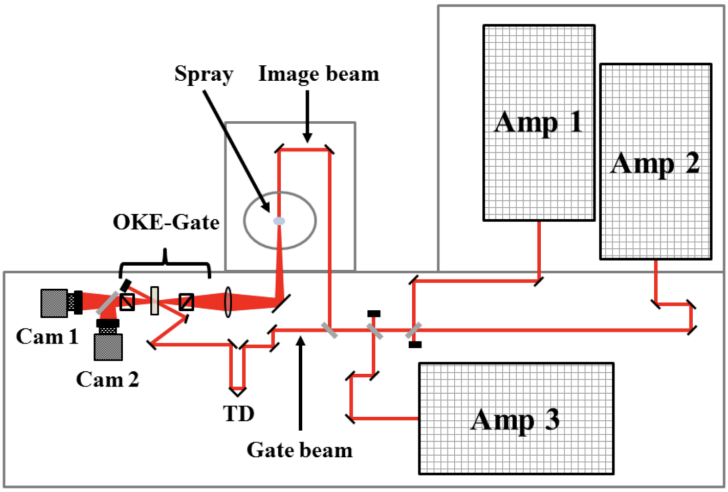

Figure 1.19: Schematic of the optical setup used by [29]

it to pass through the crossed polarizer. The problem with the classical crossed-beam configuration is the non-collinear overlap between the pump and probe pulses inside the Kerr medium due to the finite beam sizes and the angle between them. The imaging spatial resolution degrades significantly due to inhomogeneous transmission of spatial frequencies through the optical gate. Also, since this configuration (in its primitive form) uses the same wavelengths for pump and probe beams, there is an unwanted noise originating from the scattering of the intense pump beam by the Kerr medium.

To solve these problems, a new optical arrangement was proposed by Idlahcen et. al [30]. The latter is reproduced in Fig. 1.20. It consists in using second harmonic generation in a BBO crystal to convert the probe from λ = 800 nm to 400 nm for probing the sample. The characteristics of the optical time-gate were measured and it was shown that there is a significant improvement in duration of time-gate which is equal to 270 fs. They have shown that some photons experience refractions through the liquid jet and may be delayed by a typical time delay of $\Delta t = \Delta n d/c$. Here, Δn is the difference between the refractive index of liquid and surrounding medium, d is the diameter of jet and c is the speed of light in free space. Figures 1.21a and 1.21b obtained by Idlahcen et.al [148] show a comparison between a ballistic image and a classical shadowgraph. The classical shadowgraph has been obtained using a pulsed white light source (with 2μJ energy and 11 ns duration). The liquid core is only visible in the ballistic image. Thus, with ballistic imaging, one can extract statistics for e.g. the ligament size distributions, the surface curvature distributions[28], the fluid parcel velocity [149] (only possible with multi-pulse ballistic imaging).

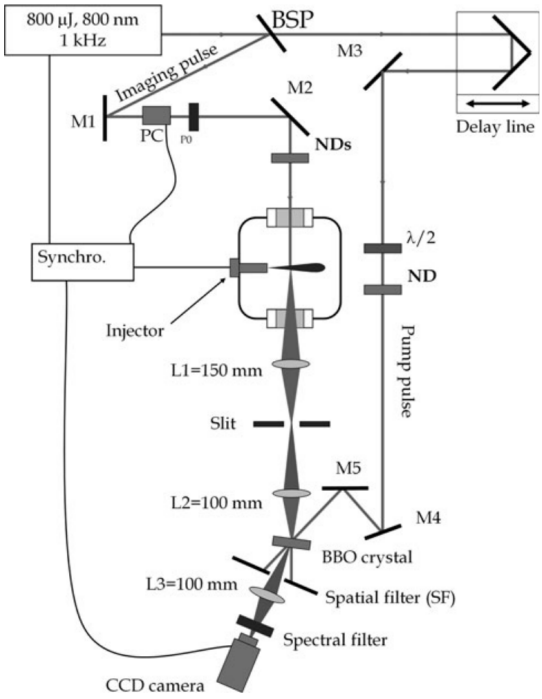

Figure 1.20: Schematic of the optical setup used by [30]

1.6 Summary

The literature review of section 1.2 has highlighted that when exploring liquid sheet flows, the knowledge of the local liquid sheet thickness is of paramount importance. The figure 1.22 shows the different characteristics of liquid sheet atomization which can be correctly interpreted or estimated when the liquid sheet thickness is known. The pyramid shape in figure 1.22 was chosen, not to place this study at the top of the question to solve, but because it shows that it is a progression. Without the foundations, it is impossible to build the rest. However, measuring the local liquid sheet thickness experimentally is very challenging (section 1.3).

Some existing intrusive (section 1.4.1) and non-intrusive (section 1.4.2) techniques has received attention. Each of these methods has advantages and disadvantages. We summarized the features of the various techniques in table 1.2 and showed that there is need of developing new optical technique. In this thesis, a new time-gated thickness method based on the principals of ballistic imaging is proposed.

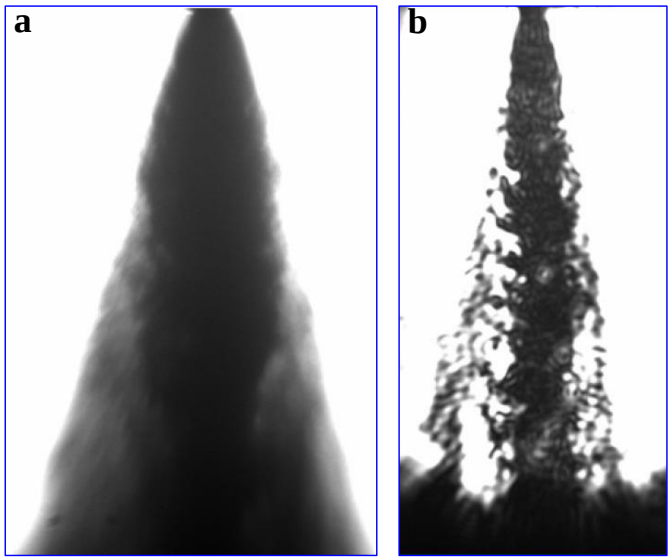

Figure 1.21: Near exhaust of injector visualization. Comparison between ballistic imaging and a classical shadowgraph.

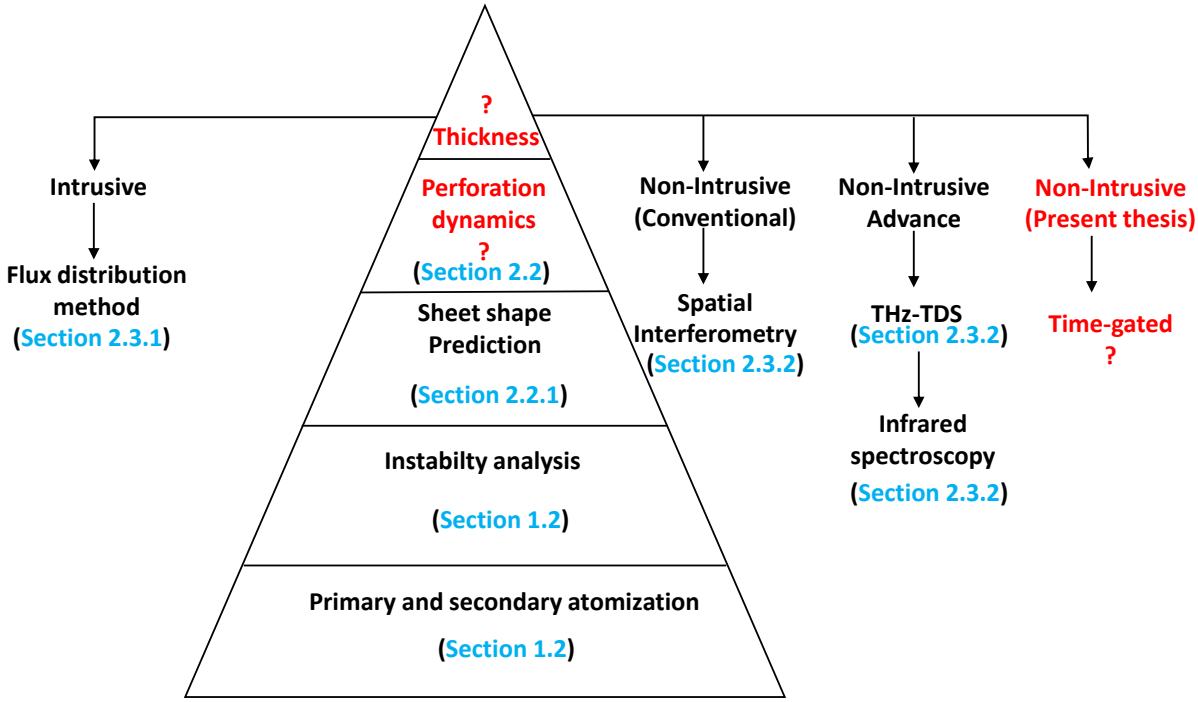

Figure 1.22: Summary of different aspects of liquid sheet discussed in this chapter. (The red font highlighting the objective of the present study to be discussed in forthcoming chapters)

2 | Experimental test facility and optical diagnostics

2.1 Experimental test facility

2.1.1 Flow bench

The experimental test facility is shown in figure 2.1a. This standard assembly comprises two main sections as described below.

(1) A central pipe fitted with a flat fan spray atomizer with an elliptical shape orifice installed in an optically accessible chamber. Here, the liquid sheet was produced using flat fan spray nozzle because they are easier to implement (compared to impacting jets) while retaining the essential break-up dynamics of other sheets (Simplex nozzle used in aero engines). Two different nozzles, denoted A_1 and A_2, are used. They were obtained from nozzle manufacturer company Lechler and correspond to reference 8002E and 8005E, respectively. They are fabricated from brass and have a maximum sheet angle of 80°. The nozzle design is shown in figure 2.1b. The exit passage of the nozzle has V-shaped slot and elliptical orifice. Some microscopic images were obtained to infer the dimensions of the nozzles. The measured orifice major ($2a$) and minor axis ($2b$) dimensions for each injector are given in table 2.2. Throughout the investigation the nozzle was mounted on a 3-axis traverse system having a 0.01 mm minimal displacement.

(2) A Storage vessel (volume capacity 10 liters) to pressurize the liquid with compressed air (gauge pressure 2 bar). Across all experiments, various water-glycerol solutions (0-40 % by volume) were used as a working fluid with dynamic viscosity (μ) ranging from 1-4.78 mPa.s. The liquid flow rate was measured and calibrated for each mixture by

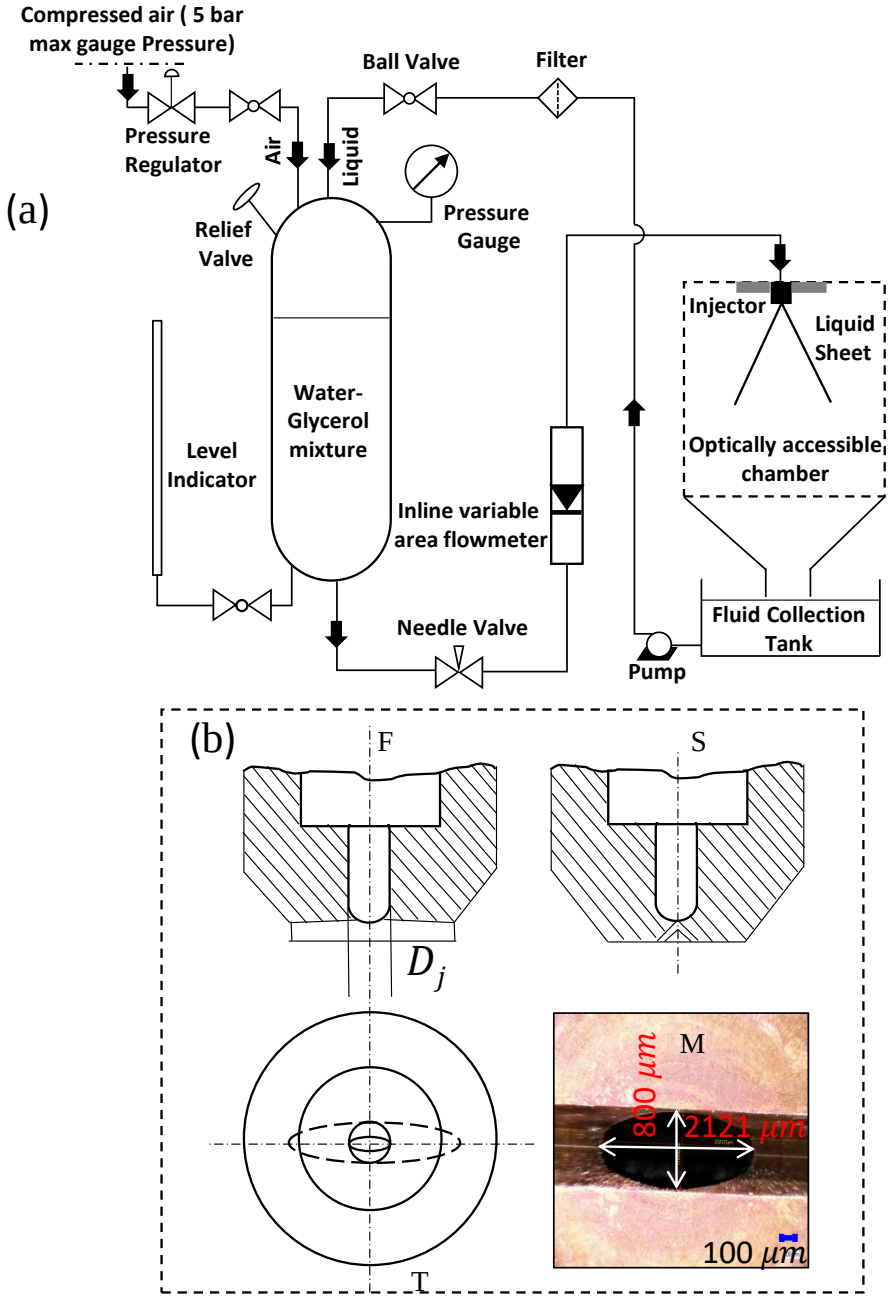

Figure 2.1: (a) Schematic illustration of experimental test facility. (b) Schematic of a cross-section of the flat fan atomizer (F) front view, (S) side view, (T) top view and (M) Micrososcopic image of nozzle orifice A_1 (orifice dimensions are given in table 2.2).

using an inline flow rotameter (range $0.1 - 1.2$ l.min^{-1}). Physical and optical properties of the blends are summarized in Table. 2.1. Surface tension (σ) is measured by the drop volume tensiometer LAUDA TVT 2, whose precision is ± 0.01 mN m^{-1}. The Viscometer Anton Paar V3000 (accuracy 0.01 %) is used to measure the dynamic viscosity (μ), kinematic viscosity (ν) and liquid mass density (ρ). The refractive index (n_l) are taken from National Research Council [31, 150](1933) (see appendix A). It is noticeable from Table 2.1 that increasing the concentration of glycerol in water from F_0 to F_{40} causes a fourfold increase in viscosity while the surface tension, density and refractive index remain nearly constant.

Liquid blend	μ(**mPa.s**)	ν(**mm^2.s^{-1}**)	ρ(**kg.m^{-3}**)	σ(**mN.m^{-1}**)	$\mathbf{n_l}$
F_0	1	1.0068	998.1	71.64	1.33
F_{10}	1.28	1.2463	1012.4	71.07	1.34
F_{20}	1.90	1.878	1038.2	70.86	1.35
F_{40}	4.78	4.324	1100	70.04	1.38

Table 2.1: Thermo-physical and optical properties of various water-glycerol aqueous mixture at 20°C, 1 atm. (subscript 0 to 40 indicates percentage by volume of glycerol in water)

The Reynolds (Re) and Weber numbers (We) are defined as

$$Re = \frac{\rho_l U_b D_h}{\mu} \tag{2.1.1}$$

$$We = \frac{\rho_l U_b^2 D_h}{\sigma} \tag{2.1.2}$$

where the bulk velocity (U_b) is inferred from the imposed flow rate Q and the nozzle orifice area A, viz.

$$U_b = \frac{Q}{A} \tag{2.1.3}$$

D_h is the mean hydraulic diameter defined as

$$D_h = \frac{4A}{P} \tag{2.1.4}$$

Here P is the perimeter of the orifice. For the elliptically shaped orifice, the hydraulic

diameter can be calculated as

$$D_h = \frac{4\pi ab}{\pi[3(a+b) - \sqrt{(3a+b)(a+3b)}]} \tag{2.1.5}$$

The denominator of the equation is Ramanujan approximation for the perimeter of an ellipse, as there is no exact mathematical expression for the perimeter of an ellipse.

Nozzle A_1	**Nozzle A_2**
a = 1.060 mm	a = 0.642 mm
b = 0.400 mm	b = 0.235 mm
P= 4.824 mm	P= 2.9074 mm
D_h = 1.1 mm	D_h = 0.6525 mm
$A = 9.579\times 10^{-7}\ m^2$	$A = 3.344\times 10^{-7}\ m^2$

Table 2.2: Geometrical parameters for nozzles A_1 and A_2 .

Nozzle A_1	**Nozzle A_2**
$Q = 2.75 - 14\times 10^{-6}$ m^{3}s^{-1}	$Q = 1.667 - 8.33\times 10^{-6}$ m^{3}s^{-1}
U_b = 3.24 – 14.73 ms^{-1}	U_b = 4.99 – 24.91 ms^{-1}
Re=830 – 12000	Re=1097 – 8688
We=184 – 5279	We=543 – 6463

Table 2.3: Flow parameter space explored in the present study.

Low injection pressure and low flow rate was chosen as a desirable operating condition for our experiments. The main reasons behind choosing these operating conditions are as follows. As our objective is to obtain the local liquid sheet thickness and study its influence on stability of liquid sheets and perforation characteristics, it is expected to reduce the interactions between the liquid sheet and the ambient air for the stability of the liquid sheet.

2.1.2 Backlight imaging

2.1.2.1 Low frame rate imaging

Conventional backlight illumination technique was employed to study the different topological structures of the liquid sheet and appraise the various flow regimes in the nozzle

near-field region. Figure 2.2 illustrates the arrangement of the backlight imaging system, consisting of a 200W non-coherent laser diode source (Cavitar CAVILUX HF) with tunable pulse duration. The light source has a wavelength (λ) of 640 nm and maximum pulse rate of 100kHz. We use a dye coated diffuser plate to ensure a uniform illumination density.

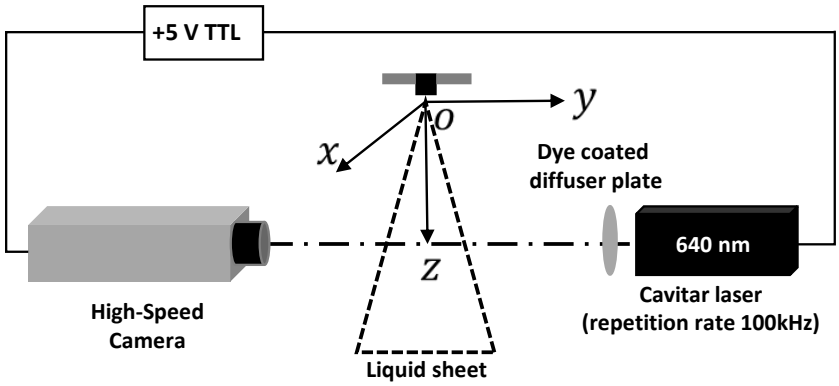

Figure 2.2: Schematic of Back-lit illumination for visualization of liquid sheet.

Images were acquired by a high resolution CCD camera (mvBlueCougar x125aG Matrix vision) with a pixel resolution of 2448 X 2050 pixels (pixel size of 3.45 X 3.45 μm^2). The camera is coupled with a zoom lens (f 16-100 mm) a spatial field of view of 77 $\times$ 87 mm^2 (optical magnification of 0.080).

2.1.2.2 High-speed imaging

Backlit imaging is also employed for high-speed visualizations of the flow, with the goal of measuring the perforation holes kinematics appearing in liquid sheet. We used the same experimental arrangement as the one portrayed in Figure 2.2.

We used two different high-speed cameras. The first camera is a Vision Research CMOS Phantom V2512. It offers a maximum resolution of 1280 $\times$ 800 pixels and a pixel size of 28 μm, which corresponds to a sensor size of 35.8 $\times$ 22.4 mm^2. The camera is coupled with a Nikon zoom lens (f 16-100 mm) with a spatial field of view of 37 $\times$ 60 mm^2. The images are acquired at a rate of 25 000 frames per second at full resolution. The exposure time is set to 40 μs and 1000 images are acquired for each flow condition.

The second camera is a Vision Research CMOS Phantom TMX 7510. It offers 76000 frames per second at full resolution (again 1280 $\times$ 800 pixels). The pixel size is 18.5 μm, which corresponds to sensor size of 23.7 $\times$ 14.8 mm^2. The camera is coupled with a Nikon zoom lens (f 16-100 mm) with a spatial field of view of 23 $\times$ 46 mm^2. The images are

acquired at 80 kHz with a resolution of 1280×640 pixels and the exposure time is set to be to 12.5 μs.

The recorded instantaneous images were further processed in PYTHON (normalization, binarization, contour detection) to determine the kinematics associated with the perforation. The steps involved in the processing will be explained later in Chapter 4 in relevant sections.

2.1.2.3 Image normalization

An image normalization is applied to both conventional and high-speed backlight images in order to correct light source inhomogeneities and shot-to-shot variations. We need two special images to perform the normalization process: the obscurity image I_o taken without any light, and the background I_b. Note that before each injection event a blank or background image was recorded. This was achieved simply by shutting off the injection from atomizer, while the laser and cameras still operate. One can obtain the normalized image I_n from the original raw image as I_m over each pixel of i, j in an image as follows:

$$I_n(i,j) = \kappa \left(\frac{I_m(i,j) - I_o(i,j)}{I_b(i,j) - I_o(i,j)} \right) N_{background} \tag{2.1.6}$$

and

$$\kappa = \frac{I_b(ref)}{I_m(ref)}, \tag{2.1.7}$$

where the subscripts (m, o, b) refer to raw image, obscurity image, and background image, respectively; $N_{background}$ is a normalization factor, which prevents overloaded grey levels in an image. κ is a shot-to-shot correction factor given by the ratio between the average intensity reference level of the source background to the average intensity reference level of the raw image. This intensity reference in Eq. (2.1.7) can be obtained from: 1) The maximum grey level in an image 2) the mode (most populated grey level) of the grey level histogram searched in the background populations or 3) the mean grey value of a region-of-interest (ROI) with no object.

As an example, the recorded back-illuminated liquid sheet image without and with normalization is as shown in figure 2.3a and 2.3b, respectively. By looking at the grey level histogram of the raw and normalized images in figures 2.3c and 2.3f, we see that the background illumination of the normalized image is far less scattered than that of the raw image.

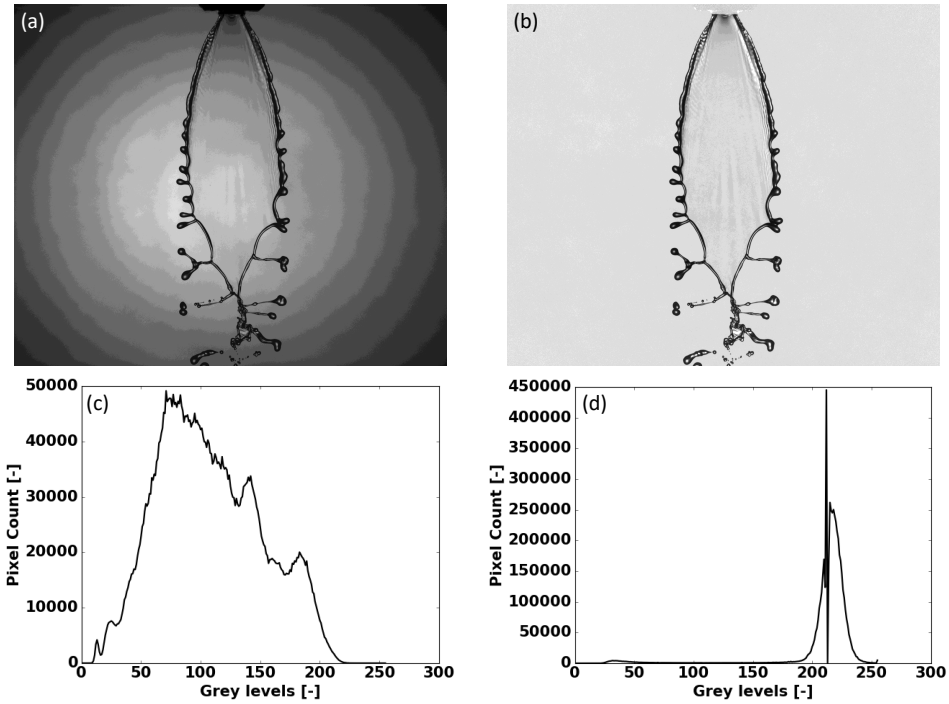

Figure 2.3: Illustration of the normalization process. a) raw image, b) normalized image, c) grey level histogram of the raw image, d) grey level histogram of the normalized image.

2.1.3 Qualitative observations of flow regimes

Before proceeding to time-gated imaging, we first carried out an exploratory qualitative characterization of various stable and unstable regimes of liquid sheet using conventional backlight illumination.

The present section outlines the stable and unstable flow regimes observed when the flow rate is increased. This allows us to assess the relevant flow rates and nozzle diameters that will be used later for measuring the liquid sheet thickness. We seek for testing our newly developed technique in certain conditions: a (1) flat, (2) stable, and (3) not too thin (i.e. with measurable thickness) liquid sheet. Figure 2.4 shows the observed flow patterns with viscosity 4.78mPas (40% water-glycerol) for atomizer A_1 and A_2.

The different flow patterns are governed by two parameters: Re and We. The experimental test cases are represented in a We-Re regime diagram and gathered in figure 2.5. Each symbol in figure 2.5 corresponds to a given glycerol-water solution and a given injector. For instance, the lowermost symbols in the We-Re diagram correspond to the largest viscosity solution with injector A_2 while the uppermost symbols corresponds to water flowing into injector A_1.

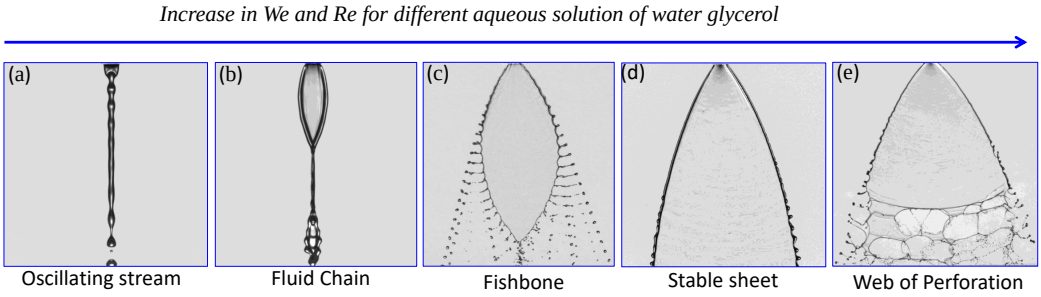

Figure 2.4: Distinct flow pattern produced by Flat fan atomizer for various solutions of water-glycerol.

At the lowest flow rate, the flat fan spray atomizer produces oscillating streams (Figure 2.4a) which results from the action of inertia and capillary effects. The amplitude of these oscillations were examined by Lord Rayleigh (1879) [61] and Niels Bohr(1909) [151] and can be used to measure the surface tension of the fluid.

At a slightly higher flow rate, one observes a fluid chain pattern (2.4b). The physical picture behind this fluid chain is as follows. At first, the liquid sheet develops and a rim is formed which closes upon itself through the influence of surface tension. Then, the rim coming from the two sides collide to form another link in the plane perpendicular to the first and so on. This cascading process of successive links decreases in amplitude through viscous damping and finally the chain coalesces into a single jet. The fluid chain structure is rather similar to the oscillating stream pattern, although it distinguishes substantially by the ratio of the sheet thickness and the rim diameter.

With an increasing flow rate, the structure of bay leaf bounded by a close rim spatially expands to form a smooth sheet with an open rim structure. At this stage the small perturbations on the rim of the sheet start to play and lead to either a stable or weak spluttering rim at its lower extremities. Increasing further the flow rate yields the fishbone structure (Figure 2.4c). Phenomenologically, the fishbone structure can be explained as follows: initially, the Rayleigh-Plateau instabilty with varicose deformations grows to create bulbous regions along the bounding rims. These bulbous regions are thrown outward, drawing out small sub-jets or tendrils under the action of centripetal force associated with curved boundaries of rim. These sub-jets are subjected to capillary instability and thus pinch-off to yield a regular array of droplets in the wake of the sheet. For small diameter nozzle (A_2) the liquid sheet is stable and smooth, but the rim is unstable and form nearly periodic tendrils along of its side. With a slight increase in bulk velocity, the width of

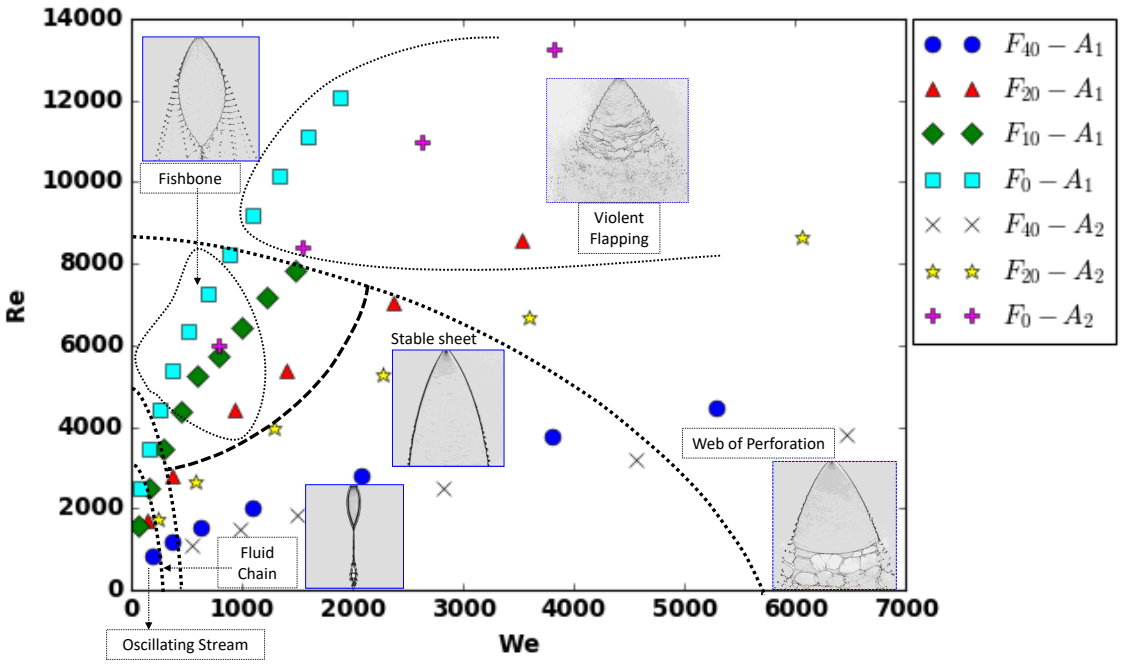

Figure 2.5: Regime diagram demonstrating the various flow pattern produced by a flat fan spray atomizer for various aqueous solutions of water-glycerol (F_0 -F_{40}) for two diameter of nozzles (A_1 and A_2). Six distinct regimes are depicted for range of We and Re (1) oscillating streams (2) liquid chain (3) fishbone (4) stable sheet (5) perforation (6) violent flapping.

fish-bone structures increases while a substantial shortening of the sub-jets occurs. This form persists only a for finite range of flow rates. For comparatively larger diameter nozzle (A_1) the sub-jets are irregular and non-periodic alongside of the rim although the sheet remains nearly stable.

When the flow rate reaches a critical value, some perforation holes start to appear and spread until reaching the rim, thereby forming ligaments and droplets. Multiple ruptures can occur when the flow rate is increased. The various perforation holes can eventually coalesce with each other to form a spider web kind of structure (figure 2.4e).

For low viscosity fluids, at highest flow rate, one observes violent flapping regime characterized by a highly unstable sinusoidal wavy pattern which grows as the liquid film is convected away from the nozzle. This yields a catastrophic sheet break-up [15, 17, 62].

All these flow structures are consistent with previous observations on impinging jets [16, 21, 22, 74, 107, 112]. In the forthcoming chapters, we have made the choice of measuring the liquid-sheet thickness in the stable regime (2.4d). The latter was found in

the range Re_j=2000-6000 and We_j=1500-6500.

2.2 A new technique for measuring the liquid sheet thickness

When a liquid is back-illuminated, the light undergoes optical deviation (refraction, reflection and diffraction) and intensity variations before reaching the detector. Specifically, optical distortions and intensity attenuation can arise when light passes through objects of differing refractive indices (RI's). The optical path difference between a ray of light passing through a thickness h of liquid and a ray passing through the same distance in the surrounding medium is characterized by a time delay

$$\Delta\tau = h\Delta n/c, \tag{2.2.8}$$

as shown in Figure 2.6. Here, Δn is the difference between the refractive index of liquid and surrounding medium and c is the speed of light in vacuum. The thickness of the probed media can thus be measured from $\Delta\tau$, knowing c and Δn.

The time delay $\Delta\tau$ could be detected by selection of the light photons based on their arrival time at the detector. Time gating (time-based filtering) could allow us to select the optical signal within a short temporal window and hence measure the delay due to the passage of light through the object.

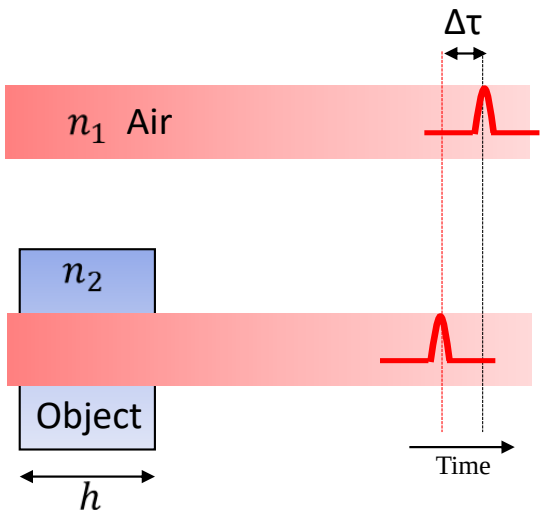

Figure 2.6: The time delay $\Delta\tau$ due to rectilinear propagation of the light in media with different refractive indices

However, the time gate must be very short (~ 10's ps) in order to capture the useful

signal. It is nearly impossible to achieve such a small-time resolution even with any fastest electronically controlled devices. For instance, practical electronic modulation is generally limited to nanosecond timescales, although advances in photo diodes or photo-multipliers have shown that it may be possible to gate at a few hundreds of picoseconds [152]. Non-linear optical phenomena such as Raman [153], Second Harmonic Generation(SHG) [30, 154, 155] and Optical Kerr Effect (OKE) [29, 142, 156] can allow sub-picosecond events to be detected. For imaging applications, the OKE remains the most popular approach in the literature and has received a renewed interest for imaging high speed transit phenomenon. Our method relies on the working principle of SHG (Idlahcen et. al [30]). To our knowledge, such a technique has never been applied to measure liquid sheet thickness.

In the following sections the SHG is described in a detail and the new measuring technique for the liquid sheet thickness is presented.

2.2.1 Second Harmonic Generation (SHG)

The aim of this section is to present the few basic concepts to understand how SHG works and how it can be used to measure $\Delta\tau$ and hence h.

Nonlinear optics is the discipline in which the electric polarization of the medium is studied as a nonlinear function of the electromagnetic field of light. Non-linear interactions are generally observed at high intensities similar to those generated by lasers. The electric polarization field $\mathbf{P}$ will depend on electric field $\mathbf{E}$ generally described as:

$$\mathbf{P} = \varepsilon_0 \left(\underbrace{\chi^{(1)}\mathbf{E}}_{\sim P_{(L)}} + \underbrace{\chi^{(2)}\mathbf{E}^2 + \chi^{(3)}\mathbf{E}^3}_{\sim P_{(NL)}} + ... \right), \tag{2.2.9}$$

where ε_0 is the vacuum permittivity, $\chi^{(1)}$ is the linear susceptibility, $\chi^{(2)}$ is the second-order susceptibility (describing phenomena such as the Pockels effect, optical rectification and SHG) and $\chi^{(3)}$ is the third-order susceptibility (describing third-order effects such as the Kerr effect and electric field-induced optical rectification).

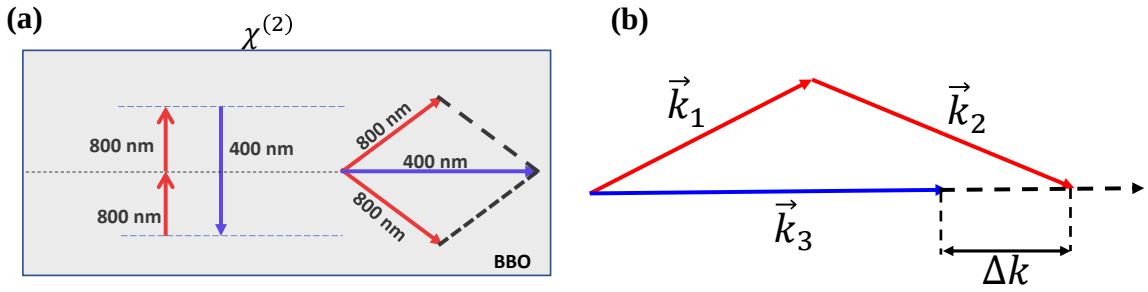

Figure 2.7: Schematic of Second Harmonic Generation in BBO (non-linear Crystal). (b)Phase matching for non-collinear incident waves

SHG is a nonlinear optical process in which two photons with the same frequency interact in a nonlinear material, "combine" and generate a new photon with twice the energy of the initial photons. It is a special case of sum-frequency generation. The wavelength of the SHG signal is exactly half of the wavelength of the incident primary beam, as shown in figure 2.7a.

The simplest case for analysis of SHG is two plane waves of amplitude $E(\omega)$ traveling in a nonlinear medium in directions of the wave-vectors $\vec{k}_1$ and $\vec{k}_2$. If the two incident waves do not propagate in the same direction, a wave with the sum of frequencies is generated in an intermediate direction defined by $\vec{k_1} + \vec{k_2}$. A polarization is generated at the second harmonic frequency

$$P(2\omega) = \epsilon_0 \chi^{(2)} E^2(\omega) \tag{2.2.10}$$

The wave from the generation of the second harmonic has a pulse of 2ω and propagates at speed $c(2\omega)$. If the process is not phase matched, the vector $\vec{k_3}$ is not equal to $\vec{k_1} + \vec{k_2}$. The relation between $\vec{k_3}$ and $\vec{k_1} + \vec{k_2}$ is

$$\Delta\vec{k} = \vec{k}_3(2\omega) - \left(\vec{k}_1(\omega) + \vec{k}_2(\omega)\right) \tag{2.2.11}$$

One can deduce that to obtain maximum efficiency, it is necessary to reduce the Δk difference as shown in figure 2.7b. The intensity is maximized for the phase matched condition $\Delta\vec{k} = \vec{0}$. In other words when two pulses overlap spatially and temporally on the crystal, second harmonic pulse is generated in the direction which is intermediate between the two pulses.

The first nonlinear optics experiment was performed by Franken et al.[157] with frequency doubling in a quartz plate. This experiment consisted of sending radiation of

wavelength 694 nm from a ruby laser on an optically nonlinear crystalline quartz plate and to generate a beam at 347 nm. Since Franken, many nonlinear materials have been discovered and widely explored in the visible and near infrared fields. The most frequently used for second harmonic generation are KDP (Potassium Dihydrogen Phosphate, KH_2PO_4), KTP (Potassium Titanyl Phosphate, $KTiOPO_4$), BBO (beta Barium Borate, β-BaB_2O_4) and LBO (Lithium diborate, LiB_3O_5), whose properties are detailed in Table 2.4 [158].

Table 2.4: Comparison of crystal properties of KDP, KTP, BBO and LBO for second harmonic generation

Crystal	**Domain of transparency** (μ**m**)	**Birefringence**	$\chi^{(2)}$(**pm/v**)	**Damage threshold** (**GW/cm**^{2}) **at 1064 nm**
KDP	0.2-1.5	0.034	0.33	1.0
KTP	0.35-4.5	0.007	5.26	0.44
BBO	0.19-3.5	0.133	1.72	8
LBO	0.16-2.6	0.039	1.40	-

Our experiments use the BBO which offers a good compromise between a wide transparency, a large non-linear coefficient and a high damage threshold. This crystal was discovered in 1985 by Chen et al [159]. It is the most used for the generation of harmonics in Ti:Sapphire, Nd: YAG and argon lasers. It can also be used for mixing frequencies or parametric conversion. This crystal is distinguished by its very wide transparency that extends from IR to UV. Its complete properties are given by Nikogosyan [160].

2.2.2 Measurement of the time-delay using SHG

The method consists of combining an imaging beam (which travels through the medium to be probed, here ultimately the liquid), and a gating beam (a reference that travels only through air) in a nonlinear crystal. When the gating beam coincides in space and time with the imaging beam in the crystal, SHG (doubling in frequency) appears.

If the gating pulse is incident at the BBO crystal at the same time as imaging pulse, the optical time-gate is said to be in an open state (marked by point A in Figure 2.8). These two pulses cross somewhere inside the crystal at an angle θ_n and produce a third pulse at half angle. Placing a camera at half angle allows the SHG pulse to be observed. It will be seen as a bright intensity zone which is related to the cross-correlation of the imaging and

gating beam maximum profiles.

Now, if a medium with a different refractive index is placed on the path of the imaging pulse, the latter will arrive in the crystal at later time. In this situation, the imaging and gating pulses will cross at another location in the crystal, here represented by point D in Figure 2.8. Considering a triangular geometry for the intersection points ACD (see Figure 2.8) leads to relation between the time delay of the imaging pulse $\Delta\tau^{\text{object}}$ and the spatial shift in the crystal Δx^{BBO}:

$$\Delta\tau = 2\frac{\Delta x^{\text{BBO}}\sin(\theta_n/2)}{c/n_{\text{BBO}}}, \tag{2.2.12}$$

where, θ_n is the angle between the two beams inside the crystal and n_{BBO} the refractive index of the crystal. On the camera, the shift from point A to point D will be observed through a pixel shift of Δx^{camera} given by:

$$\Delta x^{\text{camera}} = C_{\text{mag}}\Delta x^{\text{BBO}} \tag{2.2.13}$$

where C_{mag} is the magnification which can be obtained from the camera (described later). If the imaging and gating pulse are travelling horizontally, the pixel shift is observed also on the horizontal axis which means that the light intensity shift measured by the camera detector is function of the horizontal axis only and no variation of the SHG light is expected on the vertical axis. Practically, that means that the SHG profiles measured by the camera detector will be averaged along the vertical axis.

By combining Eqs. (2.2.12) and (2.2.13), we end up with:

$$\Delta\tau = \underbrace{2\frac{n_{\text{BBO}}\sin(\theta_n/2)}{C_{\text{mag}}\,c}}_{K_{\text{cal}}}\Delta x^{\text{camera}}. \tag{2.2.14}$$

K_{cal} is a function of the angle between the imaging and gating pulse, the properties of the crystal and the magnification of the camera. Hence, for a given optical setup K_{cal} is constant. In summary, the method for measuring the thickness of a given medium consists in the following steps:

1. get the constant K_{cal} from a calibration procedure (the latter will be detailed in the next subsection),

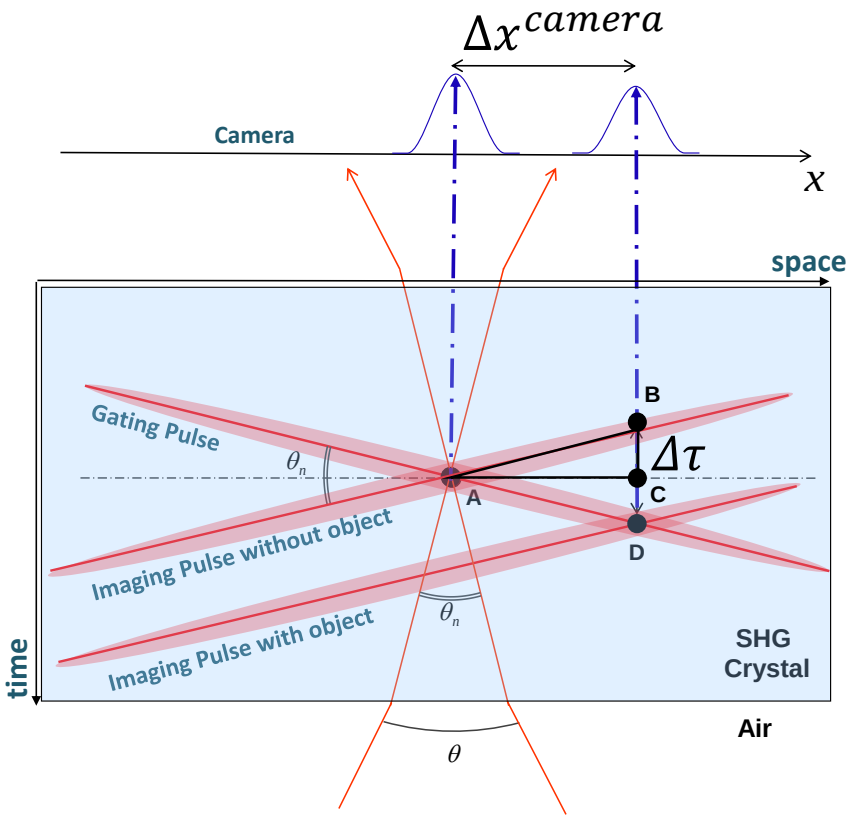

Figure 2.8: (a) Relation between gating pulses and imaging pulse passing through Air (without any object, marked by point A) and object under study (marked by point D). On the image, a pixel located at Δx^{camera} corresponds to a time delay.

2. get the images of the SHG intensity profile with and without the medium on the path of the imaging pulse,

3. measure Δx^{camera},

4. compute $\Delta\tau$ from Eq. (2.2.14),

5. compute the thickness h from Eq. (2.2.8).

Note that contrary to the interferometric technique, the here proposed procedure yields

1. absolute values for the thickness h and does not require a reference point.

2. The other advantages of our technique can be emphasized by expressing the thickness h in terms of pixel shift:

$$h = \frac{c}{\Delta n} K_{\text{cal}}\, \Delta x^{\text{camera}} \tag{2.2.15}$$

This first proves that (2) the relation between the measured quantity Δx^{camera} and the quantity to be measured h is the simplest one could expect, i.e. a linear expression.

3. Further, its slope $\frac{c}{\Delta n} K_{\text{cal}}$ which corresponds the sensitivity of the measuring technique (it can be expressed in terms of μm of liquid per pixel shift) can be varied by playing on the angle θ_n, and/or the magnification C_{mag}. While the former may be unalterable due to some constraints on the optical setup, the latter can however be easily adjusted and optimized depending on the range of thickness values one has to measure.

These are the three main advantages of this new measuring technique.

2.2.3 Proof of concept

2.2.3.1 Optical setup

For testing the measurement protocol, we have designed a first optical setup. A schematic is shown in Figure 2.9a. This setup will be referred to as the single-pass arrangement since the imaging pulse is travelling only once through the medium to be probed.

A laser system (Ti:Sapphire Regenerative amplifier, Coherent Inc.) generates ~100 femto-second (fs) pulses (800 nm, 1 kHz, 3 mJ). A combination of half wave-plates ($\lambda/2$) and a linear polarizer (Pol) is used to control the average power of the pulse. The incoming pulse is divided into imaging (probe) and gating (pump) pulses by means of a 50/50 Beam splitter (BS_1).

We further disposed a computer operated delay stage on the path of the gating pulse. The latter is used to instigate a small delay between the imaging and gating pulses (see Figure 2.9b) as well as to synchronize the imaging and gating pulse to reach at the BBO crystal and produce SHG. The gating pulse time delay ($\Delta\tau^{\text{delay}}$) is related to the displacement of the delay line Δx^{delay} by $\Delta\tau^{\text{delay}} = \frac{2\Delta x^{\text{delay}}}{c}$ (the factor 2 is due to the delay stage that produces one way, one return of the gating pulse). On the camera, an increase in path length of the gating pulse of Δx^{delay}, yields a displacement of the bright intensity zone in the BBO and hence on the camera detector. Repeating the operation for various positions of the delay line allows the constant K_{cal} to be measured.

The SHG intensity and position are detected using a Dantec FlowSense camera which has a maximum frame rate of 44 fps with pixel resolution of 1600 × 1200 (pixel size = 7.4μm). The pulses interval is synchronized with camera shutter speed through TTL signal. A spectral band pass filter (F) is used to removed undesired light. An additional neutral

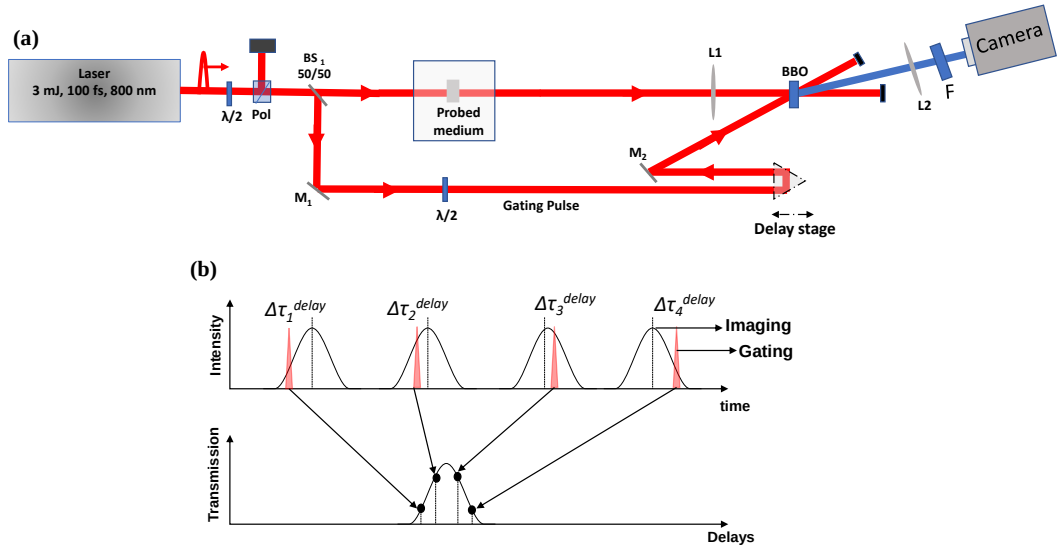

Figure 2.9: (a) Schematic of the optical setup for single pass, SHG based time-gate femtosecond imaging. Nomenclature: (BS_1) - 50 : 50 beam splitter, (M_1, M_2) - mirrors, ($\lambda/2$)-half wave-plates, (Pol) - Linear Polarizer, (BBO) - β-barium borate crystal, (L_1, L_2) - lenses. (F) is a spectral band pass filter. (b) Schematic showing the overlap between the gating and imaging pulse for different positions of the delay line

density filter is used to adjust the intensity of the SHG light reaching the camera.

The imaging beam travels through a wide aperture biconvex lens L_1 and a second lens L_2 is placed between the crystal and the camera. The focal length of these lenses can be chosen to get desired magnification of the object on CCD camera and hence optimize the sensitivity of the measurement system.

2.2.3.2 Evidence of spatial shift for a glass plate

In order to check the feasibility of our measuring technique, we carried out some experiments for a glass plates of known thickness $h = 140\mu\text{m} \pm 10\mu\text{m}$ and known refractive index ($n = 1.51$). Some images were first recorded when the imaging pulse is travelling through air only and the delay line was set to several positions. Results are reported on the top panel of Fig. 2.10. We observe that increasing the path length of the gating pulse (increasing $\Delta\tau^{\text{delay}}$) yields a shift of the bright intensity from the left to the right on the camera detector. We note also that the vertical profile of SHG intensity remains nearly constant, i.e. the pixel shift occurs only in the x-direction. Therefore, we decided to average the images in the y-direction and plot these averaged intensity profiles as a function of the horizontal axis (see Fig. 2.11)

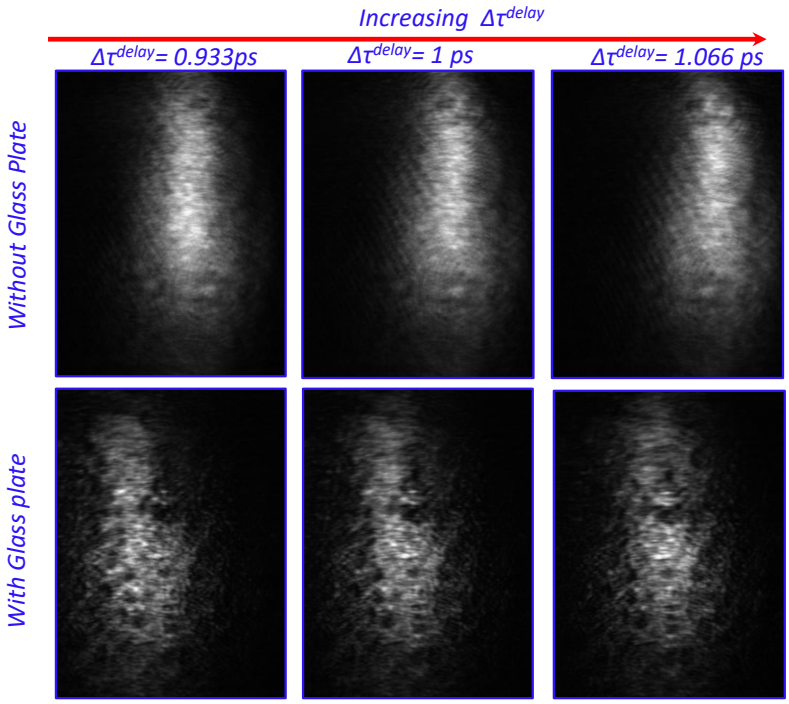

Figure 2.10: Examples of time-gated images obtained through single-pass otical time gate. The relative temporal delay($\Delta\tau$) in picoseconds is shown on each images without glass plate (first row), with glass plate (second row)

If we now place the glass plate on the imaging beam path, we observe again that changing the positions of the delay line yields similar shifts of the recorded light intensity on the camera detector (see Fig. 2.10 bottom panel and Fig. 2.11). This means that the constant K_{cal} remains the same in presence or absence of the glass plate as it is expected from Eq. (2.2.14). However, for a given position of the delay stage, the profiles obtained in presence of the glass plate are shifted to the left when compared to those obtained when the imaging beam is travelling through air only. This shift in pixels can be measured. Now since K_{cal} is known (from the experiments without the glass plate), the time delay due to the passage of the gating pulse through the glass plate can be computed (Eq. (2.2.14)), and the glass plate thickness be measured (Eq. (2.2.8)).

2.2.3.3 Spatio-temporal diagrams

The evolution of SHG signals can be investigated in more details. In previous section, we analyzed the results for 3 given positions of the delay line. However, the analysis can be performed for a wider range of positions in order to construct the full spatio-temporal diagram of the SHG signals.

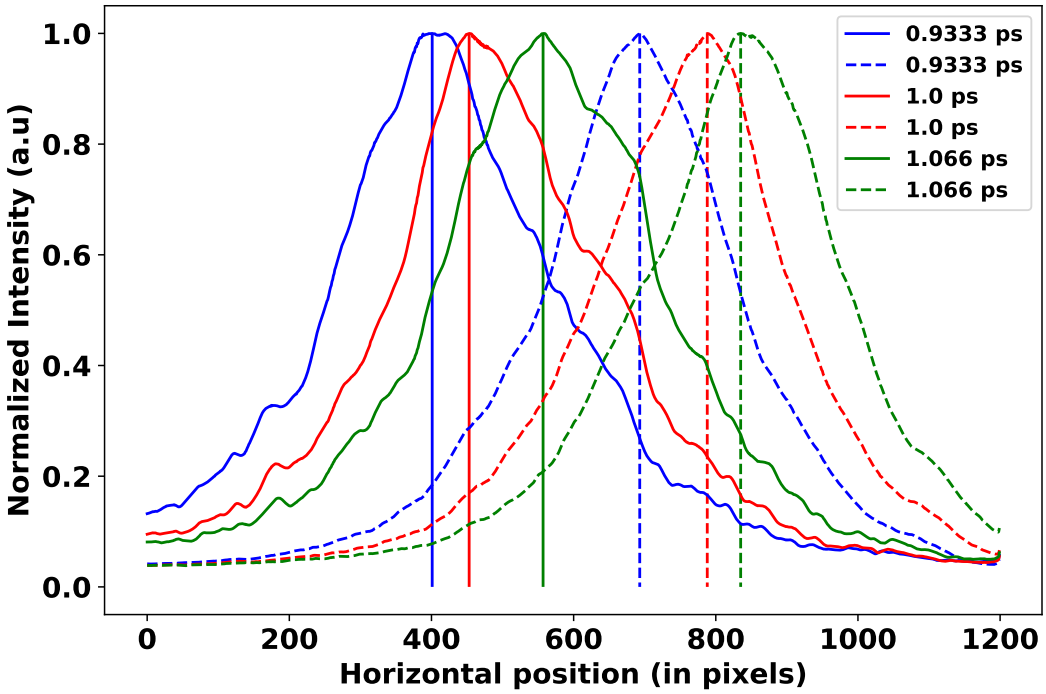

Figure 2.11: Average normalized line intensity profiles for the time-gated images showing the spatial shift for various delays between gating and imaging pulse (Solid line:with glass plate, dashed line:without glass plate)

For doing this, we set several values of the delay line $\Delta\tau^{\text{delay}}$ (generally 10 to 30 different values are used), and for each position, 10 images are recorded to produce an ensemble averaged image. This yields a 3D data cube of the light intensity $I(\Delta\tau, x, y)$ as shown in Figure 2.12(b). As discussed in previous section, only the dependence along the horizontal axis of the camera is taken into account. Hence, the intensity $I(\Delta\tau, x, y)$ is averaged in the y-direction of the images. This leads to the reduction of the information from 3D to 2D maps of SHG intensity as a function of the x-pixel position and the delay line position $\Delta\tau$ (Fig. 2.12(c)). Such spatio-temporal diagrams are plotted in Fig. 2.12 when the imaging pulse is travelling through the glass plate (Fig. 2.12(e)) or through the air only (Fig. 2.12(d)).

Comparing Fig. 2.12(e) and Fig. 2.12(d) yields several observations. First, we note that the slope relating the x and $\Delta\tau$ positions of local maxima of SHG signals are very similar in presence or absence of glass plate. The slope was found to vary by less than 1%. Here again, this behavior was expected from Eq. (2.2.14). We also note that the

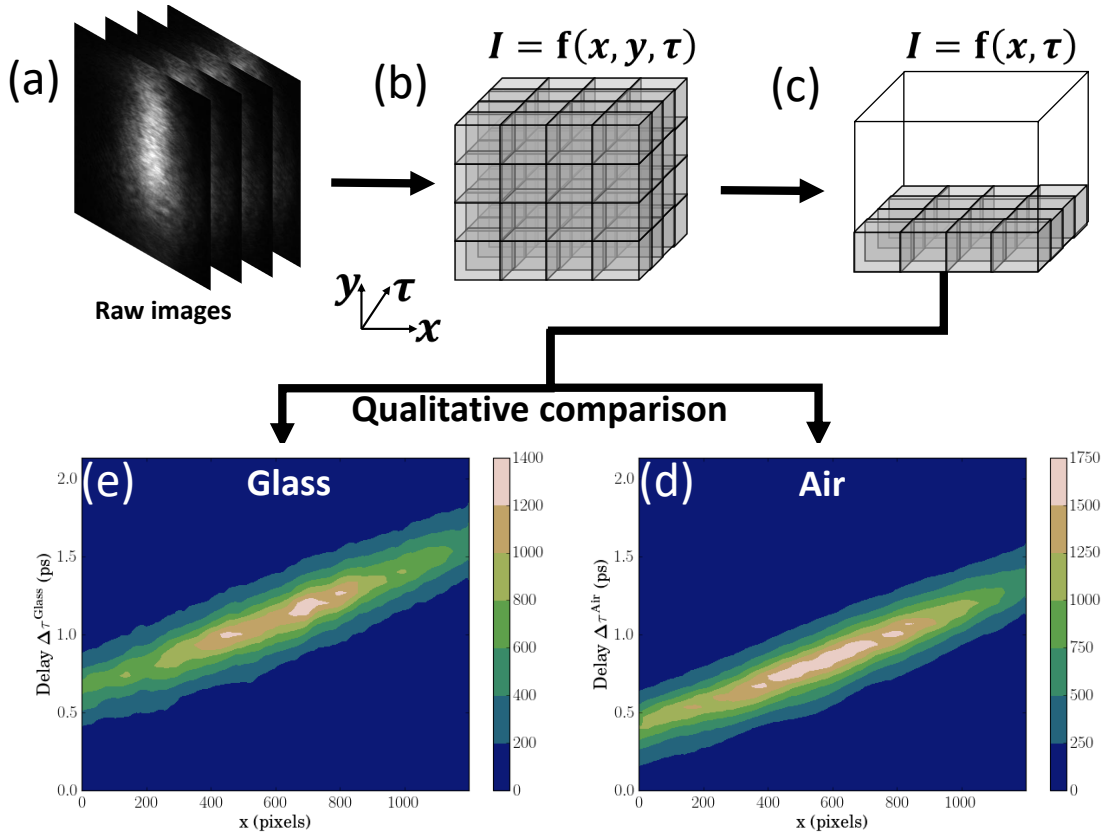

Figure 2.12: Steps involved in spatio-temporal analysis of time-resolved images. The colors indicate the intensity of the light recorded by the camera.

spatio-temporal diagram in presence or absence of glass plate are very similar, except that a shift in the direction of $\Delta\tau$ is observed. For the example reported in Fig. 2.12, the time shift between air and glass-plate is measured to be 0.243 ± 0.002 ps which by virtue of Eq. (2.2.8) gives $h = 143 \pm 1\mu$m. This result confirms that our method for measuring the thickness is accurate. The method for measuring the slope and the time shift will be described later.

2.2.3.4 Post-processing

As said before, the present measurement technique requires a calibration step to infer the value of K_{cal}, which relates the spatial shift [in pixel] on the camera detector to the time delay [in (pico-)second]. The latter can be obtained from the spatio-temporal diagram measured in absence of the medium to be probed, i.e. when the imaging beam is travelling through air only. We have seen in Fig. 2.12, that local maxima in the $\{\Delta\tau\text{-}\Delta x^{\text{camera}}\}$ space fall along a line whose slope is K_{cal}. We have designed different post-processing procedures to estimate this coefficient. They are detailed below.

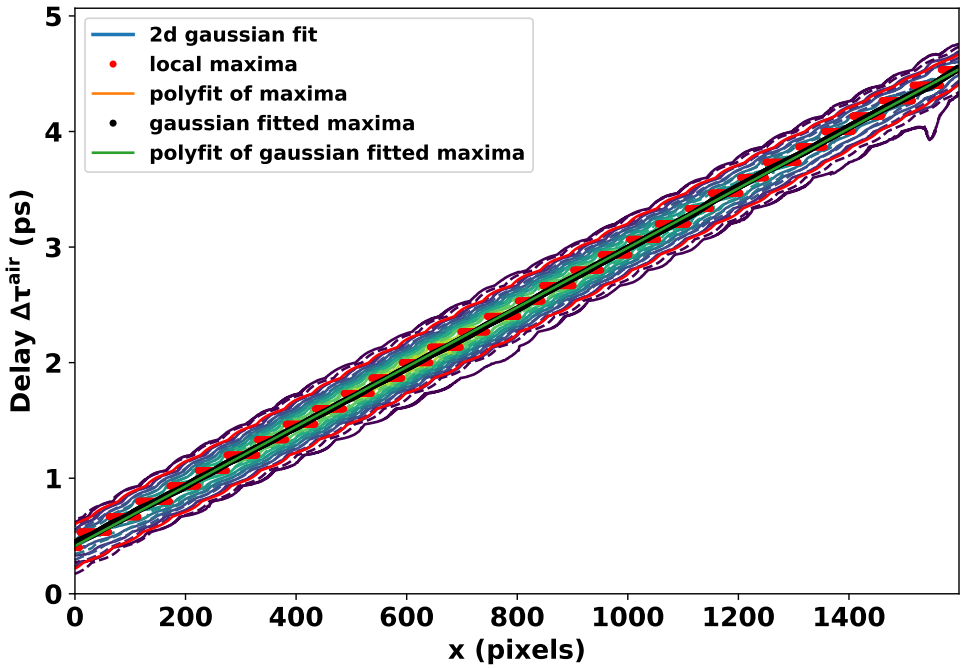

Figure 2.13: The different methods fitted on spatio-temporal diagram of air

- The "brute-force" method. This method consists in extracting the location of maxima along the $\Delta\tau$ axis for each pixel position x^{camera}. The latter are then linearly interpolated to provide the value for the slope and intercept. An example is given in Fig. 2.13 where local maxima are displayed by the red circle symbols. We note that local maxima are distributed in the form of a staircase shape. This is explained by the discretized number of positions that have been set for the delay line. Despite this behavior, the linear fit (orange line which is hidden by the other lines) appears to fit well the experimental data.

- The "1D-Gaussian fit" method. The second method consists in refining the estimation for the maxima positions along the $\Delta\tau$ axis. In this goal, for each pixel position x^{camera}, the SHG intensity profiles are fitted using a Gaussian distribution. The latter was found to be appropriate for representing the experimental results (more details are given later in section 2.3.1 and Fig. 2.17 in particular). This fit yields values for the Gaussian distribution maximum and dispersion. Once the maxima are known, they are again linearly interpolated to infer the slope K_{cal}. In fig. 2.13, we represented the results for the same example as before. The fitted positions of the SHG profiles

maxima are displayed by the black circle symbols. We observe that this method avoids the staircase distribution that we had previously with the "brute-force" method. Linearly fitting the maxima positions yields the green line which is indistinguishable from the one obtained by the "brute-force" method.

- The "2D-Gaussian fit method". The third method consists in fitting directly the SHG distribution with a 2D Gaussian distribution. In a 2d {x;y} space, the latter writes

$$I(x,y) = A\exp\left(-a(x-\mu_x)^2 + 2b(x-\mu_x)(y-\mu_y) + c(y-\mu_y)^2\right) \tag{2.2.16}$$

Here, μ_x, μ_y is the positions of the maximum of the distribution and A is the amplitude of the distribution. The parameters a, b, c are given by

$$a = \frac{\cos^2\Theta}{2\sigma_x^2} + \frac{\sin^2\Theta}{2\sigma_y^2} \tag{2.2.17}$$

$$b = -\frac{\sin 2\Theta}{4\sigma_x^2} + \frac{\sin 2\Theta}{4\sigma_y^2} \tag{2.2.18}$$

$$c = \frac{\sin^2\Theta}{2\sigma_x^2} + \frac{\cos^2\Theta}{2\sigma_y^2} \tag{2.2.19}$$

where σ_x, σ_y is the dispersion of the distribution along x and y, respectively. The fitting procedure allows the six parameters $A, \mu_x, \mu_y, \sigma_x, \sigma_y, \Theta$ to be estimated. The slope is related to the angle Θ by $K_{\text{cal}} = -\arctan(\Theta)$. The 2D fitted distribution are represented as dashed lines in Fig. 2.13. It fits very nicely the experimental distribution. For the example of Fig. 2.13, the slope given by this method is very close to the two previous cases.

For the three aforementioned methods, we have tested the effect of changing the pixel range $(x_{\min}, x_{\max})$ over which the different fits are performed. It was found that the difference on the estimated slope was marginal (of few per thousands) for most of the cases we will present afterwards in Chapter 4. The difference between the 3 methods was also found to be very small, again of the order of few thousandths.

Once the slope is known, the spatial shift of the SHG profile between the air and the medium to be probed needs to be estimated. For this purpose, we compute the cross-correlation between the air and the medium signals and seek for the maximum of this cross-correlation.

An example is shown in Fig. 2.14. The (normalized) profiles of detected SHG when

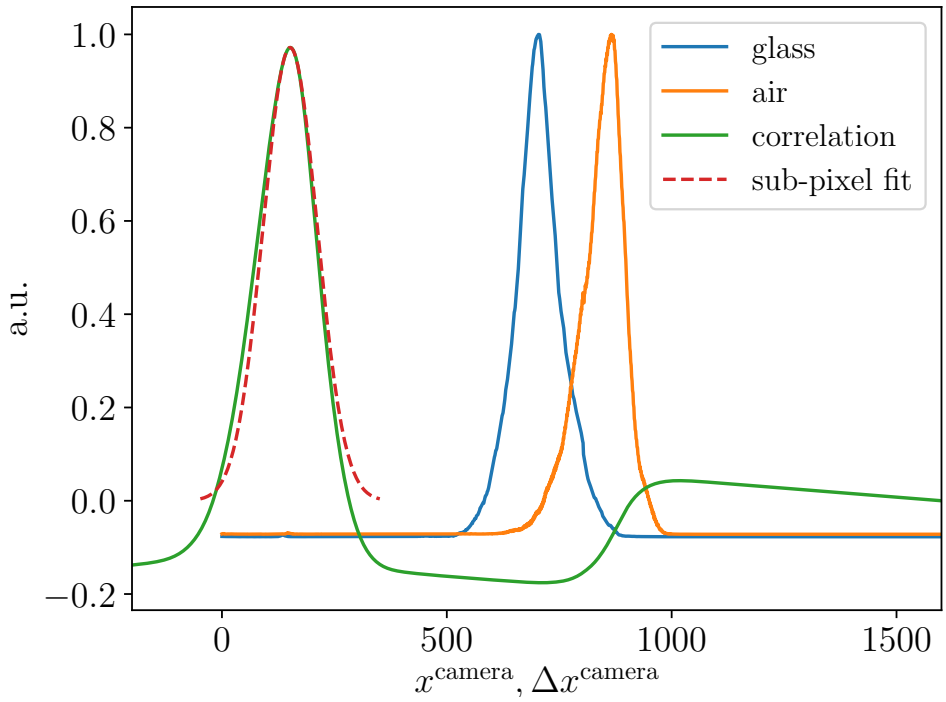

Figure 2.14: Intensity profiles in air and in the glass plate. Also shown are the cross-correlation and the Gaussian fit which is used for sub-pixel resolution.

the imaging beam is travelling in the air and in the medium (glass) are plotted as the blue and orange lines, respectively. Noticeable is the pixel shift. The cross-correlation between these two profiles is shown by the green curve in Fig. 2.14. For the example presented here, the cross-correlation is maximum for a pixel shift of about 160 pixels. As it is done for Particle Image Velocimetry, we can improve the accuracy with which we estimate the position for this maximum. Here, we fit the cross-correlation using a Gaussian distribution in the vicinity of this maximum which allows some sub-pixel resolution to be obtained. The fitted distribution is shown in Fig. 2.14 by the dashed red curve.

2.2.4 Limitations of the single-pass setup

When the imaging beam is interacting with a medium of very small thickness, the spatial shift (Δx^{camera}) can possibly be too small for being measured. Increasing the sensitivity of the measuring technique by increasing the magnification factor can provide a solution, but this solution holds true only up to a certain point. Indeed, for very small medium thickness, the spatial shift becomes very small compared to the width of the intersection between the

imaging and gating pulse. The shift Δx^{camera} thus becomes tenuous to measure. The width of the intersection can be reduced by playing on the angle θ but, again, this may apply up to a certain point.

Another disadvantage of this setup is its low spatial resolution. The BBO is placed at the image plane of the lens L_1, due to the small value of the angle θ (effect of angle is described in appendix B.1), there is a lot of noise due to the scattering of high-power gating pulse through the SHG medium and in this configuration there is no way to filter out this noise.

If the SHG medium is placed at Fourier plane of the lens L_1,the time-gated signal (bright intensity zone) does not shifts from left to right on the CCD camera when delay is changed, rather the SHG signal stays at same location on the camera with intensity attenuation of bright intensity zone. Besides, this configuration leads to an inhomogeneous transmission of spatial frequencies through the optical gate. The higher spatial frequencies can be cut off and this constrains the achievable imaging spatial resolution. Therefore placement of SHG medium at the image plane of L_1 is necessary for improving the imaging spatial resolution and obtain the spatial shifts. We need to find the ways to optimize the trade off between the angle θ, spatial resolution and temporal resolution which are discussed in upcoming sections.

2.3 Modified optical setup

2.3.1 Multi-pass loop

To overcome these limitations, we thought of using multiple passes, i.e. the imaging beam is crossing the medium several times before reaching the BBO and interacting with the gating pulse for SHG to be produced. By doing so, the time shift $\Delta\tau$ is also proportional to the number of passes through the medium, thereby increasing the measurement sensitivity.

A schematic of the optical setup for multi-pass SHG-based thickness measurement is shown in Figure 2.15a. Most part of this optical setup remains similar to the previous case. The gating pulse side is exactly similar, and the only modifications were made on the imaging pulse side.

The improvement consists in a loop that the imaging pulse is experiencing before

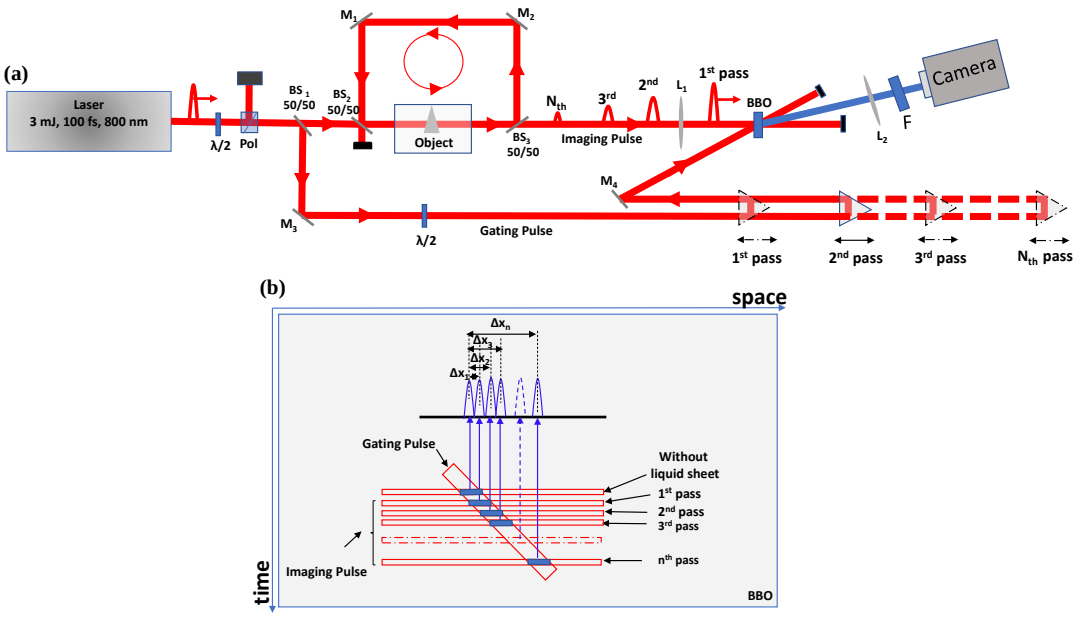

Figure 2.15: (a) Schematic of the optical setup for multi-pass imaging. Nomenclature: (BS_1) - 50 : 50 beam splitter, (M_1, M_2, M_3, M_4) - mirrors, ($\lambda/2$)-half wave-plates, (Pol)-Linear Polarizer, (BBO) - β-barium borate crystal, L_1, L_2) - lenses

reaching the BBO. This loop is obtained by adding two additional beam splitters (BS_2 and BS_3) and two additional mirrors (M_1 and M_2). By doing so, when reaching BS_2, 50% of the imaging pulse is kept and travels through the medium to be probed, the other 50% are reflected and blocked. After crossing the medium, the imaging beam reaches BS_3, 50% of which is reflected towards M_1 and M_2 before reaching again BS_2 to form a loop while the other 50% travels to the BBO. The delay line of the gating pulse can be adjusted on demand to set 1, 2, ..., N passages in the loop, thereby increasing the sensitivity by a factor N. The counterpart of this setup is that the first, second, N pass do not probe the medium at the same time. In our configuration, the distance made by the photons for doing one loop is about 1.2 meters. At the speed of light, the imaging pulse is thus probing the medium every 4 nanoseconds which remains sufficiently small for the flow to be considered as frozen between the different passes.

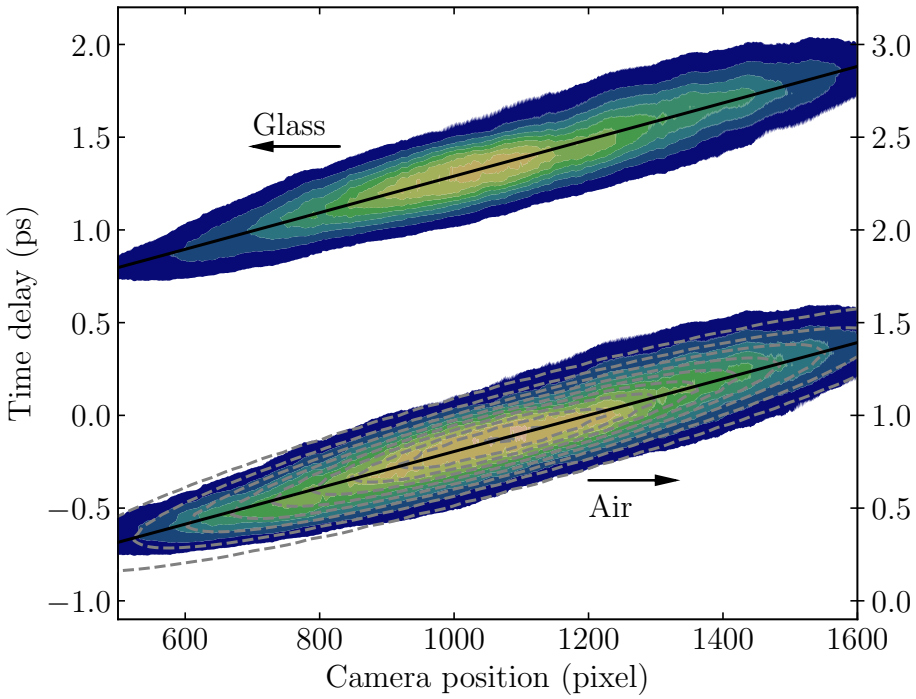

Figure 2.16: Spatio-temporal diagrams in presence or absence of the glass plate using the two loops setup. The right and left axis are translated by a value of 1 ps for enhancing the visual display. The black line represents the linear fit of local maxima of light intensity in the $\Delta\tau^{\text{delay}} - \Delta x^{\text{camera}}$ map. The grey dashed contours represent a 2D gaussian fit.

The spatio-temporal diagrams obtained in presence or absence of glass plate using 2 loops of the mutli-pass loop setup are reported in Fig. 2.16. Here again, local maxima of light intensity in the $\{\Delta\tau^{\text{delay}}; \Delta x^{\text{camera}}\}$ map fall along a line whose slope (the black lines in Fig. 2.16) is the same in presence of absence of glass plate (difference less than a percent). The delay between the SHG signal in air and glass plate $\Delta\tau$ is measured and was found to be 0.482 ±0.004 ps, twice the value of the previous optical setup. This corresponds to a thickness $h = 141 \pm 1\mu m$, i.e. again very close to the expected value.

The cross-correlation of two Gaussian distributions (with mean $\mu_{1,2}$, and standard deviation $\sigma_{1,2}$) yields a Gaussian distribution, with a mean located at $\mu_1 + \mu_2$ and standard deviation $(\sigma_1^2 + \sigma_2^2)^{1/2}$. For testing this, we fit each SHG intensity profile along the different iso-delay lines with a Gaussian distribution and extract the width and center of the distribution. We plot the normalized profile in Fig. 2.17. It is observed that the SHG profiles compare favorably well with a Gaussian profile meaning that the imaging and gating pulse can be considered as Gaussian.

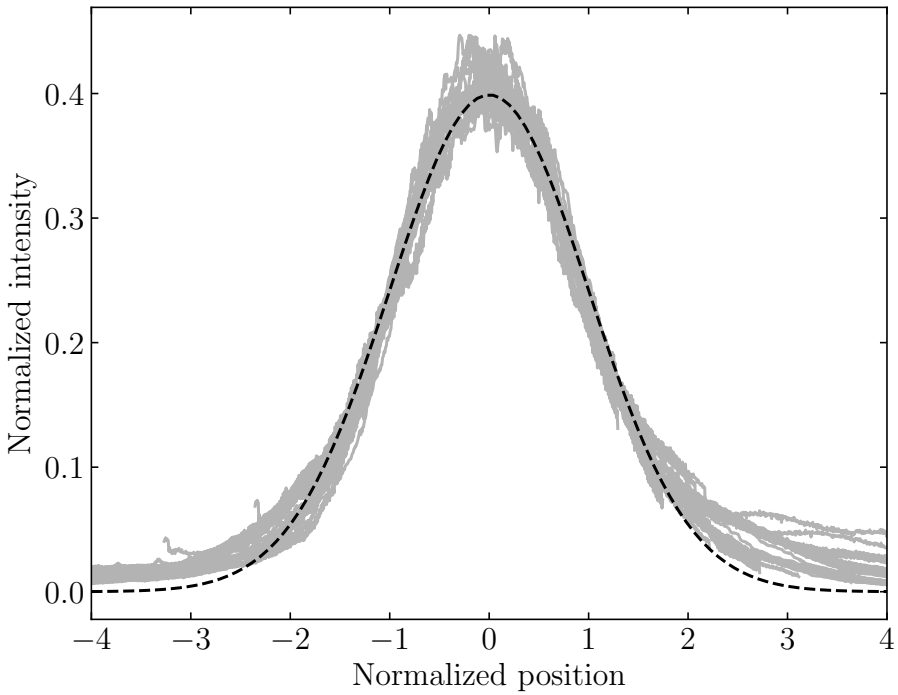

Figure 2.17: Comparison of the normalized intensity profiles along the iso-delay line positions with a Gaussian profile.

2.3.2 Shortcomings of multi-pass loop setup

The problem with multi-pass loop configuration is a significant reduction of the SHG intensity after each loop of imaging pulse. To understand this, consider the initial intensity of the laser beam I_L. Once it passes through first 50/50 beam splitter (BS_1), the intensity of imaging pulse (I_I) and the intensity of gating pulse I_G is given by:

$$I_I = I_G = \frac{I_L}{2} \tag{2.3.20}$$

When the imaging beam travels through BS_2 and BS_3 the output intensity becomes:

$$I_1 = \frac{I_I}{4} \tag{2.3.21}$$

Sequentially, at the second pass I_2 and third pass I_3 the output intensity of imaging pulse is attenuated, and their intensities are given by:

$$I_2 = \frac{I_I}{16}; \quad I_3 = \frac{I_I}{64} \tag{2.3.22}$$

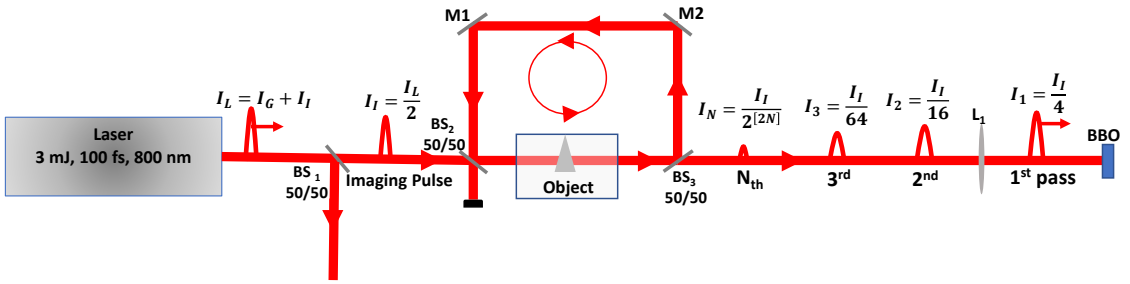

Figure 2.18: Schematic of imaging pulse in multi-pass time gated configuration showing intensity attenuation for each pass of the imaging pulse.

For N loops, the output imaging pulse intensity reads:

$$I_N = \frac{I_I}{2^{2N}} \tag{2.3.23}$$

This sequential reduction of the intensity of the imaging beam compared to the gating pulse yields a significant reduction of the signal-to-noise ratio. For this reason, we have succeeded using the loop configuration with only 2 passes in the medium. Increasing further the number of passes was found to be inappropriate for the SHG signal to be accurately detected.

To overcome the issue of imaging beam attenuation, a novel configuration was designed and developed. The other advantage of the optimized configuration to be detailed in the section below is that it allows the distance made by the imaging pulse between the different passes to be significantly reduced.

2.3.3 Two-pass inline cavity setup

The idea of this optical setup is to restrict the number of passes to 2 which was found to be sufficient for our application while avoiding the attenuation of the imaging beam. This can be achieved using the optical setup shown in Figure 2.19.

This configuration consists using a combination of a rotatable half wave-plate ($\lambda/2$), a linear Polarization Beam Splitter (PBS), and a quarter wave-plate ($\lambda/4$). The working principal is this setup is as follows. Here again, the laser pulse is first divided into an imaging and a gating pulse by using a 50-50% beam splitter. The difference between the previous setup is that the imaging pulse is then travelling through the half wave-plate ($\lambda/2$). The latter allows the polarization of the imaging pulse to be adjusted in such a way that the linear Polarization Beam Splitter reflects the incoming light towards the medium to be

probed. The polarization of this reflected light is then rotated 45° using a quarter wave-plate ($\lambda/4$) before travelling through the medium and reaching a mirror M_1. The light reflected by M_1 is then travelling a second time through the medium, and its polarization is rotated again 45° by the quarter wave-plate ($\lambda/4$). By doing so, the polarization of the imaging pulse has encountered a 90° rotation in total so that it is free to travel through the PBS. The imaging beam is then collected using wide aperture biconvex lens L_1. The focal length of the lens can be chosen to get desired magnification of the object on CCD camera. The imaging and gating pulse are then collocated spatially and temporally in the BBO and the SHG is acquired at mid-angle by the camera.

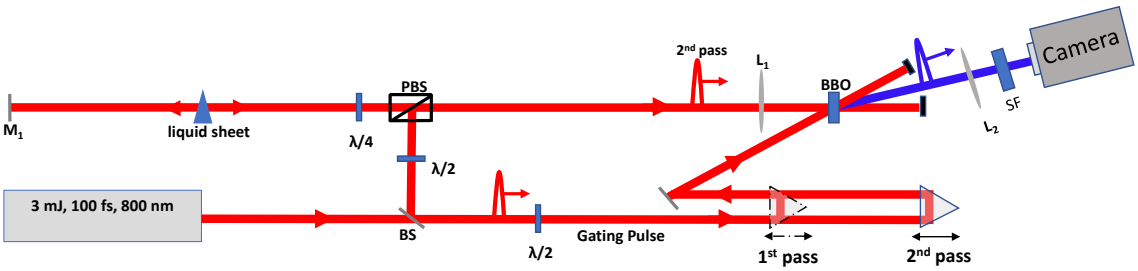

Figure 2.19: (a) Schematic of the experimental setup for multi-pass, the SHG based time-gate femtosecond imaging.Nomenclature: (BS) - 50 : 50 beam splitter, (M_1) - mirror, ($\lambda/2$)-half waveplates, (PBS)-Polarization Beam Splitter, ($\lambda/2$)-quarter waveplates, (BBO) - β-barium borate crystal, (L_1, L_2), - lenses.

The transmission of the imaging beam through the SHG time-gate is given by [161].

$$\frac{I_T}{I_0} = \sin^2\left(\frac{\Delta\phi}{2}\right)\sin^2(2\theta_i) \tag{2.3.24}$$

where I_0 is the incident imaging intensity and I_T is the intensity of the imaging beam transmitted through the optical gate, $\Delta\phi$ is the phase shift experienced by the imaging pulse and θ_i is the angle between the polarization states of the gating and imaging beams. So, the transmitted intensity, I_T is maximum for $\theta = 45°$.

In this configuration, the extra distance made by the photons between the two passes has been divided by 3. Hence, the time between consecutive passes is now reduced to 1-2 nanoseconds which is sufficiently improved compared to the multi-pass setup.

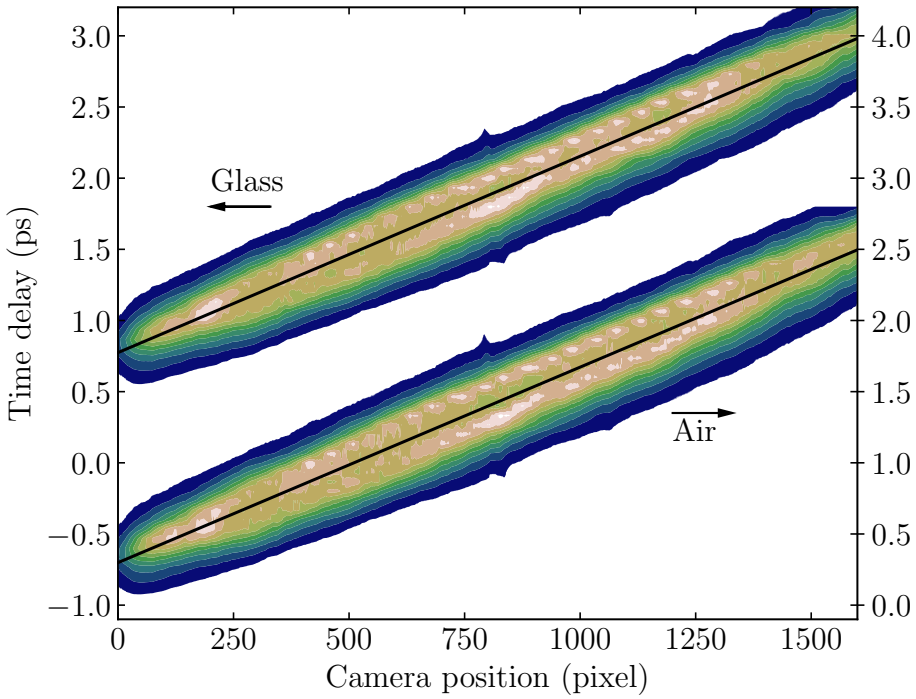

Figure 2.20: Spatio-temporal diagrams in presence or absence of the glass plate using the inline cavity setup. The right and left axis are translated by a value of 1 ps for enhancing the visual display. The black line represents the linear fit of local maxima of light intensity in the $\Delta\tau^{\text{delay}} - \Delta x^{\text{camera}}$ map.

The spatio-temporal diagrams obtained in presence or absence of the glass plate using the inline cavity setup are compared in Fig. 2.20. We note again that these two spatio-temporal diagrams look similar. The one obtained when the imaging pulse is travelling through the glass plate is just the translated version of the one obtained when the imaging pulse is travelling through air. The shift along the $\Delta\tau^{\text{delay}}$ axis is here 0.477 ± 0.002ps yielding $h = 140.0 \pm 0.5\mu$m. Additionally, to check probed medium thickness is nearly constant within the field of view or not, we have done validation of vertical shift which is discussed in appendix B.2. The results obtained for liquid sheet using similar post-processing method is explained in appendix C.

2.4 Femtosecond imaging

The latter configuration can also be slightly modified in order to perform some imaging of the liquid sheet. The problem with liquid objects such as liquid sheets is that the liquid being transparent, there is no sufficient light attenuation in the liquid for being discriminated

from the light that has travelled only through air. The pragmatic consequence is that most segmentation algorithms based on the image grey level intensity are unable to detect the liquid and gas phase. However, the light that has travelled through the liquid hits the camera detector slightly delayed compared to the light that has travelled through air only. Therefore, femto-second time-gating can possibly be used to select the photons that have travelled only through air (or liquid), thereby enhancing the contrast between the liquid and the gas phase. In what follows, we present the proof-of-concept for this method.

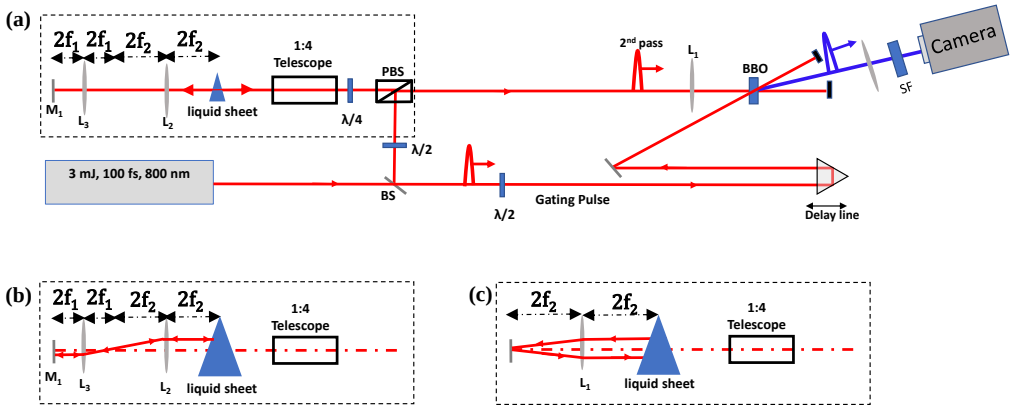

Figure 2.21: (a) Schematic of the setup for double-pass, SHG based time-gate femtosecond imaging. Nomenclature: (BS) - 50 : 50 beam splitter, (M_1) - mirror, ($\lambda/2$)-half waveplates, (PBS)-Polarization Beam Splitter, ($\lambda/4$) waveplates, (BBO) - β-barium borate crystal, (L_1, L_2, L_3) - lenses. (b) Schematic showing the optical path traced by $8f$ imaging setup without offset. (c) Schematic showing the optical path traced by $4f$ imaging setup with offset.

A schematic of the optical setup for large field of view, time-gated femtosecond imaging with the SHG-based time-gate is shown in Figure 2.21a. Here again, most part of this optical setup remains similar to the previous case detailed in section 2.3.3. The main difference between the two setups is in the method of relaying the image to the camera. In this case, after interaction of the incoming imaging pulse with a linear Polarization Beam Splitter (PBS) and quarter waveplate ($\lambda/4$), a 1:4 upcollimating lens pair is used to increase the viewing area fourfold to 15mm x 15mm while allowing a beam size sufficient to overfill the 1600 x 1200 pixel CCD camera sensor.

The imaging beam is directed towards the liquid sheet or the sample under study which results in a given delay in time. The delayed light signal needs then to be focused again to fit the size of the mirror M_1. Here special care should be given. Indeed, if we use only one lens L_1 as in the example shown in figure 2.21c, the light coming from say the left (top) of the field of view will be transmitted towards the right (bottom) of the field of view after being reflected by M_1. This means that, in this $4f$ optical setup, the image captured

by the camera detector will be composed of the superposition of both the image of the liquid sheet and of its mirror symmetry. This makes this setup inappropriate for imaging purpose.

To avoid this, we have designed a double lens setup (also referred to as $8f$ correlator in standard Fourier optics). This arrangement is shown in figure 2.21b. Here, two lenses L_2 and L_3 of 2 inch diameters are used with focal lengths of f_2=300mm and f_3=100mm, respectively. By doing this, we apply a second mirror symmetry which thus cancels out. The imaging pulse is then travelling a second time into the liquid and the remaining of the optical setup is the same as previously.

The near exit of an injector has been imaged using this technique for different flow rates and at different distances from the nozzle. The images are acquired for nozzle A_1 with a water-glycerol solution of 40 %. All the images of the liquid sheet were normalized using the method discussed in section 2.1.2.3. This step is important to enable quantitative comparisons between images of varying laser energy. For instance the time-gated images reduces the available intensity by a factor of about three as compared with non-time-gated backlight illumination. For the smaller flow rate (Re = 1500), the full liquid sheet was reconstructed from two fields of view while at the larger flow rate (Re = 2800), 3 of such fields of view were necessary.

In Figs. 2.22 and 2.23, we compare the image obtained with and without the optical gate. We did experiments for two different flow rates leading to different apparent transparency for the liquid. In particular, in Fig. 2.22 the flow rate is smaller than in Fig. 2.23, which results in a larger value for the liquid sheet thickness in Fig. 2.22 compared to Fig. 2.23. The attenuation of light that passes across a liquid medium is described by the Beer–Lambert law [162]

$$\frac{I}{I_o} = e^{-\mathrm{OD}} \tag{2.4.25}$$

where $I/(I_o)$ is the irradiance of light exiting (entering) the liquid sheet, and OD is the optical depth which is given by:

$$\mathrm{OD} = \sigma_e h \tag{2.4.26}$$

Here, σ_e is the extinction coefficient (via absorption and scattering) and h is thickness of the liquid medium. As the absorption in the liquid is very small at the wavelengths used for time-gated imaging, the extinction coefficient consists of only scattering through the liquid sheet. The equation (2.4.25) and (2.4.26) show that the intensity of the light exiting

the liquid varies with negative exponential of its thickness. Hence, we expect a brighter intensity for larger flow rate.

When the delay is adjusted so that the gating pulse overlap the imaging pulse, refracted or reflected light is no more detected and the liquid sheet appears completely dark. In contrast, when the optical gate is removed, the liquid phase appears almost transparent. Consequently, the liquid sheet can not be easily distinguished from the background, i.e. the local textural content of the image between the light transmitted directly to the camera has almost similar textural content to the one which traveled through the liquid sheet. In summary, without the optical gate, the liquid phase will be hardly distinguishable from the gas phase using conventional threshold algorithms based on the grey levels.

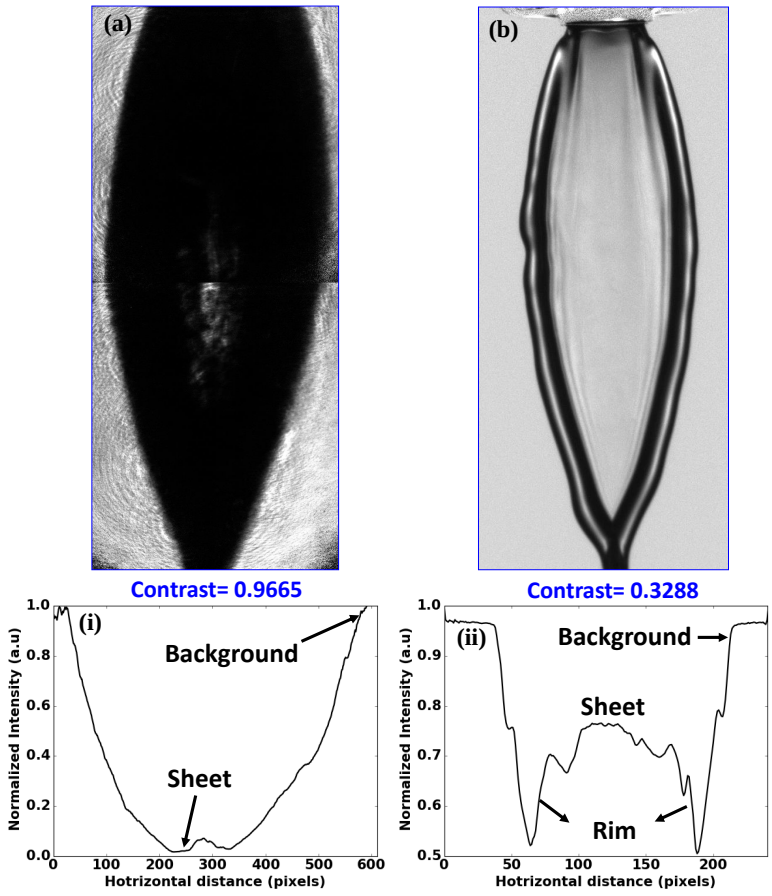

Figure 2.22: (upper row) Comparison between time-gated femtosecond images and non-time-gated classical backlight images at *Re*= 1500 (a) time-gated image (b) non-time-gated image. Intensity profiles for (i) time-gated image and (ii) classical backlight image

We now provide a more quantitative assessment of the image contrast with and

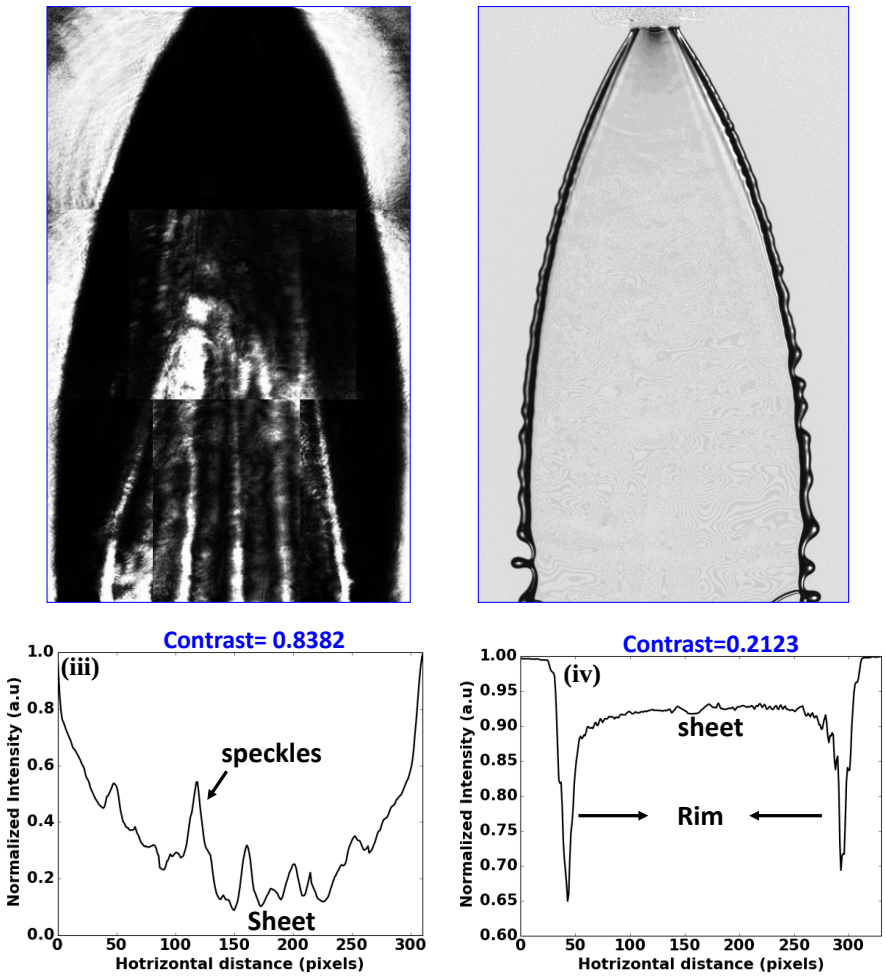

Figure 2.23: (upper row) Comparison between time-gated femtosecond images and non-time-gated classical backlight images at Re= 2800 (a) time-gated image (b) non-time-gated image. Intensity profiles for (iii) time-gated image and (iv) classical backlight image

without the time gate. The contrast C of an image is defined as:

$$C = \frac{I_{max} - I_{min}}{I_{max} + I_{min}} \tag{2.4.27}$$

The intensity profiles of C for the two flow rates considered here are displayed in Figs. 2.22 and 2.23. We also give the global contrast values. At the lower flow rate (larger h), the global contrast between the liquid sheet and background is $\sim$ 30% for classical backlight images, whereas for time-gated, C is significantly improved $\sim$ 90%. However, these values include the liquid rims which have high contrast. In the perspective of practical spray application, while analysing complex liquid sheet lamella the rim cannot be used and the local contrast must be considered (refer to the example given in section 1.5, figure

1.18). The profiles for C reveals that for classical backlit images, the local contrast (without considering rims) is as low as $\sim 4-10\%$ at the level of the liquid film while the values using the optical gate is almost optimal (100%).

At a larger flow rate (smaller h), the contrast of backlight images is even worse, as expected from Eq. (2.4.25). The global contrast falls at 20% while it remains high ($\sim 85\%$) using the time-gate setup. Local profiles also reveal that the contrast can be less than 10% at the liquid film while it is substantially larger with the optical gate (about 90%). It is also worth mentioning that some speckle appears on the time-gated images. This may be caused by the reflection or refraction due to non-uniform thickness distribution of liquid sheet.

In summary, these examples illustrates the potential of the time-gated technique to provide contrasted images of optically transparent medium.

2.5 Summary

This chapter has illustrated a new method for measuring the thickness of semi transparent medium. Inspired by SHG time-gate based ballistic imaging (Idlahcen et al. [30]), the technique consists in measuring the delay the imaging pulse has experienced when travelling through the medium to be probed.

We have started from a single-pass configuration, which was used to provide a proof-of-concept setup. The capability of the method for measuring the thickness of glass plate was demonstrated. Some improvements have then been proposed which consist in convoying the imaging pulse several times into the medium to increase the time-delay and hence the measurement sensitivity.

In this purpose, two distinct setups were developed, the multi-pass loop and inline cavity setups which were tested for 2 passages of the imaging pulse into the medium. An important drawback of the multi-pass loop is the reduction of light intensity after each pass of the imaging pulse. The output imaging pulse intensity I_N after N passes reduces to $I_N = I_I/2^{2N}$ which makes this technique almost unusable for $N > 3$.

We finally decided to restrict to 2 passes and avoid the imaging beam attenuation using the inline cavity setup. It was found that this configuration is simpler to set up since the different beam splitters (BSP) and mirrors are removed. By adding the telescope in the in-line cavity configuration, we have shown that we can also obtain large field-of-view

images with enhanced contrasted compared to the classical backlit imaging technique.

In the next chapter, this measurement technique will be employed to measure the streamwise evolution of liquid sheets for different injectors at varying flow rates.

3 | Thickness distribution and kinematics of perforation

3.1 Theoretical background

We investigate here the variations in the thickness of the liquid-sheet in the stable regime, along the injection axis downstream of the nozzle exit. Our experimental results will be compared to the theoretical model developed by Dombrowski et al. [14]. This model predicts that the liquid sheet thickness is inversely proportional to the downstream distance, i.e. $h = K(z - z_0)^{-1}$ (for complete derivation see chapter 2, section 1.1.2, equation (1.1.7)) where K is a parameter that depends on the nozzle geometry and on the flow regime and z_0 is the position of the center of pressure.

The expression for thickness parameter K is related to the angle α_t that characterizes the sheet expansion as illustrated in Figure 3.1a. Dombrowski et al. derived the expression for K from the boundary conditions at nozzle exit. Indeed, they showed that $K = h \times z = h_0 \times z_0$ where h_0 is the thickness of the orifice exit and z_0 is the origin of the line source of pressure of the flow in the orifice. As shown in Figure 3.1b, the theoretical thickness parameter K_{theo}[1] is given by:

$$K_{\text{theo}} = AB\, z_0 = \frac{AB\, AD}{2 \sin \alpha_t} = \frac{\text{Orifice area}}{2 \sin \alpha_t} \tag{3.1.1}$$

[1]The subscript 'theo' referred as theoretical

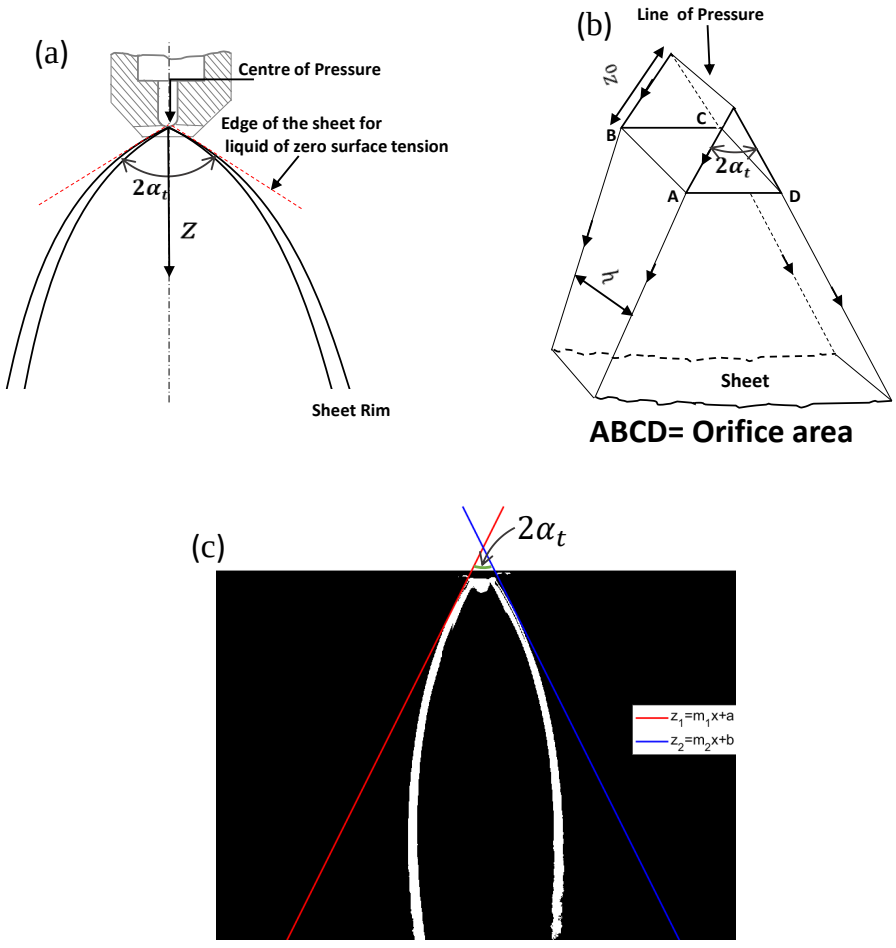

Figure 3.1: (a) Flow pattern in the sheet. (b) flow pattern of liquid upstream and downstream of the orifice [14]. (c) Example of sheet angle calculations for test condition $Re_1 = 1930$: white color region indicating sheet boundaries; linear fitted lines at left and right sides of the sheet contour.

3.2 Evolution of liquid sheet thickness

3.2.1 Experimental protocol

3.2.1.1 Measurements and flow parameters

For measuring the liquid sheet thickness, the inline cavity optical setup was used. The optical setup has been optimized to achieve a sensitivity of about 1 μm of liquid per pixel shift. This value corresponds to the minimum measurable value for the liquid sheet thickness.

Measurements were performed at different downstream locations z on the centerline of the liquid sheet. The liquid sheet issuing from the two injectors A_1 and A_2 were explored.

Injector	A_2	A_2	A_1
Glycerol concentration (%)	40	20	40
Bulk velocity $U_b = Q/A$ (m/s)	11.97	7.73	7.89
Sheet angle at orifice exit $2\alpha_t$ (°)	61.92	48.36	59.48
Reynolds number $Re = \rho_L U_b D_h/\mu_L$	1816	2688	1930
Weber number $We = \rho_L U_b^2 D_h/\sigma$	1400	572	1076
symbol color	red	blue	green

Table 3.1: Flow parameters for the three cases investigated

40% and 20% water-glycerol solutions were used for injector A_2. The corresponding Reynolds numbers are $Re = 1816$ and $Re = 2688$, respectively. For injector A_1, only the 40% water-glycerol solution was investigated which corresponds to $Re = 1930$. These conditions were selected so that the liquid sheet lies in the stable regime. Table 3.1 gathers the main parameters of the flow configurations investigated here. We note that for injector A_2, although the bulk velocity U_b has been decreased from 11.97 to 7.73, the corresponding Reynolds number is increased from 1816 to 2688. This is the result of the strong decrease of the liquid viscosity when moving from 40% to 20% of glycerol concentration. The corresponding Weber number which depends mainly on the bulk velocity since the surface tension is insensitive to variations of the glycerol concentration is decreased from 1400 to 572.

The front and side views for these three configurations are portrayed in Fig. 3.2. It is seen that they correspond to the stable liquid sheet regime. Also superimposed in Fig. 3.2 are the location for the thickness measurement points using the inline cavity setup.

3.2.1.2 Measurements of the sheet angle at the nozzle exit

The sheet expansion angle $2\alpha_t$ was measured at the nozzle exit for different flow rates. For this purpose, a set of images acquired from the backlight illumination technique were first averaged and a binary image is computed from the average image of the liquid sheet. A ROI (Region Of Interest) is selected as a horizontal strip of height $\Delta z = 3$ mm which is shifted vertically from $z = 0$. This small horizontal strip is chosen to minimize the effect from curved boundaries. For each ROI location, a tangential line fitting is performed on the contour of the binary image for each side (left and right). The lines on each side is characterized by a slope m and an intercept c. A gray level threshold is chosen to select the

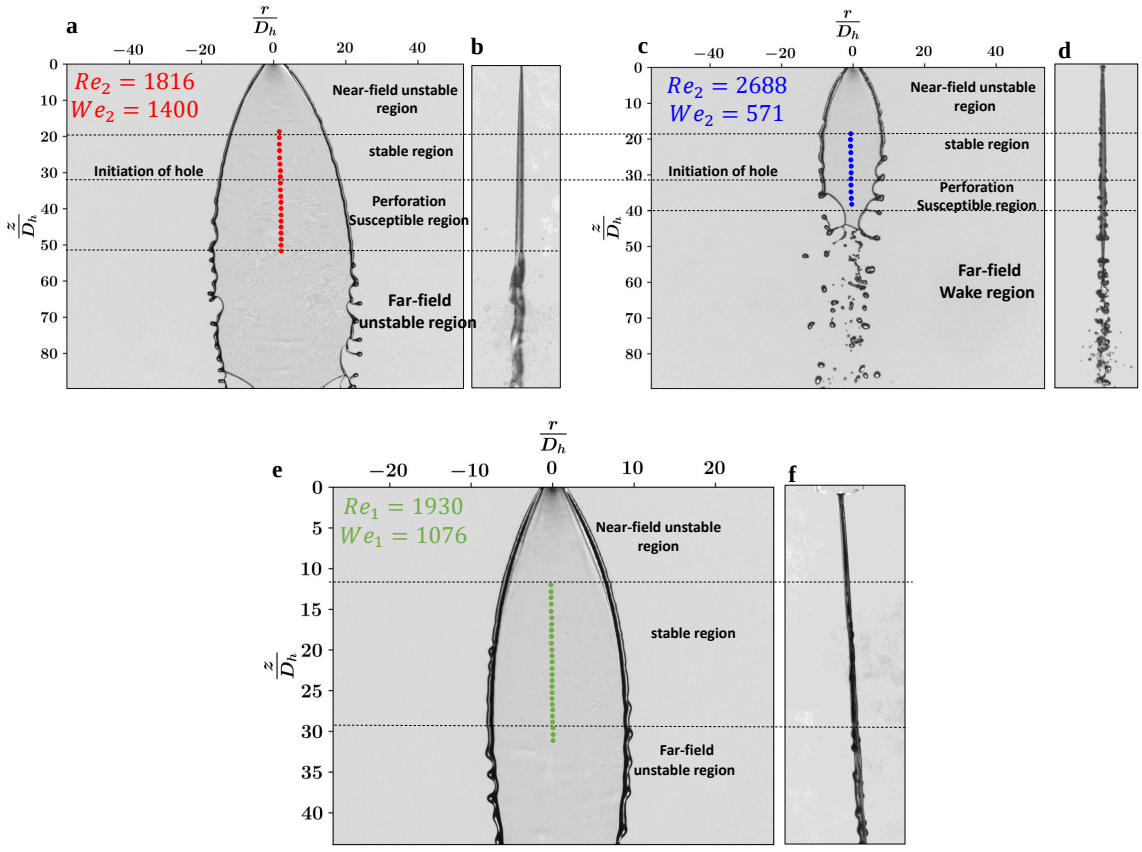

Figure 3.2: Instantaneous front view images of the liquid sheet for (a) $Re_2 = 1816$ (c) $Re_2 = 2688$ (e) $Re_1 = 1930$ and corresponding side view images (b), (d) and (f). The red, blue and green dots represents the measurement location grid for test cases under study. All the experiments are carried out at transverse location $\frac{r}{D_h} = 0$, i.e. along the centerline indicated by top axis of the image

best fitting of lines. It gives the slopes m_1 and m_2 for left and right side respectively. An example of such a result is given in Figure 3.1c. The angle between the straight lines is easily calculated by the geometrical relation:

$$2\alpha_t = \tan^{-1}\left(\frac{m_2 - m_1}{1 + m_1 m_2}\right) \tag{3.2.2}$$

This procedure is similar to the one used by Chen and Lefebvre [163]. The computed values obtained for $2\alpha_t$ and corresponding K_{theo} are given in table 3.1. It is worth noting that α_t is rather far from the 90° indicated by Lechler for the two injector under study. This is due to the smaller flow rate that is used here compared to the flow rate required by the constructor. We further note that α_t increases with the bulk velocity. This means that the higher the bulk velocity, the expanded is the liquid sheet.

3.2.1.3 Statistical convergence of the liquid thickness measurements

For each position in the flow and for each experimental situation, the liquid sheet thickness was measured over $N_{\text{im}} = 1000$ images of the SHG. The calibration (spatio-temporal diagram in air) and post-processing procedures detailed in Chapter 3 were employed for computing the instantaneous value of h from each image. By doing this, we dispose of $N_{\text{im}} = 1000$ values for the thickness allowing a statistical analysis to be performed. The latter consists in computing the ensemble averaged value for h, which is noted with the overbar $\overline{h}$ and writes

$$\overline{h} = \frac{1}{N_{\text{im}}} \sum_{i=1}^{N_{\text{im}}} h_{\text{i}} \tag{3.2.3}$$

The standard deviation for the liquid sheet thickness is defined by

$$h_{\text{rms}} = \sqrt{\frac{1}{N_{\text{im}}} \sum_{i=1}^{N_{\text{im}}} \left(h_{\text{i}} - \overline{h}\right)^2} \tag{3.2.4}$$

We have verified that the averaged value for the liquid sheet thickness was statistically converged. For this purpose, we have first checked that the ensemble averaged light intensity captured by the camera was statistically converged. For a set of N_{im} images with respective intensity $I_1, I_2, \ldots, I_n$ with a standard deviation of σ_I, the evaluation of the mean value calculated from the sample $\overline{I}$ has an associated statistical error $\sigma_{\overline{I}}$ given by:

$$\sigma_{\overline{I}} = \frac{\sigma_I}{\sqrt{N_{\text{im}}}} \tag{3.2.5}$$

Therefore, the more the sample size N_{im}, the less is the statistical error. For a given standard deviation σ_I, reducing the error on the estimate of the mean by a factor of two requires acquiring four times more samples. Contrarily, the larger the fluctuations of the measured quantity are, the larger the statistical error.

The measured light intensity profile for a given position in the flow, a given flow configuration and a given delay line position is depicted in Fig. 3.3. The different curves correspond to different sample size N_{im} from 200 to 1000. Also shown in Fig. 3.3 is the statistical error $\sigma_{\overline{I}}$ which is represented by error-bars. The latter are barely visible in Fig. 3.3 proving that the statistical error made on the mean intensity profiles is very small.

More insights can be provided by plotting the ratio $\sigma_{\overline{I}}/\overline{I}$ for different sample size.

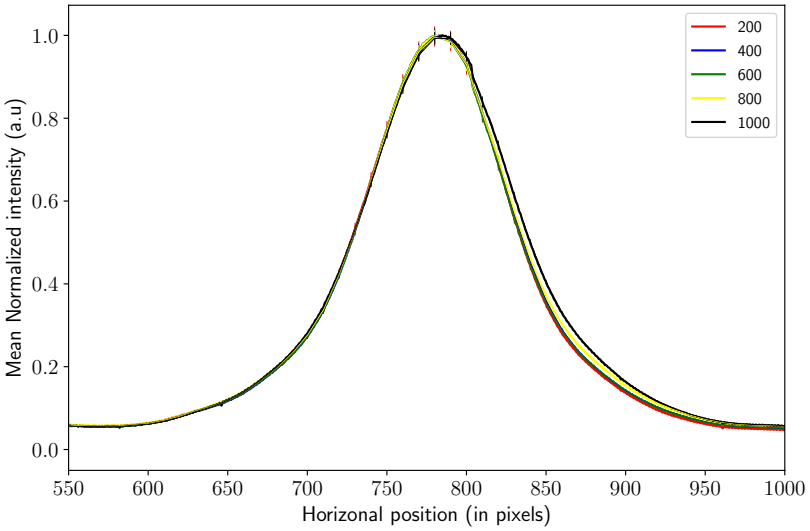

Figure 3.3: The variation of mean normalized intensity for a sampling size of 200, 400, 600,800 and 1000 images. The errorbar represents the standard error $\sigma_{\bar{I}}$ given by equation (3.2.5).

The latter is displayed in Fig. 3.4 for different sample size from 200 to 1000. It can be noticed that the lesser the number of images is, the larger the standard error. For instance, the standard error computed for set of 200 images is $\sim 2.5\%$ whereas for acquisition of 1000 images we obtain $\sim 1.5\%$. These data suggests that 1000 images is enough for the mean intensity profiles to be statistically converged.

Similarly, from the N_{im} instantaneous values of the liquid sheet thickness, we can check that the statistical error that is made on the estimation of $\overline{h}$ is sufficiently small. In Fig. 3.5 is reported the streamwise evolution of the liquid sheet thickness for the three flow configurations explored in the present study. The error-bars corresponding to the statistical error are also displayed. These are only barely visible meaning that the number $N_{\text{im}} = 1000$ is enough for statistics to be converged.

3.2.2 Liquid sheet thickness evolution in the stable regime

We now explore the downstream evolution of the liquid sheet thickness for the various flow configurations. We focus first on the stable liquid sheet regime. Consistently with the theory, the liquid sheet thickness reported in Fig. 3.5 is decreasing with increasing distance from the injector. Note that the values for h are in the range [10,100] μm. Our technique thus appears adequate for measuring rather small values for the liquid sheet thickness. As expected also, the values of h for injector A_1 (the one with larger orifice) are larger than the

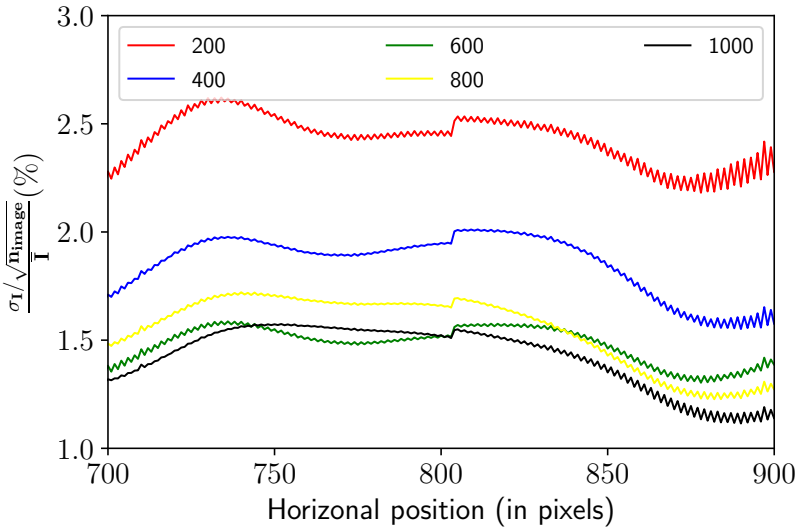

Figure 3.4: The statistical error that is made on mean with a set composed of 200, 400, 600,800 and 1000 images.

ones of injector A_2.

In fig. 3.5, we also displayed the typical fluctuations of the liquid sheet thickness. These are represented by the shaded regions which are given by $\overline{h} \pm h_{\text{rms}}$. We note that for injector A_2, fluctuations are much larger with 20% glycerol concentration compared to the 40% case. This is consistent with the direct visualization of the flow reported in Fig. 3.2 which shows that the rims of liquid sheet are much more corrugated when 20% glycerol solution is used as test fluid. This will be important later when analyzing the perforation holes kinematics.

Figure 3.6 shows the variation of the inverse of the thickness ($\overline{h}^{-1}$) along the sheet centreline z for the two nozzles A_1 and A_2. Note that h and z are non-dimensionalized using the hydraulic diameters D_h. We also report the plots using z and $z - z_0$ as abscissa. The error-bars correspond to the standard deviation ($\text{STD}_{\text{h}^{-1}}$) of the inverse of the thickness estimated as:

$$\text{STD}_{\text{h}^{-1}} = \frac{1}{\overline{h}} \frac{h_{\text{rms}}}{\overline{h}} = \frac{h_{\text{rms}}}{\overline{h}^2} \tag{3.2.6}$$

where h_{rms} is the root mean square (rms) of thickness fluctuations.

It can be discerned that the measured thickness values change only slightly when the flow conditions are varied. We note that for injector A_2, increasing the bulk velocity yields a small decrease of the liquid sheet thickness. The influence of the injector is much more perceptible. We further note that the standard deviation for the inverse of the

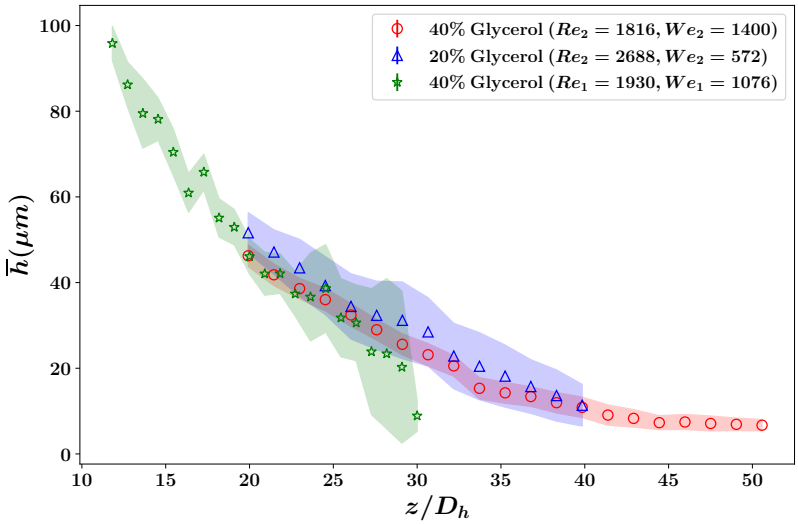

Figure 3.5: Streamwise evolution of the liquid sheet thickness for the three flow configurations explored in the present study. Some errorbars corresponding to the statistical error are also displayed although they are only barely visible. The shaded region depicts the typical fluctuations of the liquid sheet thickness, i.e. $\overline{h} \pm h_{\text{rms}}$.

thickness increases with downstream distance. As we will see later, this is an evidence of an increasingly unstable liquid sheet with the streamwise distance.

As stated previously, a linear relationship should exist between z and $1/h$. The measured thickness values appear to fall along this trend only close to the injector. For atomizer A_1 at $Re_1 = 1930$ the linear evolution of the inverse mean thickness is observed up to $\sim z/D_h = 28$. For atomizer A_2, at $Re_2 = 1816$ and $Re_2 = 2688$, the transition appears at a position $\sim z/D_h = 32$ and $\sim z/D_h = 34$ respectively. In this range of downstream position, we can apply the following linear regression to the experimental data

$$h_{\text{fit}}^{-1} = (z - z_0^{\text{L}})K_{\text{L}}^{-1} \tag{3.2.7}$$

in order to compute K_L and z_0^L numerically[2]. The solid lines in figure 3.6 indicate the linear regression.

Table 3.2 shows a comparison between theoretical (K_{theo}) and measured (K_{L}) thickness parameter for the different flow conditions under study. For obtaining K_{theo}, we have used the measured α_t. Hence, K_{theo} is rather a semi-analytical value. The agreement is very good for injector A_2 which appears as a proof for the adequacy of both the measurement technique and the theoretical prediction of Dombroswski et al. The difference between

[2]The subscript/superscript 'L' referred as linear fit obtained values

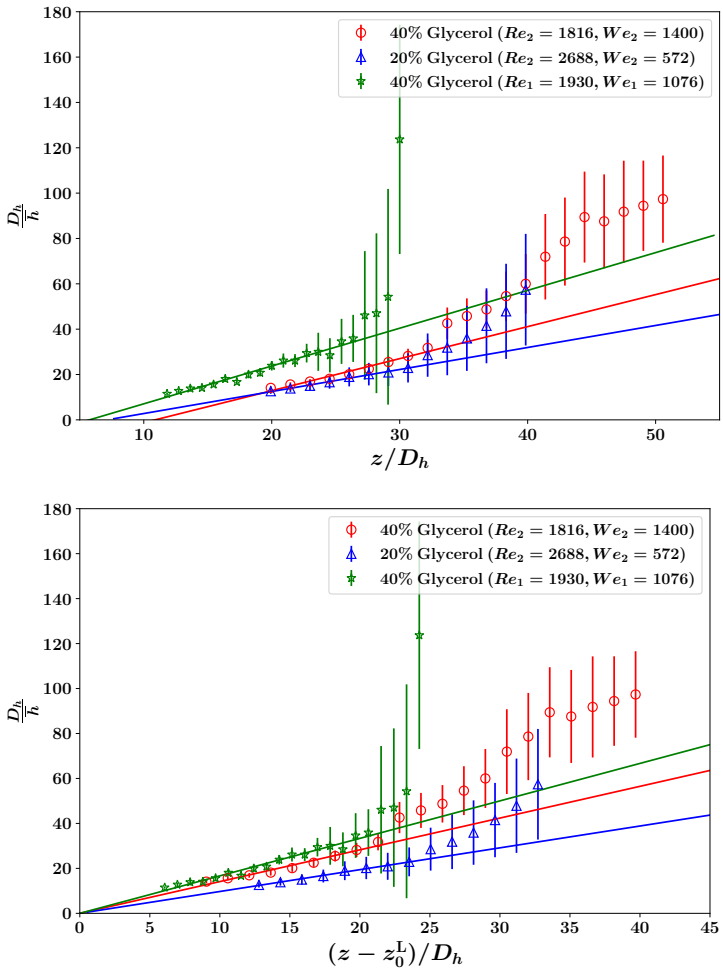

Figure 3.6: Thickness variations along the centerline of the liquid sheet for nozzle A_1 and A_2 for different nozzle dimensions and viscosity values. Solid lines indicate the fitted lines using equation (3.2.7). The errobars correspond to the standard deviation of the inverse of the liquid sheet thickness. In the top figure, h is plotted as a function of z/D_h while in the bottom figure, the abscissa is $(z - z_0^L)/D_h$.

K_{theo} and K_{L} for injector A_1 is larger, i.e. $\sim 25\%$ which is still rather satisfactory.

The virtual origin z_0^{L} which corresponds to the position of the center of pressure in Dombroswski's theory is also reported in table 3.2. We note that the latter does not coincide with the nozzle exit, and is always negative. This means that the center of pressure is located $\sim 4 - 7$ mm upstream of the nozzle exit.

Although Dombroswski's theory applies quite well close to the injector, it appears that as one moves downstream from the nozzle exit, the inverse of the thickness increases more rapidly than expected. This trend has not yet been observed in the literature where a continuous but non-linear increase of the inverse thickness is usually reported [14, 27,

Parameter	$\mathbf{Re_2}$ = **1816** (40%)	$\mathbf{Re_2}$ = **2688** (20%)	$\mathbf{Re_1}$ = **1930** (40%)
K_{L} $(\mu m^{-1}/mm)$	301	438	726
K_{theo} $(\mu m^{-1}/mm)$	325	408	965
$\Delta K_{\mathrm{error}}^{\mathrm{theo-L}}$ (%)	7.3	7.4	25
z_0^{L} (mm)	-7.1	-4.6	-6.3

Table 3.2: Comparison between semi-theoretical K_{theo} and computed K_{L} thickness parameter for different flow conditions under study. We also report the values for the virtual origin z_0^{L} and the sheet angle $2\alpha_t$.

133].

This suggests that another phenomenon is at play. The reasons for this change of slope of h^{-1} could be hypothesized to be related to a sudden change of the flow evolution, or to erratic occurrence of perforations (we will see in next section 3.3) or to corrugations in the liquid sheet. The front and side view images reported in figure 3.2 provide some rationale and possible explanation for the observed change in the thickness distribution. In figure 3.2a-b and 3.2c-d, the stable and smooth region is observed up to $z/D_h \simeq 32$. Beyond $z/D_h \simeq 32$ some appearances of hole nucleation were observed. In consequence the local thickness distribution changes due to which the mean inverse thickness no longer follows the linear trend. For the case $Re_1 = 1930$ (green markers), the stable and smooth region is observed at position $z/D_h \simeq 11$ to $z/D_h \simeq 27$ which corresponds to the region where experimental values perfectly follows the linear relation. In the more downstream region from $z/D_h \simeq 28$ to $z/D_h \simeq 32$ the liquid sheet is likely to be less stable and susceptible for flapping break-up which causes the abrupt change in behavior of the thickness.

It is noticeable that the standard deviation of the thickness distributions increases comparatively for downstream measurement locations. This suggests the liquid sheet becomes less stable at these locations. This is confirmed by visualization of the liquid sheet which appears to be increasingly corrugated as we travel downstream.

3.2.3 Liquid sheet thickness evolution in the unstable sheet

We now investigate the evolution of the liquid sheet thickness in the unstable regime. Figure 3.7 shows the variation of the inverse of the thickness along the centreline of the liquid sheet for nozzle A_1 and 20% glycerol concentration. The solid line indicates the linear fit

of the experimental points and the vertical error-bars correspond to the standard deviation for each downstream measurement location. The figure is separately plotted to show the combine effect of flapping, corrugations and contractions in liquid sheet.

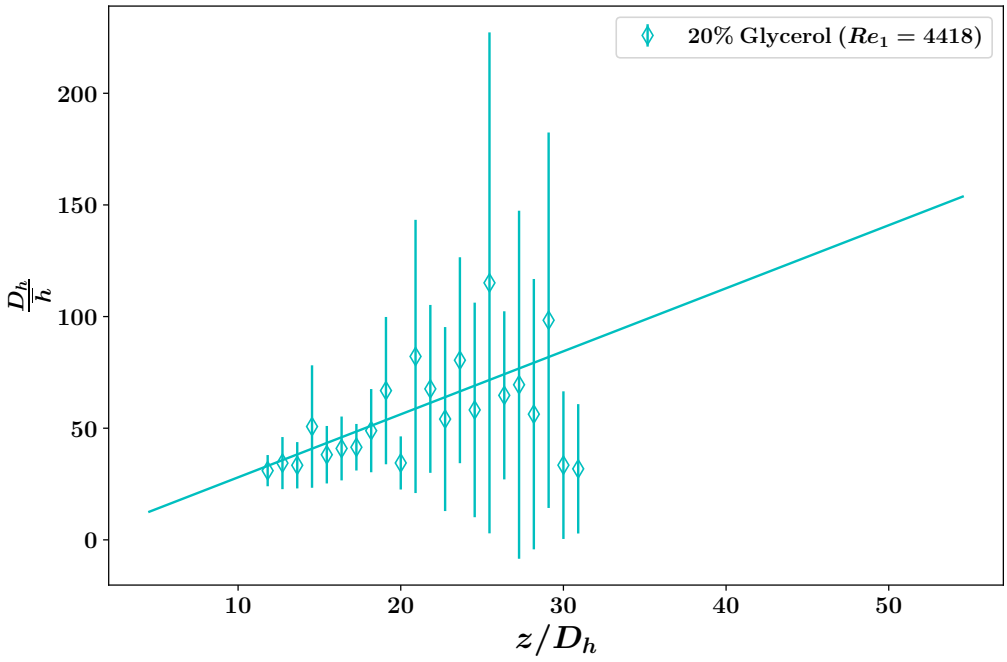

Figure 3.7: Mean thickness variation along the centerline of the liquid sheet for nozzle A_1 and 20% glycerol concentration. Solid line indicates the linear fit (Eq. 3.2.7)

The deviation remains moderate down to $z/D_h \simeq 20$ where the liquid sheet is just corrugated. Further downstream, it increases drastically whereas the mean value does deviate too much from the linear fit. This is linked to the onset of flapping of the liquid sheet. The deviation from a linear evolution is expected since the Dombrowski's model [14] does not take into account the fact that the liquid amassing in the unstable contracting rims is continuously being lost as drops are being ejected as subjets (see figure 3.8). To understand, we recall the figure 1.12, discussed in chapter 2 for stable rims. The continuity equation consists in a set of normal and tangential force balance equations for stable rims.

$$\frac{\partial}{\partial s}(\pi R^2 w) - u_n h = 0 \tag{3.2.8}$$

For unstable rims which are pinching drops and sub-jets, the additional sink term would appear in (3.2.9) as indicated by the second term in LHS to take into account flux of drop

shedding [74].

$$\underbrace{\frac{\partial}{\partial s}(\pi R^2 w)}_{\text{flux accumlated in rim}} + \underbrace{\frac{\partial}{\partial s_d}(4\pi r_d^2 u_d)}_{\text{Drop flux leaving rim}} = \underbrace{u_n h}_{\text{Sheet flux entering rim}} \tag{3.2.9}$$

We respectively note r_d is drop diameter, u_d is drop velocity and s_d is the drop surface area.

Furthermore, the decrease of h^{-1} around $z/D_h = 30$ (increase of the thickness) can be associated to a decrease in the expansion of the liquid sheet.

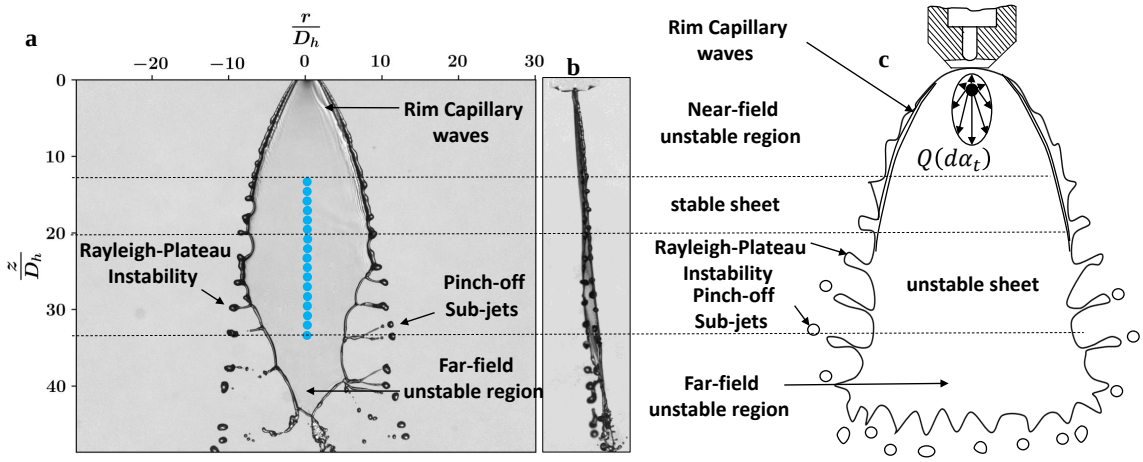

Figure 3.8: Instantaneous (a)front view (b) side view image of the liquid sheet for $Re_1 = 4418$ (c) schematic showing various regions of liquid sheet

3.3 Growth rate of perforation

We now turn our attention to the importance of local liquid sheet thickness in understanding the kinematics of perforation holes appearing on liquid sheet.

The existence and kinematics of perforation holes influence the downstream spray characteristics such as the formed ligament size and hence the drop size distribution, but also the interface velocity etc. For typical flow conditions considered here the perforation originates in the central region of the sheet with an average life-time of the hole $\sim 1.5 - 2$ msec.

An example of perforation hole evolution is shown in figure 3.9. Figure 3.9a shows the frame where the perforation is detected for the first time, and subsequent images from figure 3.9b-3.9o shows its growth with respect to time. Most of the perforations considered

in this work were observed at the lower end of the sheet, i.e. $\sim$ 20 mm (i.e. $\sim 30D_h$) downstream to the nozzle exit. At this position, the time-averaged liquid sheet thickness $\overline{h}$ was around 25-30 μm.

The holes travel approximately 10 to 30 mm before coalescing with the liquid sheet rim (Figure 3.9o) or with another perforation holes to disintegrate into ligaments. These ligaments finally breakup into chain of droplets.

At the highest flow rates perforations can appear in the upper part of liquid sheet and form a web of perforations in the downstream region. This interconnected web of holes forms erratically, making it difficult to visualize and track, even with high speed video cameras. Therefore, in the present study we considered only single perforation hole for which the local liquid sheet thickness is known.

3.3.1 Theoretical considerations

Dombrowski et al. [24] provided a theoretical and experimental analysis for the growth rate of perforation. The complete derivation was reported in section 1.2 (see (1.2.16) to (1.2.20)). It gives the retraction speed of the rim also called the Taylor-Culick velocity [79, 125]:

$$u_p = \sqrt{\frac{2\sigma}{h\rho_l}} \tag{3.3.10}$$

The equation 3.3.10 shows that the growth rate of perforation is independent of r_p and is function of the liquid sheet thickness h. It is considered that h is a function of z only, and h is controlled by one parameter, i.e. K or α_t. If the hole diameter is greater than the thickness of the sheet, the perforation will continue to grow in size. Consequently, the liquid originally contained in the area of the perforation is gathered at the rim. From equation 3.3.10 it is expected that u_p varies with z as a consequence of the non-constant liquid sheet thickness along downstream location. Indeed, from equation 3.2.7, Eq. 3.3.10 can be rewritten as:

$$u_p = \sqrt{\frac{2\sigma(z_d - z_0)}{\rho_l K}} \tag{3.3.11}$$

We immediately note that Eq. (3.3.11) supposes that h is considered constant along the perforation contours. This hypothesis might not be respected if the radius of the perforation covers regions with very different liquid sheet thickness.

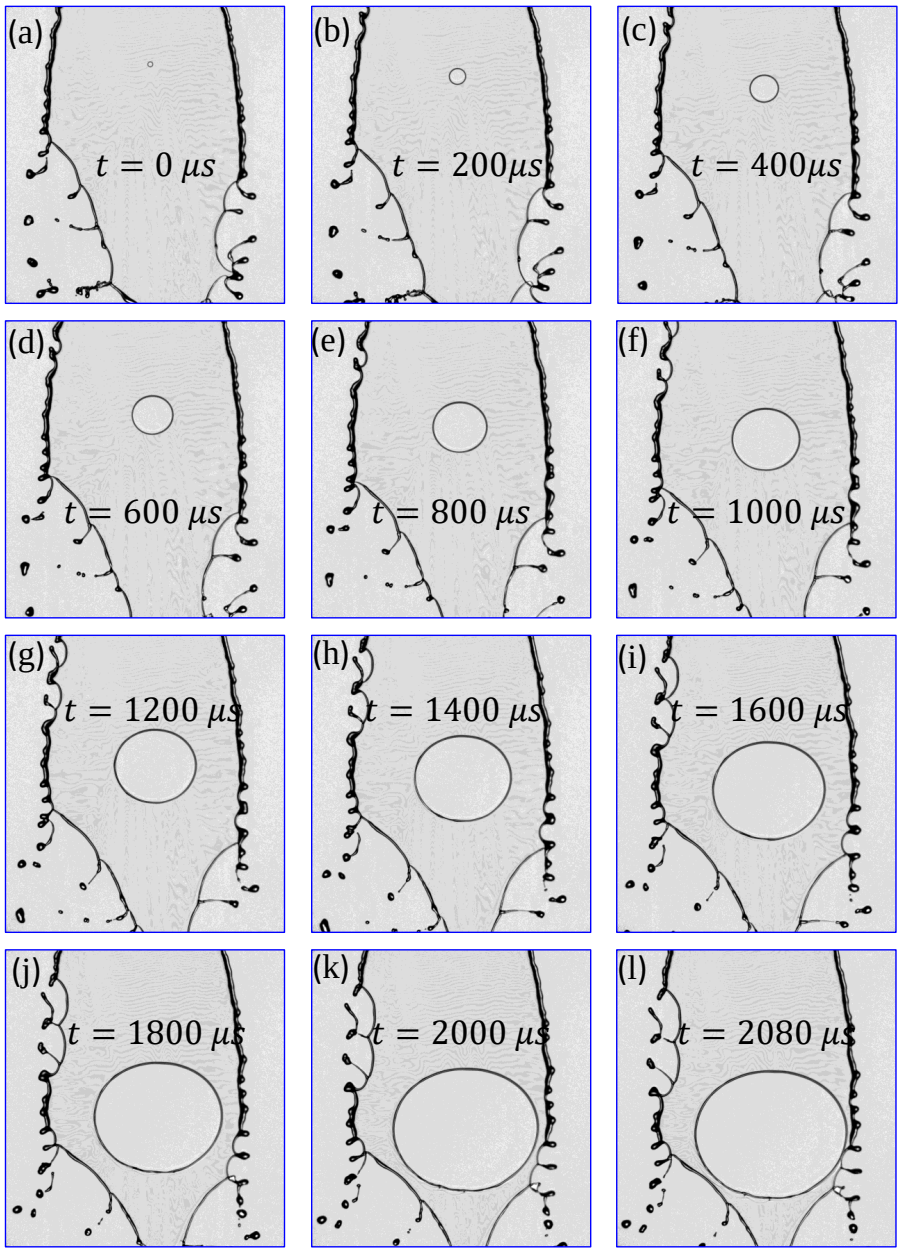

Figure 3.9: Time evolution of single perforation hole at $Re_2 = 2688$

3.3.2 Detection of holes characteristics.

Holes were detected and tracked for two distinct Reynold's numbers $Re_2 = 1816$ and $Re_2 = 2688$ (for which thickness data was also acquired) from high speed videos at frame rates of 25kHz and 80kHz respectively. Hole boundaries from at least 40 and at maximum 100 images were tracked using a homemade Python code. The main steps of the detection and tracking code are (see Figure 3.11):

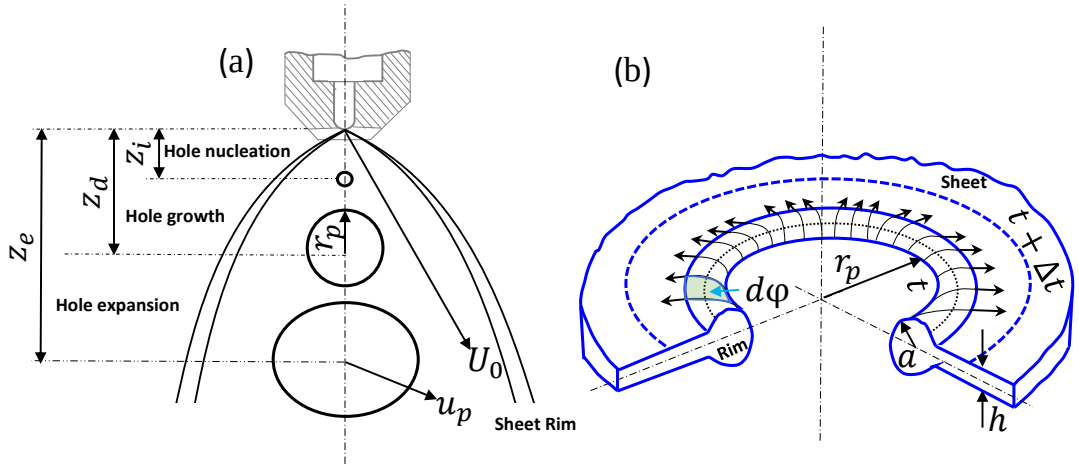

Figure 3.10: (a) Schematic of Successive positions and corresponding phenomena of single perforation (b) Schematic of time evolution of perforation

1. images are loaded into Python and cropped depending on the region of interest required for the hole detection;
2. a two-level image is obtained by a global threshold application
3. the image hole is filled by a morphological operation;
4. a Gaussian blur and mask filter is used to separate out the contours of the hole from sheet.
5. Finally, using contour detection package, the borders of the identified hole is detected and tracked.

This above-mentioned steps yield hole geometrical characteristics such as the perforation area (A_p), perimeter (P_p) and hole centroid vertical position(z_d).

By considering the local retraction speed of the rim u_p we can express the rate of change of the hole area:

$$\oint_c u_p dl = \frac{dA_p}{dt} \tag{3.3.12}$$

The perimeter-averaged growth rate of perforation $\langle u_p \rangle$ is thus given by:

$$\langle u_p \rangle = \frac{1}{P_p} \oint_c u_p dl = \frac{1}{P_p} \frac{dA_p}{dt} \tag{3.3.13}$$

Therefore, $\langle u_p \rangle$ can be directly computed from the time series for $A_p(t)$ and $P(t)$. A more detailed derivation of the different terms in either in equation (3.3.12) or (3.3.13) is

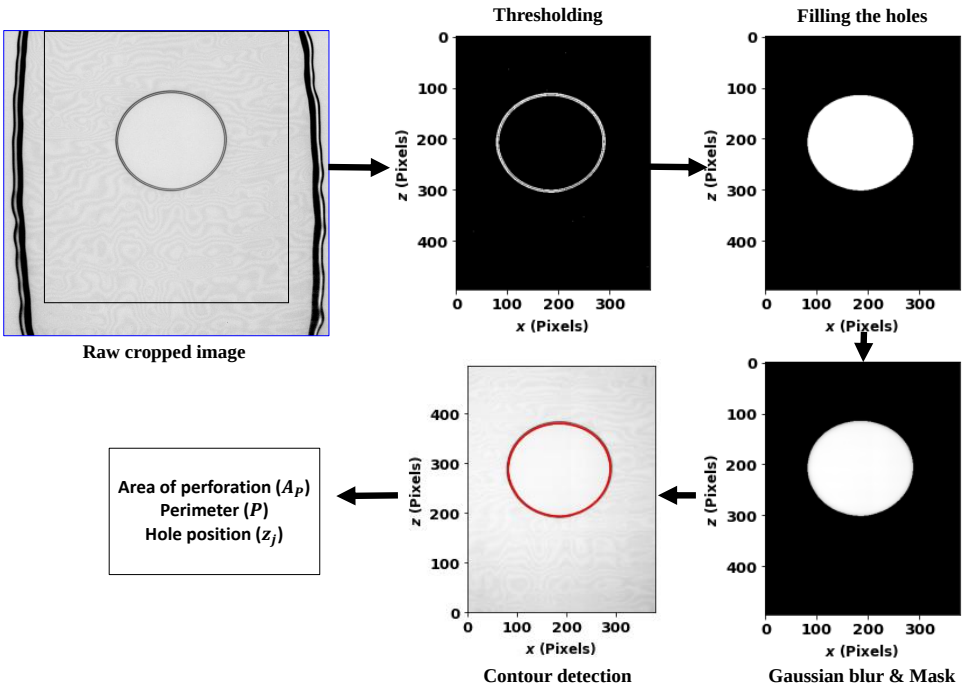

Figure 3.11: Steps involved in detection and tracking of perforation (Note: The read line indicates detected contour)

also documented in appendix C.1.

We can also extract the convection velocity for the hole centroid $z_d(t)$:

$$\dot{z_d} = U_c \tag{3.3.14}$$

Assuming U_c constant in time and space, the position for the hole centroid should be

$$z_d(t) = z_i + t\,U_c \tag{3.3.15}$$

3.3.3 Hole trajectory and convection velocity

The trajectory of the hole centroid is given by the variation of z_d with respect to time, as plotted in figure 3.12. The time (t) is scaled by the convection time obtained from the bulk fluid velocity (U_b) and the hydraulic diameter and is given by $T = D_h/U_b$.

The linear variation of z_d shows that the hole centroid moves at a constant convection velocity. The mean convection velocity of the hole is given by $\overline{U_c} = \overline{\dot{z_d}}$ and can be determined from the slope $z_d(t)$. U_c is found to be equal to 7.06 m/s $Re_2 = 1816$ and 6.65 m/s for $Re_2 = 2688$. The ratio of the convection velocity and the bulk velocity U_b is 0.59

for $Re_2 = 1816$ ($U_b = 11.97$m/s) and 0.86 for $Re_2 = 2688$ ($U_b = 7.73$m/s). This indicates that the more the liquid sheet is expanding, the lower the hole convection relative to the bulk velocity. This can be readily explained by the conservation of mass which yields a smaller streamwise velocity magnitude (relative to the bulk velocity) when the sheet angle at the orifice increases.

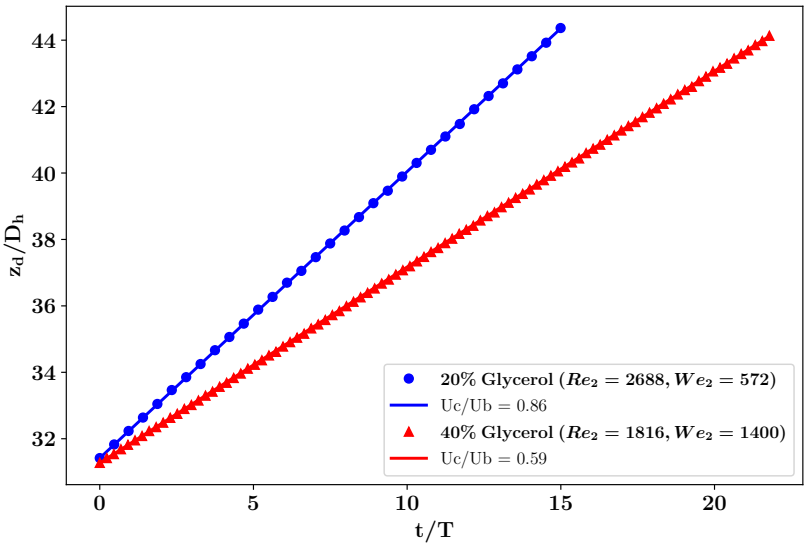

Figure 3.12: Trajectories of hole centroid at $Re_2 = 2688$ and $Re_2 = 1816$.

3.3.4 Hole area and perimeter

Figure 3.13 shows the evolution of hole surface area which obviously increases with time. In both cases, the time variations of A_p resembles a quadratic evolution, which would have been strictly valid for a constant expansion speed. As we will see later, $\langle u_p \rangle$ is increasing in time and hence A_p is lying slightly above a t^2-law. At $Re_2 = 2688$ the area of the hole grows faster than at $Re_2 = 1816$.

The time evolution of the perforation perimeter is plotted in Fig. 3.14. Here the time variation are similar for both cases. All points appear to align roughly on a line, which again would have been strictly valid for $\langle u_p \rangle = const.$. Instead, since $\langle u_p \rangle$ is slightly increasing (this will be shown later), we note that P_p is increasing a bit more rapidly than a t^1-law.

We have also measured the area and perimeter based radius defined as $r_{eq}^A = \sqrt{A_p/\pi}$ and $r_{eq}^P = P/2\pi$ respectively. The ratio $\frac{r_{eq}^P}{r_{eq}^A}$ gives information about circularity of the hole

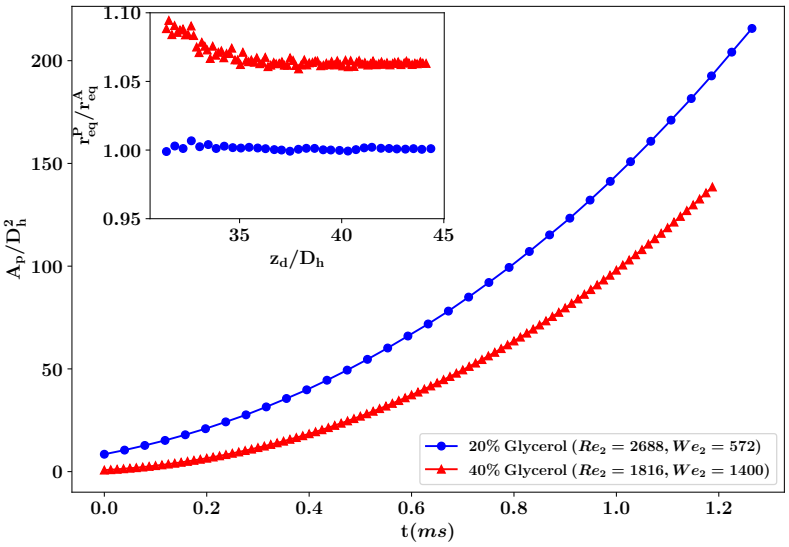

Figure 3.13: Evolution of area of perforation hole w.r.t. time. The inset subplot shows the measure of circularity of holes for $Re_2 = 2688$ and $Re_2 = 1816$.

and is plotted in the inset of Fig. 3.13. We note that for $\mathrm{Re}_2 = 2688$ the perforation hole is almost circular (the ratio is very close to 1) while at $\mathrm{Re}_2 = 1816$, the ratio is in the range 1.05 - 1.1, indicating a slight anisotropy. Moreover, this non-circular hole does not tend to a circular one and remains slightly elongated over the duration of its trajectory. At the lower Reynolds number (higher injection velocity), the liquid sheet expansion is larger (see figure 3.2a). This leads to a more significant stretching of the hole along the transverse direction (see Fig. 3.9) which explains the slightly more elongated form of the puncture at $\mathrm{Re}_2 = 1816$.

3.3.5 Hole expansion velocity

Figure 3.15 shows the expansion velocity $\langle u_p \rangle$ for $\mathrm{Re}_2 = 2688$ and $\mathrm{Re}_2 = 1816$. The mean growth rate of perforation $\langle u_p \rangle$ increases with time. Although the differences are quite small, $\langle u_p \rangle$ is slightly larger at $\mathrm{Re}_2 = 2688$ (smaller bulk velocity and α_t) than at $\mathrm{Re}_2 = 1816$ (larger bulk velocity and α_t).

The evolution of the measured $\langle u_p \rangle$ is compared to the one obtained assuming the Taylor-Culick expression for the expansion velocity and the Dombroswski's expression for the liquid sheet thickness:

$$\langle u_p \rangle = \sqrt{\frac{2\sigma(z_d - z_0^{NL})}{\rho_l K_{NL}}} \tag{3.3.16}$$

Eq. (3.3.16) states that the liquid sheet thickness that is seen by the perforation hole is equal

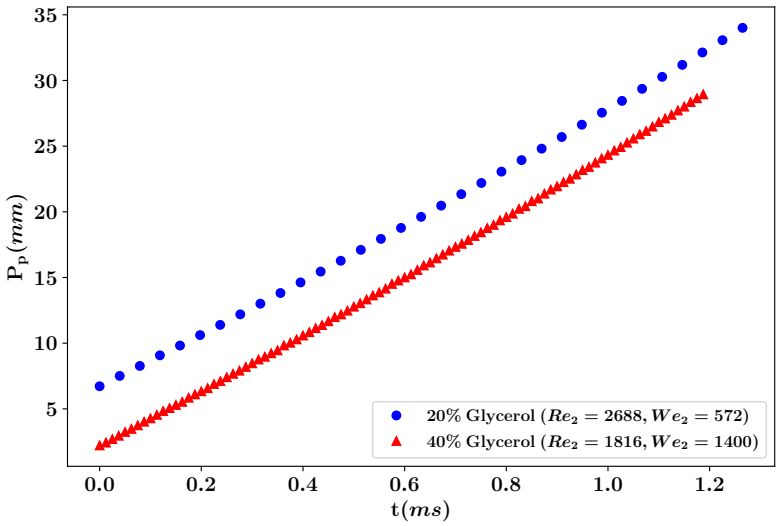

Figure 3.14: Evolution of perimeter of perforation hole w.r.t. time

to the one that would have been present at the perforation centroid z_d. This is of course a rather crude hypothesis given that the puncture radius can be rather large compared to the length-scale of thickness variations. Second, it neglects the fact that h is a fluctuating quantity, although our measurements of the statistics of h reveal that h_{rms} is significant. The parameters z_0^{NL} and K_{NL} can be extracted numerically by fitting Eq. (3.3.16) to measured values of $\langle u_p \rangle$ and compared to the one we obtained previously when $\overline{h}(z)$ was fitted using Dombroswski's expression (Table 3.2).

The results from the fit using Eq. (3.3.16) are displayed by the red and blue full lines in Fig. 3.15. We observe that Eq. (3.3.16) reproduces very nicely our experimental data, suggesting that, at least qualitatively, the Dombroswski-Taylor-Culick theory applies to the perforation kinematics of flat fan liquid sheet in the stable regime. The fitting parameters K_{NL} and z_0^{NL} are given in the table below: For $\text{Re}_2 = 1816$ (the highest bulk velocity),

Parameter	$\mathbf{Re_2}$ **= 1816** (40%)	$\mathbf{Re_2}$ **= 2688** (20%)
z_0^{NL} (mm)	4.2	5.1
K_{NL} $(\mu m^{-1}/mm)$	269	223

Table 3.3: Computed values for K_{NL} and z_0^{NL}.

we note that K_{NL} is in agreement with the one we obtained by fitting $\overline{h}(z)$ (K_L in Table

3.2). The difference between the two estimations is around 10% which is satisfactory. For $\mathrm{Re}_2 = 2688$, the difference is much larger, i.e. about 60%. Even more dramatic is the difference in the virtual origin z_0 which is positive while it was found negative in Table 3.2. We have not yet any explanations for such discrepancies.

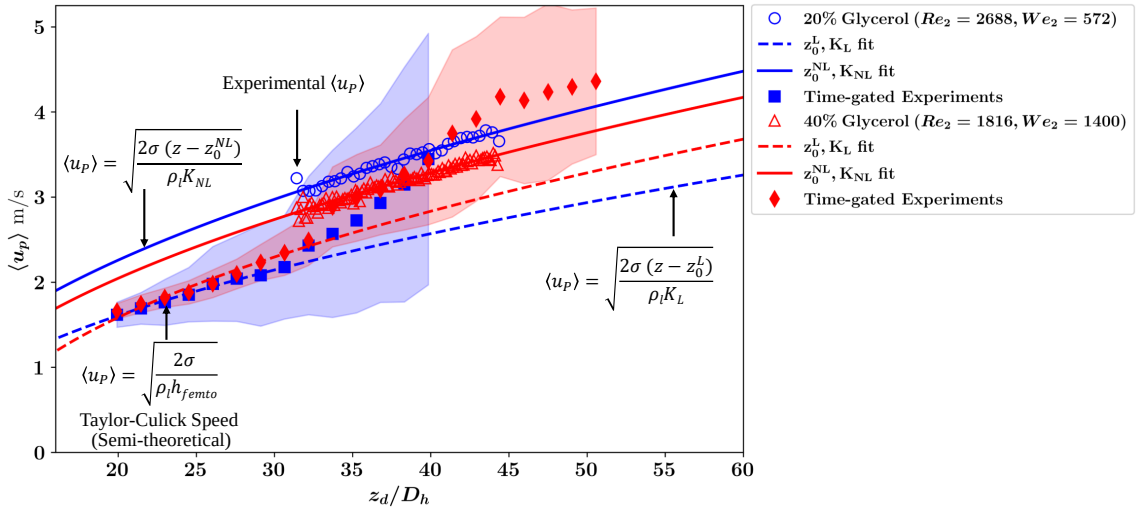

Figure 3.15: Time evolution of the growth rate of perforation for $\mathrm{Re}_2 = 2688$ and $\mathrm{Re}_2 = 1816$. The symbols correspond either to directly measured values (open symbols) or to indirect calculations from the measured thickness values (closed symbols). Also reported are the trends expected from the Taylor-Culick-Dombroswski theory (dashed and full lines).

We can also substitute the previously measured (see section 2.3.3) values for the liquid sheet thickness noted $h_{femto} \equiv \overline{h}$ in the expression of the Taylor-Culick speed:

$$\langle u_p \rangle = \sqrt{\frac{2\sigma}{\rho_l h_{\mathrm{femto}}}}, \tag{3.3.17}$$

and compare to the directly measured values of $\langle u_p \rangle$. Results are displayed in Fig. 3.15, represented by the filled symbols. We also added for enhancing the visual readability of the figure the dashed lines which correspond to Eq. (3.3.16) where the values of K_L and z_0^L reported in Table 3.2 where used in place of K_{NL} and z_0^{NL}.

Qualitatively, the values obtained from Eq. (3.3.17) are consistent with the one directly measured. Interestingly, we note that the appearance of the puncture ($\sim 32 z/D_h$) corresponds to the position where the liquid sheet thickness evolution changes abruptly. This zone corresponds also to the position where fluctuations of h suddenly increase. As it was shown earlier in this manuscript, this behavior was attributed to the onset of an unstable

liquid sheet beyond this location ($\sim 32z/D_h$).

Although qualitatively consistent, we note that the measured values of $\langle u_p \rangle$ is systematically larger than the one expected from the measured evolution of h_{femto}. There is a rather intuitive reason for this difference that lies in the fact that h is a fluctuating quantity. Indeed, it appears rather safe to hypothesize that the probability of perforation increases when the liquid sheet thickness is small. Hence, it is very likely that the instantaneous liquid sheet thickness at the moment when the puncture is forming is smaller than the mean $\overline{h}$. In this condition, the speed at which the puncture is expanding will thus be larger than the one expected from $\overline{h}$. This statement can be given more strength by estimating the expected variations of $\langle u_p \rangle$ knowing the typical fluctuations of h, i.e. h_{rms}. This is presented in Fig. 3.15, where were plotted some shaded regions that correspond to the variations of $\langle u_p \rangle$ that can be computed from the measurements of h_{rms} we performed using the inline-cavity setup. We observe that the directly measured values of $\langle u_p \rangle$ fall perfectly in this interval which reinforces the idea that the puncture forms and propagates when the instantaneous liquid sheet thickness is smaller than the average. We also note that the difference in $\langle u_p \rangle$ between $\text{Re}_2 = 2688$ and $\text{Re}_2 = 1816$ are relatively small, the values at $\text{Re}_2 = 2688$ being systematically larger than those at $\text{Re}_2 = 1816$. This could appear quite counterintuitive since the liquid sheet thickness at $\text{Re}_2 = 2688$ is slightly larger than for $\text{Re}_2 = 1816$. Here again this difference can be explained by the observation that h_{rms} is larger at $\text{Re}_2 = 2688$ compared to $\text{Re}_2 = 1816$ (the visualizations of the sheet portrayed in Fig. 3.2 reveal that it is more unstable at $\text{Re}_2 = 2688$) and hence, there is a larger probability to get a smaller instantaneous value for h and hence a larger $\langle u_p \rangle$. Overall our data reveals that the speed at which the perforation expands is compatible with a thickness value of $\overline{h} - h\text{rms}$ which for the two cases investigated here corresponds to about 20 μm.

3.4 Summary

In this chapter, we have scrutinized the relation between the liquid sheet thickness and the kinematics of perforation. Several outcomes emerge from this study that are listed below:

1. We have obtained reliable measurements of the liquid sheet thickness using the inline cavity time-gated femtosecond technique. The optical setup has been optimized in order to reach a sensitivity of about 1 pixel shift per micro-meter of liquid. This technique and the post-processing procedures allow instantaneous values of h to be

obtained thereby opening the possibility of a statistical analysis. Special care has been taken on the statistical convergence of the data.

2. The streamwise evolution of the liquid sheet thickness was compared to existing theory. It was found that $\overline{h}(z)$ agrees well with Dombrowski's prediction up to certain downstream distance. The liquid sheet parameters (K and z_0) were measured and were found to be in reasonable agreement with Dombrowski's theory.

3. Further downstream, there exists a position where the evolution liquid sheet thickness suddenly departs from Dombroswski's expression. Using visualizations of the flow, we have identified that this position corresponds to the onset of instabilities that destabilize the rim and the entire liquid sheet. This was confirmed by larger standard deviation of the liquid sheet thickness.

4. High-speed back-light illumination experiments were performed with the goal of capturing the expansion of puncture at the same flow conditions. An explicit relationship between the area-weighted growth rate of perforation $\langle u_p \rangle$ and geometrical parameter of holes (A_P, P) was derived and used to characterize the kinematics of perforations and its relation to the local liquid-sheet thickness. The convection velocity was also extracted by tracking the position of the perforation centroid.

5. It was found that perforations occur at the position where the averaged liquid thickness was about 20-25 μm. The expansion velocity $\langle u_p \rangle$ was observed to agree rather well with the Taylor-Culick theory.

6. We have also emphasized that the measured values of $\langle u_p \rangle$ were systematically larger than those expected from the Taylor-Culick expression and the measured time-averaged thickness $\overline{h}$. We have proposed a scenario to explain this discrepancy based on the observed fluctuations of h. This scenario suggests that the perforation occur when the instantaneous liquid sheet thickness is smaller than its average and might thus occur when $h < 25 - 30\ \mu$m. Indeed, our experimental data suggests that a puncture is susceptible to occur when the liquid sheet thickness is $\overline{h} - h_{\mathrm{rms}}$ which for the two cases investigated here yields $h \sim 20\ \mu$m.

Conclusion and perspectives

The main scope of this thesis was: 1) to design and develop optical diagnostic tools for thickness measurement of liquid sheet; 2) to compare evolution of obtained thickness with well established theoretical model and 3) to use the obtained experimental thickness understand the kinematics of erratic peroration hole appearing on liquid sheets.

In a first approach, different complementary and conventional experimental techniques such as backlight imaging and high-speed imaging were implemented in order to characterize the flow. For example, the classical backlight imaging technique utilizing high resolution low frame rate camera and pulsed laser source were first tested on both injectors (Inj. A_1 and Inj. A_2). Across all experiments, various water-glycerol solutions (0-40 % by volume) were used as a working fluid. Using the front and side view images of the liquid sheet images, we first carried out an exploratory qualitative characterization of various stable and unstable regimes of liquid sheet. All the flow structures were consistent with previous observations on impinging jets [16, 21, 22, 74, 107, 112]. Additionally, these backlight illumination images were used to measure the sheet angle and to understand the different phenomenons (such as perforation, contraction of rims, drop-shedding) occurring at different scales of the sheet. To achieve thickness measurement, specific tailored diagnostic tools were designed and implemented to extract information inaccessible using conventional methods. This gives us an opportunity not only to improve the experiments but also to think of ways to obtained experimental data that could be analyzed to extract new quantitative information so as to overpass the limitations of conventional methods. Additionally, enhancement of the contrast of liquid sheet images using developed optical tools was also part of the objectives, and compared with conventional backlight images. The major aims of this thesis, in the context of macroscopic and microscopic quantity characterization of liquid sheet, are summarized in figure 3.16.

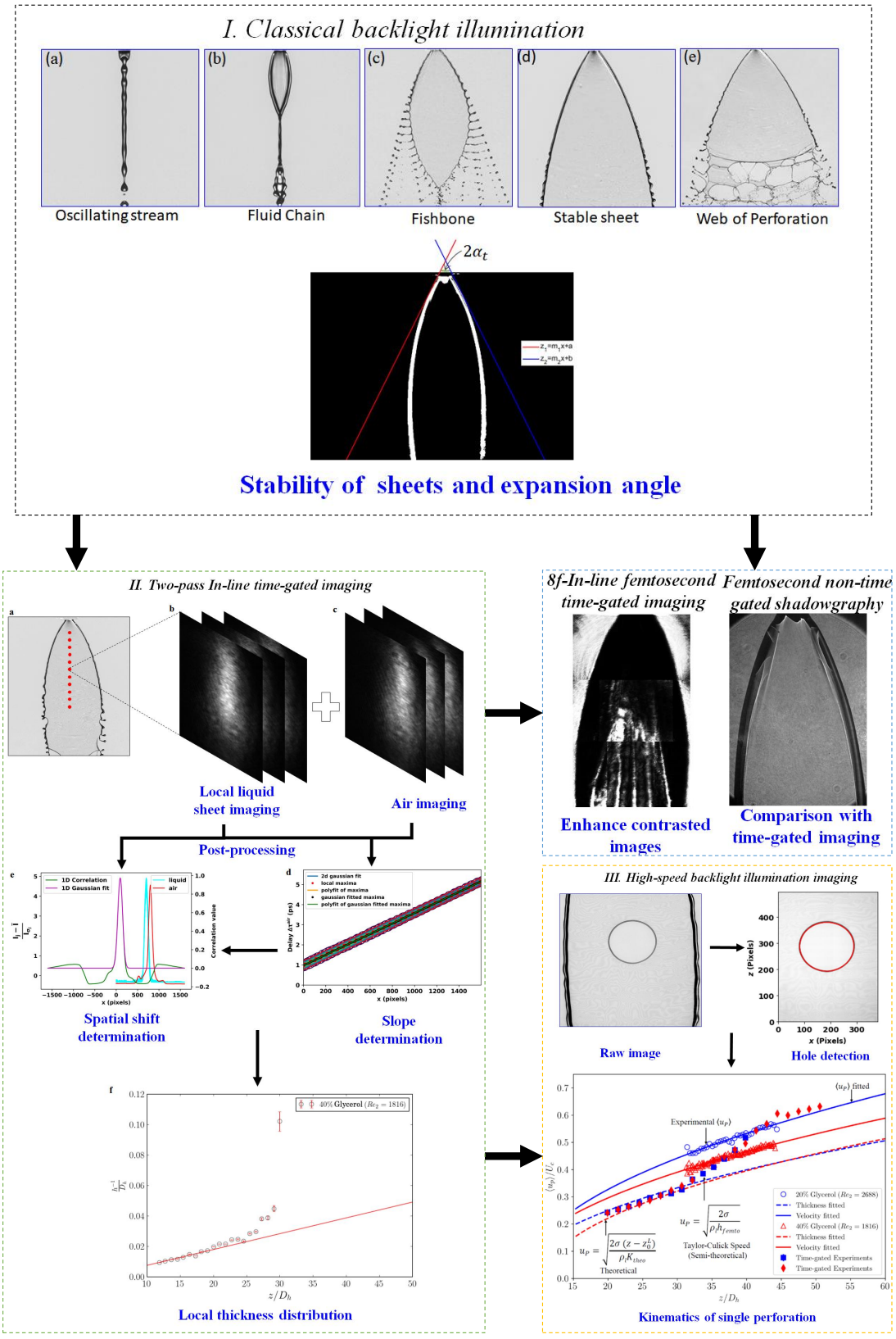

Figure 3.16: Summary of the major aims of the thesis

The design and development of the technique for thickness measurement for semi transparent medium was based on using the potential of SHG time-gate, inspired by ballistic imaging (developed by Idlahcen et.al [30]). We first introduced the single-pass configuration which was used to provide a proof of concept setup, where gating and imaging beams overlap inside BBO crystal to produce SHG signal. We have tested this configuration for its applicability to glass plate. It was shown that the single-pass time-gated imaging setup is capable of separating directly transmitted light and delayed light signal through 140 μm thick glass plate. A few drawbacks have been identified and had to be overcome for this technique to be used for thickness measurement of liquid sheet: (i) spatial shift between air and liquid on the camera is not sufficient to resolve the liquid sheet thickness; (ii) high-levels of noise originating from the high-power pump pulses from the SHG medium in single-pass configuration and (iii) variable optical gate characteristics, both in terms of temporal and spatial resolutions, depending on the angle between the two pulses and on the placement of the SHG medium. As both these characteristics are dependent on the overlapping beams inside SHG medium, the challenge was to make this possible for liquid sheets.

Some improvements have then been proposed with the multi-pass cavity configuration of the optical gate, where the main difference between the two setups is in the method of relaying the imaging beam multiple times to the camera by forming a cavity around the object. The idea of multi-pass is just to increase time delay by a factor 2 between imaging and gating pulse and hence increase the time resolution by a factor 2. Using this configuration, the time-gated images of liquid sheet were recorded by varying the delay between the gating and imaging pulses. This allowed us to obtain a well separated spatial shift between air and liquid sheet. The results obtained with liquid sheet is explained in the appendix B. An important drawback of multi-pass loop based configuration is the reduction in the intensity for each pass of imaging pulse. The output imaging pulse intensity (I_N) after N^{th} pass reduces in geometric progression $I_N = I_I/2^{2N}$ which makes this technique almost unusable for N > 3. Additionally, this configuration can not be used for large field of view of the liquid sheet.

To overcome optical issues in multi-pass cavity configuration, we finally decided to restrict to 2 passes and avoid the imaging beam attenuation using the inline cavity setup. This in-line cavity configuration stands out of other two configurations as it can yield thickness measurements and large field of view of enhanced contrasted images. It

was found that this configuration is simplified even more by removing multiple beam splitters (BSP) and mirrors giving best suited spatio-temporal profiles for measuring the thickness. By adding the telescope in the in-line optical configuration one can obtain enhanced contrasted images of liquid sheet with a large field of view.

Extra refinements could now be added at different levels on the post-processing methods to make thickness measurement simpler and to obtain more accurate computation of the liquid sheet thickness. The full spatio-temporal diagram is no longer needed for measurement on a liquid sheet but only one statistical ensemble of 1000 images for one position of delay is required. Then for each image of this ensemble we can extract spatial shift in pixels (Δx^{camera}) by comparing probed medium and air signal at same delay. The time delay is obtained by $\Delta\tau^{\text{object-air}} = \Delta x^{\text{camera}} \times K_{\text{cal}}$ where K_{cal} is obtained by the slope of the full spatio-temporal diagram in air at a calibration step. This approach gives instantaneous values of thickness which opens perspective towards statistical analysis and minimizes shot to shot variation in images. Thus thickness can be obtained by $h = \frac{c}{\Delta n} K_{\text{cal}}\ \Delta x^{\text{camera}}$. The summary of the various optical configurations designed and developed in this thesis are summarized in Table 3.4.

Table 3.4: Summary of various optical configurations for time-gated imaging of thickness measurement

Optical configurations	**Advantages**	**Disadvantages**
Single Pass	Simple optical setup	May not be appropriate for too small medium thickness
Multi-pass loop	(i) Improved sensitivity (ii) Adjustable number of loops	Reduction of imaging beam intensity
Two-pass in-line cavity	(i) Simpler optical setup (ii) Improved sensitivity	Only two passes possible

Using the thickness results obtained with post-processing methods, we have performed parametric study of thickness distribution and compared it with well established theoretical models. Several outcomes and perspectives emerged out of this study for stable and unstable liquid sheet. For the stable liquid sheet three flow test cases were examined. The obtained evolution of the liquid sheet thickness with the distance from the nozzle exit agrees well literature prediction upto certain downstream distance. An axial attenuation of the thickness is observed during the expansion of the sheet. Also, from the experimental values of thickness it was noticeable that the slope of downstream thickness variation

changes non-monotonically, suggesting that another phenomenon is at play. It was found that this non-monotonic thickness variation mostly occurs in the downstream region where erratic occurrence of perforation and corrugation in liquid sheet were observed, this region being related to the flow conditions.

In this context, after analyzing and validating the thickness values we performed high-speed back light illumination experiments with the goal of capturing holes at the location of measured thickness and at the same flow conditions. Hole contours were tracked from at least 40 and at maximum 100 images using a homemade python code which yields hole topological characteristics such as area of perforation A_P, perimeter P and hole centroid vertical position z_d. In the present study, an explicit relationship between the area-weighted growth rate of perforation $\langle u_p \rangle$ and geometrical parameter of holes (A_P, P) on well defined two-dimensional domain of a hole is proposed. Results show that the mean growth rate of perforation $\langle u_p \rangle$ increases as Reynold number is increased. This is because at higher Reynolds number the convection U_c and bulk velocity U_b is higher, hence the rate of perforation growth is also higher. Additionally, the Taylor-Culick speed is computed based on the measured thickness and validated with analytical expression of Taylor-Culick speed. It is demonstrated that velocity and thickness fields of the holes are correlated and follows the Taylor-Culick law within scatter limit. We find that even though the dissipation due to viscosity is not directly described by Taylor's and Culick's momentum balance, its inclusion does not alter the veracity of our experimental results. This shows that method of calculating area weighted value of growth rate of perforation is more precise because it is valid irrespective of the shape of the hole. Extracting the perimeter and hole area are quite simple and most likely more accurate than extracting minor and major axis of holes.

Future aspects:

As an overall conclusion, our robust experimental method for thickness measurement could be advantageously used to investigate other physical situations where free liquid and stable sheets develop. For instance in-line time gated technique could be applied for different geometries of nozzle such as pressure-swirl atomizer producing hollow cone liquid sheet [164] or water bells [99] where light has to pass two times through curved interfaces. Furthermore, with the knowledge of local liquid sheet thickness one can study different mechanisms of perforations:

1. Complex fluids including dilute emulsions [15, 165] or dilute colloidal suspensions[166] can trigger a perforation mechanism and can be validated with Taylor-Culick law.

2. Temperature inhomogeneities at surface of a sheet can also translate into gradient of surface tension by which a sheet may also rupture. When a laser pulse heats the free surface of an optically absorbing liquid, non-uniform heating induces local surface tension gradients which in turn impart tangential shear stresses causing the fluid motion and transport of heat. The Laser Induced Surface Tension Driven flows (LISTD) [116, 117, 167] is utilized in microfluidic devices as an actuation mechanism which can be well understood with Taylor-Culick law.

3. The mechanism of hole collision that produces very small droplets besides the formation of the standard drops in a fragmentation process [130]. Interestingly, a similar 100 μm drop threshold has been identified in human exhalations like sneezing [168], a fact which clearly underlines its anthropomorphic nature. It is certainly useful to study the emergence of tiny fragments from a general perspective in a different but related context.

Some of the classical imaging techniques (high speed imaging) discussed in Chapter 3 of this thesis can be applied to understand the fishbone structures. Fluid fishbones are characterized by two coupled physical effects: the varicose instability on the rim, and the flapping of the fluid sheet. Both sheet- and rim-driven instabilities [21] can be solved with the well established linear stability theories with the knowledge of liquid sheet thickness.

In chapter 3 section 2.3.2 we discussed shortcomings of multi-pass loop. In this configuration, the reduction in the imaging pulse intensity for each pass of the beam can be avoided by introducing pockel cell and half wave plate inside the cavity loop. A Pockels cell, combined with a half wave plate, can be used for switching between no optical rotation and 90° rotation, creating a fast shutter capable of "opening" and "closing" of the loop for each turn of the beam, which can allow us to avoid intensity reduction of imaging beam. Thus one can set as many passes as it would require to increase the resolution of thickness measurement. Additionally, with this modified configuration one can place the BBO at Fourier plane and can acquire high contrasted images. Further, our femtosecond time-gated imaging technique discussed in Chapter 3, section 2.4 could be applied to obtain a large number of time-gated images of the fully developed fuel sprays. The complex sheet curvature or the spray edges could be studied using shape analysis tools based on the curvature scale space, more common in computer science applications, as discussed in several articles for shape and geometry detection [169, 170].

A | Appendix

Refractive index of glycerol

Glycerol % by weight	Refractive Index n_D^{20}	Difference for 1%	Glycerol % by weight	Refractive Index n_D^{20}	Difference for 1%
100	1.47399	0.00165	50	1.39809	0.00149
99	1.47234	0.00163	49	1.39660	0.00147
98	1.47071	0.00161	48	1.39513	0.00145
97	1.46909	0.00157	47	1.39368	0.00141
96	1.46752	0.00156	46	1.39227	0.00138
95	1.46597	0.00154	45	1.39089	0.00136
94	1.46443	0.00153	44	1.38953	0.00135
93	1.46290	0.00151	43	1.38818	0.00135
92	1.46139	0.00150	42	1.38683	0.00135
91	1.45989	0.00150	41	1.38548	0.00135
90	1.45839	0.00150	40	1.38413	0.00135
89	1.45689	0.00150	39	1.38278	0.00135
88	1.45539	0.00150	38	1.38143	0.00135
87	1.45389	0.00152	37	1.38008	0.00134
86	1.45237	0.00152	36	1.37874	0.00134
85	1.45085	0.00155	35	1.37740	0.00134
84	1.44930	0.00156	34	1.37606	0.00134
83	1.44770	0.00160	33	1.37472	0.00134
82	1.44612	0.00162	32	1.37338	0.00134
81	1.44450	0.00160	31	1.37204	0.00134
80	1.44290	0.00155	30	1.37070	0.00134
79	1.44135	0.00153	29	1.36936	0.00134
78	1.43982	0.00150	28	1.36802	0.00133
77	1.43832	0.00149	27	1.36669	0.00133
76	1.43683	0.00149	26	1.36536	0.00132
75	1.43534	0.00149	25	1.36404	0.00132
74	1.43385	0.00149	24	1.36272	0.00131
73	1.43236	0.00149	23	1.36141	0.00131
72	1.43087	0.00149	22	1.36010	0.00131
71	1.42938	0.00149	21	1.35879	0.00130
70	1.42789	0.00149	20	1.35749	0.00130
69	1.42640	0.00149	19	1.35619	0.00129
68	1.42491	0.00149	18	1.35490	0.00129
67	1.42342	0.00149	17	1.35361	0.00128
66	1.42193	0.00149	16	1.35233	0.00127
65	1.42044	0.00149	15	1.35106	0.00126
64	1.41895	0.00149	14	1.34980	0.00126
63	1.41746	0.00149	13	1.34854	0.00125
62	1.41597	0.00149	12	1.34729	0.00125
61	1.41448	0.00149	11	1.34604	0.00123
60	1.41299	0.00149	10	1.34481	0.00122
59	1.41150	0.00149	9	1.34359	0.00121
58	1.41001	0.00149	8	1.34238	0.00120
57	1.40852	0.00149	7	1.34118	0.00119
56	1.40703	0.00149	6	1.33999	0.00119
55	1.40554	0.00149	5	1.33880	0.00118
54	1.40405	0.00149	4	1.33762	0.00117
53	1.40256	0.00149	3	1.33645	0.00115
52	1.40107	0.00149	2	1.33530	0.00114
51	1.39958	0.00149	1	1.33416	0.00113
			0	1.33303	.....

Figure A.1: Refractive Index of Glycerol at 20° [31](1933)

B | Appendix

B.1 Influence of the angle between the imaging and gating pulse

The power of SHG signal is strongly dependent on angle θ which induces a non-uniform overlap between the two pulses. The angle between imaging and gating pulse was set to $\theta = 10.24°$ for single-pass setup (see section 2.2.3) and to $\theta = 29.92°$ for the two-pass inline cavity setup (liquid sheet thickness measurements, see section 2.3.3). Note that due to the finite size of the involved optics it was not possible to reduce the angle beyond $\theta = 10.24°$. The schematic in Figure B.1 shows the overlap of the two pulses inside the SHG medium at a particular instant of time and how this overlap of two beams at different angles can change the intensity distribution on camera. Due to the small angle between pump and probe, the pulse exhibits greater overlap when compared with larger angle and it has following complications:

- Ideally, reducing θ is an alternate way to reduce the gate duration and is suitable to attenuate delayed light contribution on detector. However, when angle is small, the two collinear SHG from the imaging pulse and from the gating pulse are very close to each other. This reduces the image resolution due to inhomogeneous transmission of spatial frequencies.
- Due to small angle the spatial filter (used to separate the collinear SHG from the non-collinear one) and the camera must be located further away from the BBO crystal, inducing image degradation due to a long light propagation in air.
- In general the dependency of angle θ becomes more prominent, as increase in θ increases non-uniform overlap and increases the gate duration but well separates the non-collinear SHG from collinear one.
- In order to improve spatial resolution of the time-gated images the BBO crystal is

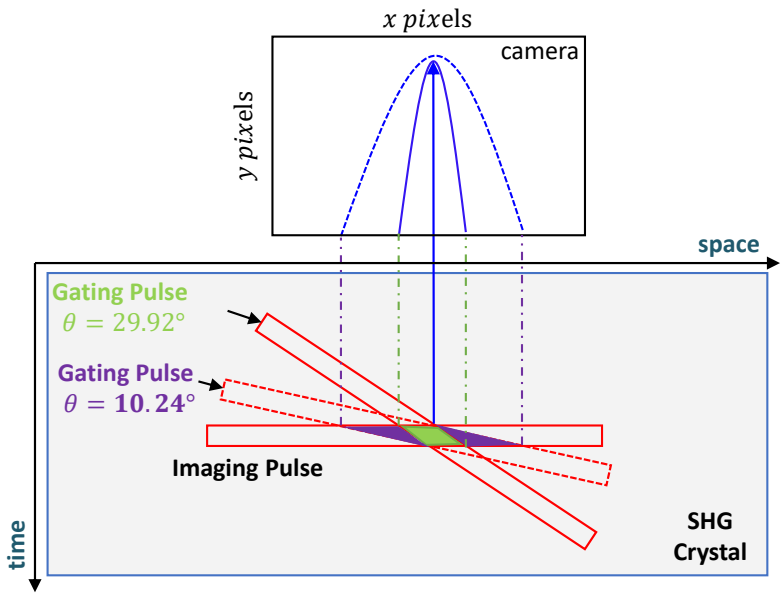

Figure B.1: Schematic of influence of the angle θ between the gating and imaging beams.

placed at image plane, however, there will be lots of unavoidable noise in time-resolved images due to high power pump beam.

The angle $\theta = 29.92°$ is used for all liquid sheet thickness measurement test cases.

B.2 Validation of Vertical shift

To check variations of thickness within the field of view ($\sim$ 10 mm) we carried out the comparison between vertical intensity profile of the images between air and liquid sheet for each particular delay. To do so we divided the 1600 X 1200 pixels in rectangular Region of Interest (ROI) of 250 pixel height (y) in the span of 10 intervals.

The selection of ROI'S made in such way that each ROI overlaps at the center of prior ROI ($y/2$). Next, the intensity profile within ROI is fitted with gaussian profile. As a final step we checked variation of mean and standard deviation (error bars) for gaussian profile for various locations of ROI's as shown in the Figure B.2. The difference between maximum mean beam location of air and sheet is embedded in small sub-plot for each location of ROI's. This phase shift difference shows that the shift appears roughly constant for different vertical position suggesting that the glass plate thickness is nearly constant within the field of view.

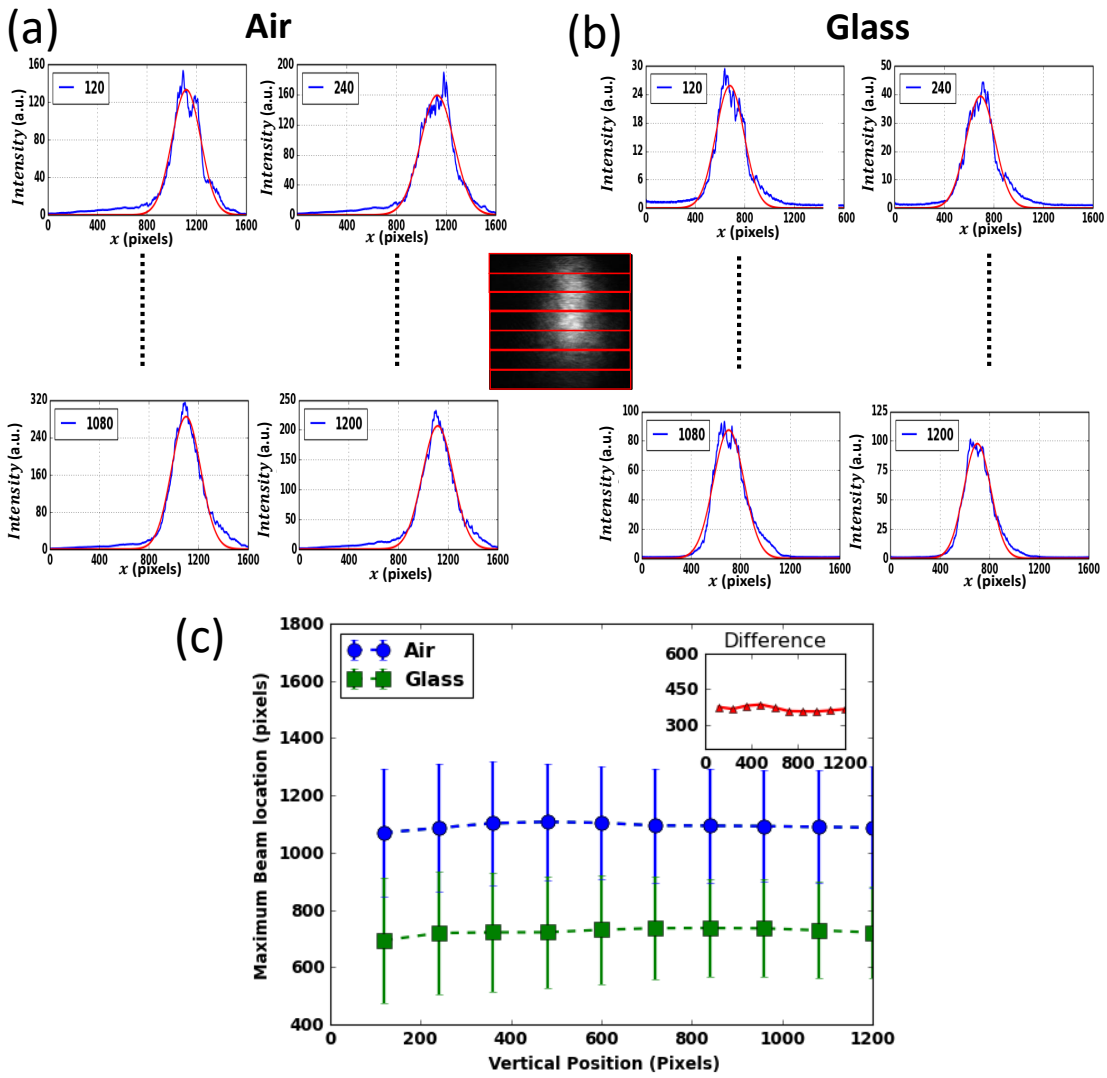

Figure B.2: (Color online)Average intensity profiles (in blue) and best gaussian fit(in red) for (a) Air (b) Glass made 10 profiles with ROI of 250 pixels (c) variation of mean and standard deviation (error bars) for Gaussian fits, the subplot shows the maximum beam location difference between air and the glass plate.

B.3 Intercept method: multi-pass cavity

In the chapter 3, section 2.3.1, we have discussed the results obtained for glass plate. However we did not presented the post-processing results of liquid sheet. This appendix contains the representative spatio-temporal analysis for single location in liquid sheet. Initially we have developed intercept method which is another post-processing tool and it yields time delay between object and air by considering full spatio-temporal diagram of object and air. It has several complications which are discussed below and explained why there is need of another post-processing tool. Figure B.3 shows quantitative spatio-temporal diagrams for air (plot B.3a) and for liquid (plot B.3b) using multi-pass cavity configuration (see section 2.3.1). Fixed values of delay between gating pulse and imaging pulse, i.e. $\Delta\tau^{\text{delay}}$ are considered, and for each delay, 10 images are recorded to produce a mean image $I(\Delta\tau^{\text{object-air}}, x, y)$ for a particular delay. Note that during these preliminary experiments using multi-pass cavity configuration, we have recorded only 10 images when imaging pulse passes through liquid sheet. The aim of these experiments was just to check the spatial shift between air and liquid and effect of number of images to get statistically converging solution.

Quantitative analysis is done to estimate an average time delay due to interaction of light and liquid sheet. To find the location of local maximum intensities $I_{max}(\Delta\tau, x, y)$ for various delays, computations are performed using 1) The "brute-force" method 2) The "1D-Gaussian fit" method 3) The "2D-Gaussian fit method". At the end, all are linear fits, however, the first one computes only locations of maximum value of intensity as a reference and latter is based on complete curve fitting of the intensity profile contours to find the location of maximum. The white contours are the gaussian fit modes of intensity w.r.t delay for given x. The spread of different white contours are dependent on threshold over which the Gaussian computations are performed. The different colored lines in figure B.3 represents the regression lines using different methods to obtain the slope and intercept of the intensity contours. Note that the difference between the lines are not clearly visible in figure B.3 and to better visualize the variation between lines see figure B.4. Remark also that when spatio-temporal analysis is done on only 10 images of liquid sheet, the lines does not overlap as should be ideally the case. The figure B.4b shows that the percentage variation in slope for each line is $\sim 1-5\%$

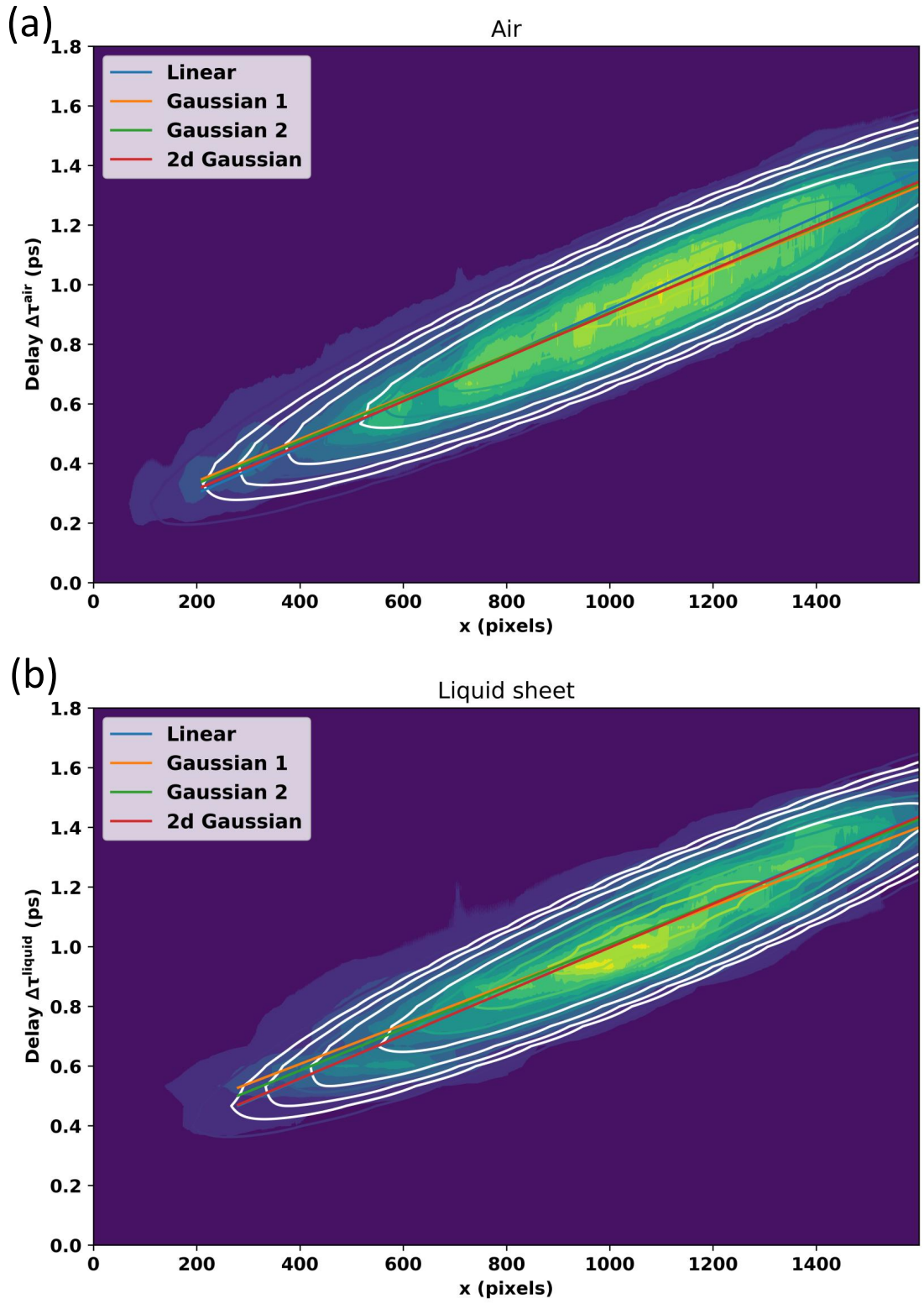

Figure B.3: Spatio-temporal diagram for (a) air and (b) liquid sheet, the results obtained using multipass-cavity configuration.

From a statistical point of view, we need to recapitulate the linear regression equations

for maximum intensity we have discussed in chapter 3. We use linear regression between x and τ, then the linear fit expresses the location of maximum intensity ($I_{max}(x, \tau)$) as a function of x in the form for air :

$$I_{max}(\tau) = mI_{max}(x) + c_a \tag{B.3.1}$$

and for liquid,

$$I_{max}(\tau) = mI_{max}(x) + c_s \tag{B.3.2}$$

Now, if we take a difference between intercept of air and glass plate,

$$\Delta\tau^{\text{liquid}-\text{air}} = c_a - c_s \tag{B.3.3}$$

We obtain an average time delay due to interaction with liquid sheet. For instance, a delay $\Delta\tau^{\text{liquid}}$ was computed for four different methods in liquid:

- 0.235 ps for 1D linear fit of maxima
- 0.244 ps for 1D linear fit of gaussian along delay axis
- 0.237 ps for 1D linear fit of gaussian fitted maxima
- 0.222 ps for 2D gaussian fit

If we take delays only close to maxima of intensity contours the order variation is minimum in the intercepts. The order of variation is maximum for 1D linear fit of gaussian along delay axis which does not particularly considers maximum intensity profiles. Similarly, sub-picosecond delay $\Delta\tau^{\text{liquid}-\text{air}}$, in-terms of the difference between directly transmitted light through air and transmitted light through liquid sheet is estimated numerically by subtracting the c_a and c_s of both spatio-temporal diagrams.

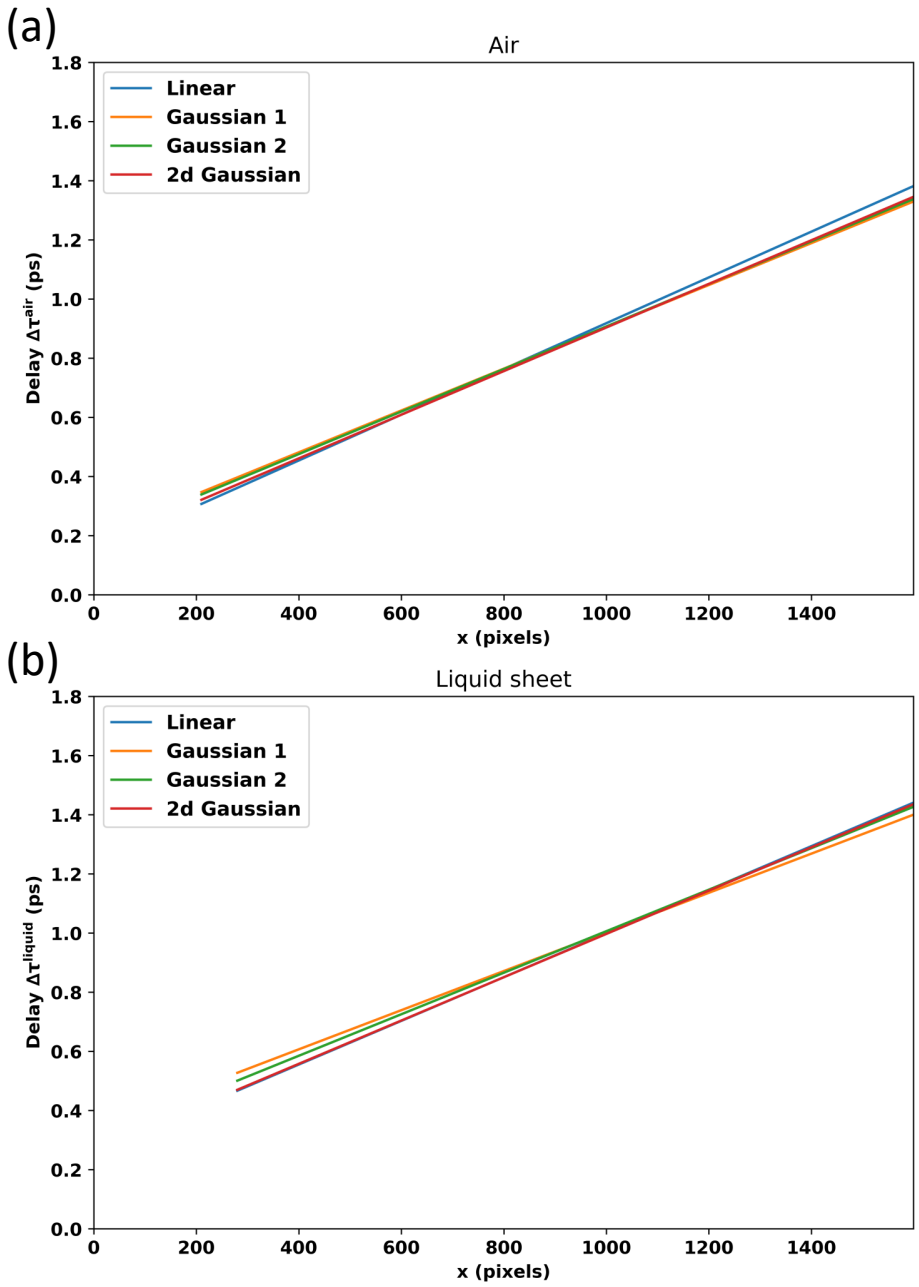

Figure B.4: The figure B.3 is dissected to show the difference between different post-processing methods. (a) air and (b) liquid sheet.

Thus, the thickness of object under study (h) can be obtain:

$$h = \frac{\Delta\tau^{\text{liquid}-\text{air}} c}{2(n_l - 1)} \tag{B.3.4}$$

where n_l is refractive index of liquid sheet.

The intercept method is strongly influenced by the threshold over which the complete gaussian curve fitting is done and have a larger impact on the analysis. Slightly overestimating or underestimating the contours of the experimental data could lead to uncertainty in the thickness of the liquid sheet of the order of $\approx \pm 5 - 10 \mu m$. Although this method is popularly used in image processing for the subpixel peak detection of a point or a line, it does not enable us to make it threshold independent to estimate the statistical parameters. This is why we developed new instantaneous slope based method which is discussed in chapter 3 and applied to the data acquired from inline cavity optical method (see section 2.3.3)

C | Appendix

Instantaneous slope method: In-line cavity

In the chapter 3, section 2.3.3, we have discussed the results obtained for glass plate using in-line cavity optical configuration. However we did not presented the post-processing results of other two test cases $Re_2 = 1816$ and $Re_1 = 1930$ of liquid sheet. This appendix contains the representative steps involved in spatio-temporal and 1D correlation analysis for liquid sheet thickness measurement along the center line in stream wise direction.

Figure C.1 (a & c) shows qualitative spatio-temporal diagrams for air profiles of test cases $Re_2 = 1816$ and $Re_1 = 1930$ respectively. The corresponding quantitative spatio-temporal diagram are shown in figure C.1 (b & d) for computing the slope (noted as A) of the air profile for Reynolds number $Re_2 = 1816$ and $Re_1 = 1930$ respectively.

Figure C.2 shows a three axis plot[3] showing variation in y-averaged intensity between air and liquid signals and a 1D correlation correlation fitted with gaussian fit which calculates correlation lags (displacement in pixels) between air and liquid signals for test cases (a) $Re_2 = 1816$ and (b) $Re_1 = 1930$. Note that the points where a correlation of signal in air and liquid is more than 98% are taken into account, which is a very strict test for calculating correlations. The time delay is obtained by multiplying this spatial shift (in pixels) by the slope A and the thickness is computed as usual once the time delay is known.

[3] the axis for variation in y-averaged intensity between air and liquid signal are on left side of plot and the axis for 1D correlation is on the right side of the plot (marked by arrows) respectively.

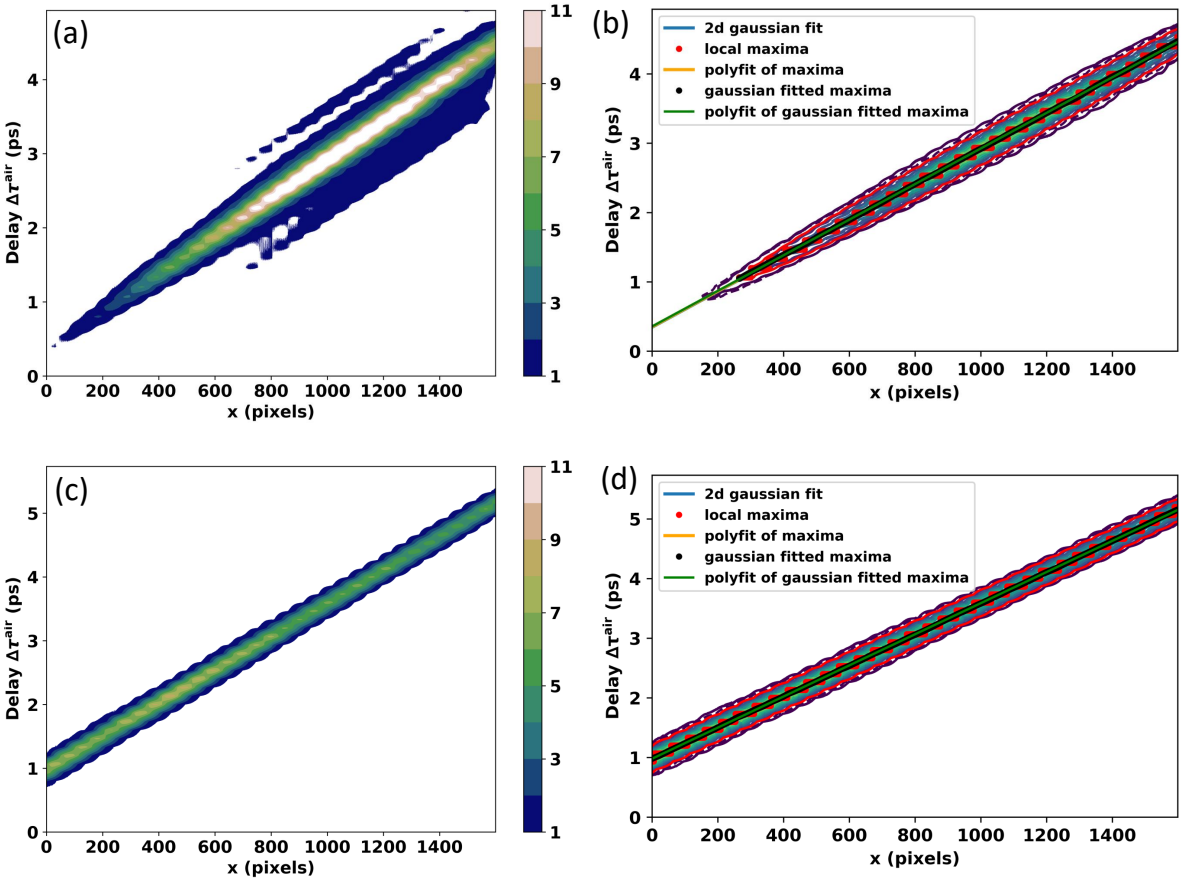

Figure C.1: (a) and (c) qualitative spatio-temporal diagram for air, the color bar represents the measured spatio-temporal evolution of light intensity for Reynolds number $Re_2 = 1816$ and $Re_1 = 1930$ respectively. (b) and (d) quantitative spatio-temporal diagram for computing the slope of the air profile for Reynolds number $Re_2 = 1816$ and $Re_1 = 1930$ respectively.

C.1 Mass budget for growth rate of perforation $\langle u_p \rangle$

We proposed distinct way for assessing the growth rate of perforation as follows. A schematic of control volume V is presented in figure 3.10b. V is decomposed into two volumes, one is the slowly growing toroidal rim of radius $a(t)$ and second is the liquid sheet region of thickness $h(z)$. The liquid is gradually collected from inner disk with the radius $r_p(t)$ into toroidal rim with the volume given by

$$2\pi^2 r_p(t) a^2(t) = \pi r_p^2(t) h \tag{C.1.1}$$

Let us recall some useful geometrical properties of contour revolution by considering an arc element $d\varphi$ of volume dV, length dl, surface area ds and unit vector $\hat{n}$ pointing outward

of the detected rim as shown in figure 3.10b. Applying Reynolds transport theorem on control volume, the general form of continuity equation writes:

$$\frac{d}{dt}\iiint_{\forall} \rho d\forall + \oiint_{s} \nabla.(\rho u_p.\hat{n})ds = 0 \tag{C.1.2}$$

We can approximate equation (C.1.2) with its 2D surrogate by assuming that within the control volume the liquid sheet is smooth so that $|\partial h| \to 0$. From equation (C.1.1) and (C.1.2) the mass conservation on selected incompressible control volume per unit length becomes

$$\frac{d}{dt}\iiint_{\forall} \rho d\forall = \frac{d}{dt}\oiint_{s} ds - \oint_{c} u_p.\hat{n}dl = 0 \tag{C.1.3}$$

Where,

$$\oint_{c} dl = P \tag{C.1.4}$$

The negative sign in the right-hand side of equation (C.1.3) indicates the inflow of flux from intial disk to rim without any outflow of flux from control volume.

The rate of change of area (A_p) and perimeter (P) for each frame can be obtain by simply rotating around the detected contours to form surface revolution. By considering the local retraction speed of the rim u_p we can express the rate of change of the hole area:

$$\oint_{c} u_p dl = \frac{dA_p}{dt} \tag{C.1.5}$$

The perimeter-averaged growth rate of perforation $\langle u_p \rangle$ is thus given by:

$$\langle u_p \rangle = \frac{1}{P}\frac{dA_p}{dt} \tag{C.1.6}$$

It is directly derived from the time series for $A_p(t)$ and $P(t)$ obtained from the measurement on high speed videos.

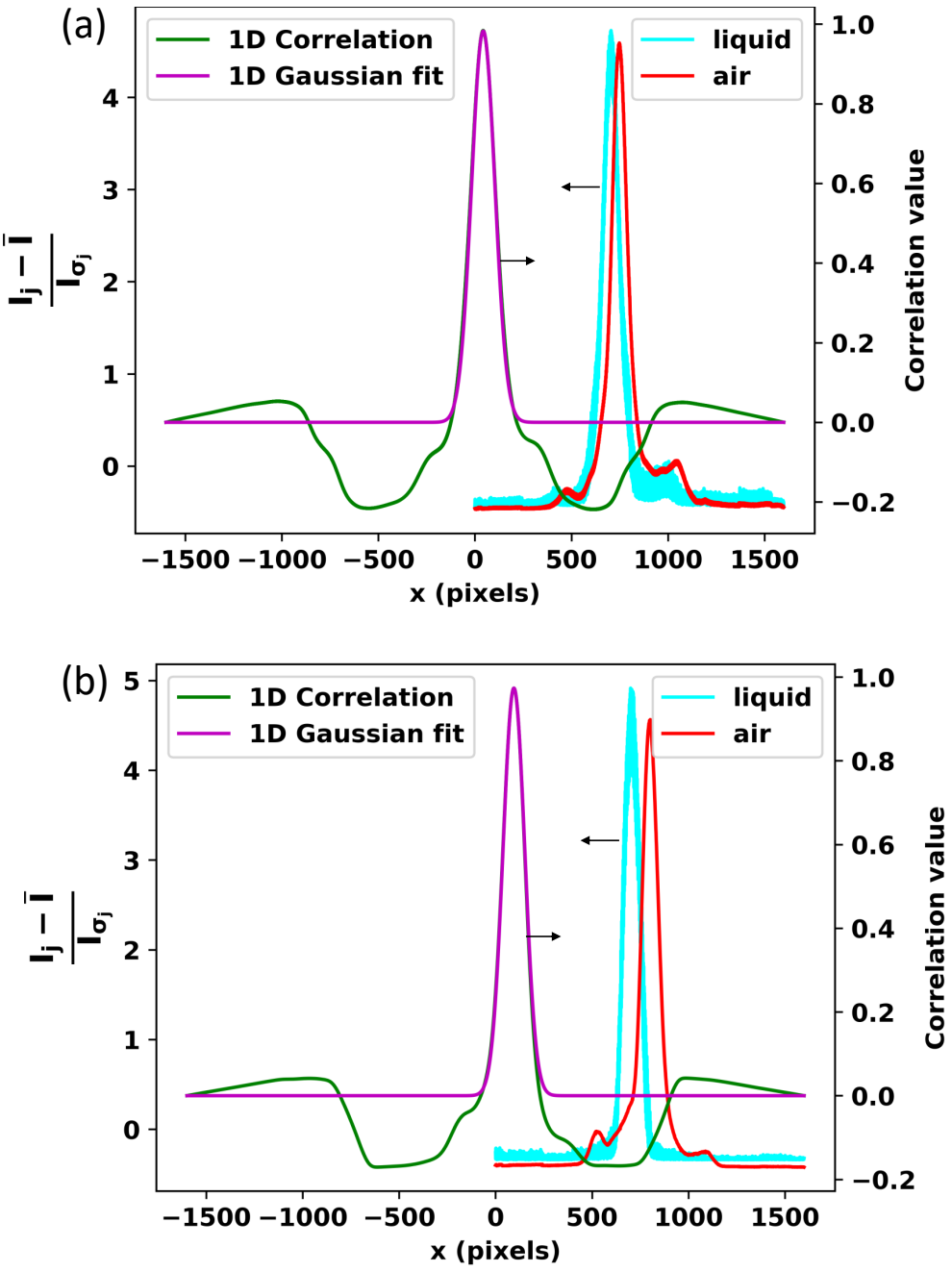

Figure C.2: A three axis plot showing variation in y-averaged intensity between air and liquid signals and a 1D correlation correlation fitted with gaussian fit which calculates correlation lags (displacement in pixels) between air and liquid signals (a) $Re_2 = 1816$ and (b) $Re_1 = 1930$. Note*: the axis for variation in y-averaged intensity between air and liquid signal are on left side of plot and the axis for 1D correlation is on the right side of the plot. (marked by arrows)

Bibliography

[1] Sui Huang. Covid-19: Why we should all wear masks–there is new scientific rationale. *Medium. com*, 2020. (document), 1

[2] Trung-Thanh Vu. *Atomisation process of turbulent liquid sheets: Experimental analyses and numerical developments*. PhD thesis, Normandie Universite, 2017. (document), 1

[3] Harsh Purwar, Hongjie Wang, Mincheng Tang, Saïd Idlahcen, Ammar Hideur, Claude Rozé, Jean-Bernard Blaisot, and Thomas Godin. Development of picosecond fiber laser for high repetition diesel spray imaging. In *13th International Conference on Liquid Atomization and Spray Systems*, 2015. (document), 1

[4] L Neumeister and W Reuter. The eu pesticide blacklist. *Greenpeace*, 2016. (document), 1

[5] Dilip Sanadi, Saïd Idlahcen, Jean-Bernard Blaisot, and Fabien Thiesset. Liquid sheet thickness measurements using multi-pass, time-gated femtosecond imaging. In *International Conference on Liquid Atomization and Spray Systems (ICLASS)*, volume 1, 2021. (document), 1

[6] Robert S Kraemer and Vince Wheelock. *Rocketdyne: Powering humans into space*. AIAA, 2006. (document), 1

[7] Stanislaw Ryszard Massel. *Ocean surface waves: their physics and prediction*, volume 11. World scientific, 1996. (document), 1

[8] D Sindayihebura and C Dumouchel. 3. pressure atomiser: Hole breakup of the sheet. *Journal of Visualization*, 4(1):5–5, 2001. (document), 1, 1.2

[9] David J. Smith. Power-by-the-hour: The role of technology in reshaping business

strategy at rolls-royce. *Technology analysis & strategic management*, 25(8):987–1007, 2013. (document), 1

[10] National Aeronautics and Space Administration (NASA). Interactives – climate change: Vital signs of the planet. https://climate.nasa.gov/interactives/climate-time-machine, October 2021. (document), 2

[11] Nicolas Bremond, Christophe Clanet, and Emmanuel Villermaux. Atomization of undulating liquid sheets. *Journal of Fluid Mechanics*, 585(585):421–456, 2007. (document), 1.1.1, 1.2, 1.2

[12] Y. Wang and L. Bourouiba. Mass, momentum and energy partitioning in unsteady fragmentation. *Journal of Fluid Mechanics*, 935:A29, 2022. (document), 1.2

[13] Robbie Buckingham and John W. M. Bush. Fluid polygons. *Physics of Fluids*, 13(9):S10–S10, 2001. (document), 1.2

[14] Norman Dombrowski, David Hasson, and DE Ward. Some aspects of liquid flow through fan spray nozzles. *Chemical Engineering Science*, 12(1):35–50, 1960. (document), 1.3, 1.1.2, 1.1.2, 1.3, 1.4.2, 1.15, 1.4.2, 3.1, 3.1, 3.2.2, 3.2.3

[15] Norman Dombrowski and RP Fraser. A photographic investigation into the disintegration of liquid sheets. *Philosophical Transactions of the Royal Society of London. Series A, Mathematical and Physical Sciences*, 247(924):101–130, 1954. (document), 1.3, 1.1.2, 1.1.3, 1.2, 1.7, 1.2, 1.2, 1.13, 1.4.1, 1.14, 2.1.3, 1

[16] Nicolas Bremond and Emmanuel Villermaux. Atomization by jet impact. *Journal of Fluid Mechanics*, 549:273, 2006. (document), 1.5, 1.2, 1.3, 1.13, 2.1.3, 3.4

[17] Geoffrey Taylor. Formation of thin flat sheets of water. *Proceedings of the Royal Society of London. Series A. Mathematical and Physical Sciences*, 259(1296):1–17, 1961. (document), 1.5, 2.1.3

[18] V. Kulkarni, D. Sivakumar, C. Oommen, and T. J. Tharakan. Liquid sheet breakup in gas-centered swirl coaxial atomizers. *Journal of Fluids Engineering*, 132(1), 2010. (document), 1.6

[19] Emmanuel Villermaux. Fragmentation versus cohesion. *J. Fluid Mech*, 898:P1, 2020. (document), 1.6, 1.2, 1.3, 1.3

[20] Nikos Savva. *Viscous fluid sheets*. PhD thesis, Massachusetts Institute of Technology, 2007. (document), 1.1.1, 1.6

[21] John W. M. Bush and Alexander E. Hasha. On the collision of laminar jets: fluid chains and fishbones. *Journal of fluid mechanics*, 511:285, 2004. (document), 1.1.1, 1.2, 1.7, 1.2, 1.3, 1.3, 1.12, 1.4.1, 1.14, 2.1.3, 3.4, 3.4

[22] Xiaodong Chen, Dongjun Ma, Vigor Yang, and Stephane Popinet. High-fidelity simulations of impinging jet atomization. *Atomization and sprays*, 23(12), 2013. (document), 1.2, 1.7, 1.13, 2.1.3, 3.4

[23] J. Bico. Cracks in bursting soap films. *Journal of Fluid Mechanics*, 778:1–4, 2015. (document), 1.9

[24] R. P. Fraser, Paul Eisenklam, Norman Dombrowski, and David Hasson. Drop formation from rapidly moving liquid sheets. *AIChE Journal*, 8(5):672–680, 1962. (document), 1.1.2, 1.1.2, 1.1.2, 1.2, 1.3, 1.10, 3.3.1

[25] Baptiste Néel and Emmanuel Villermaux. The spontaneous puncture of thick liquid films. *Journal of Fluid Mechanics*, 838:192, 2018. (document), 1.2, 1.15, 1.4.2

[26] Masato Kondoh and Masaaki Tsubouchi. Liquid-sheet jets for terahertz spectroscopy. *Optics express*, 22(12):14135–14147, 2014. (document), 1.4.2, 1.16

[27] Jake D Koralek, Jongjin B Kim, et al. Generation and characterization of ultrathin free-flowing liquid sheets. *Nature communications*, 9(1):1–8, 2018. (document), 1.4.2, 1.17, 3.2.2

[28] Mark Linne. Imaging in the optically dense regions of a spray: A review of developing techniques. *Progress in Energy and Combustion Science*, 39(5):403–440, 2013. (document), 1.5, 1.18, 1.5

[29] Mark Linne, David Sedarsky, Terrence Meyer, James Gord, and Campbell Carter. Ballistic imaging in the near-field of an effervescent spray. *Experiments in Fluids*, 49(4):911–923, 2010. (document), 1.5, 1.19, 2.2

[30] Saïd Idlahcen, Claude Rozé, Loïc Méès, Thierry Girasole, and Jean-Bernard Blaisot. Sub-picosecond ballistic imaging of a liquid jet. *Experiments in fluids*, 52(2):289–298, 2012. (document), 1.5, 1.5, 1.20, 2.2, 2.5, 3.4

[31] L. F. Hoyt. New table of the refractive index of pure glycerol at 20 C. *Industrial & Engineering Chemistry*, 26(3):329–332, 1934. (document), 2.1.1, A.1

[32] Arthur H. Lefebvre and Vincent G. McDonell. *Atomization and sprays*. CRC press, 2017. (document), 1.1.2

[33] L. Bayvel and Z. Orzechowski. Liquid atomization taylor and francis. *Washington, DC*, 1993.

[34] Christophe Dumouchel. On the experimental investigation on primary atomization of liquid streams. *Experiments in fluids*, 45(3):371–422, 2008. (document), 1.2

[35] Cop26 - united nations conference on climate change. https://unfccc.int/process-and-meetings/conferences/glasgow-climate-change-conference, October 2021. (document)

[36] Frank E Marble. Spacecraft propulsion. 1964. (document)

[37] Andrew J Yule and John J Dunkley. *Atomization of melts: for powder production and spray deposition*. Number 11. Clarendon Press, 1994. (document)

[38] Alex MKP Taylor. Science review of internal combustion engines. *Energy Policy*, 36(12):4657–4667, 2008. (document)

[39] A. J. Hewitt. Spray drift: impact of requirements to protect the environment. *Crop Protection*, 19(8-10):623–627, 2000. (document)

[40] Stefan Kooij, Rick Sijs, Morton M. Denn, Emmanuel Villermaux, and Daniel Bonn. What determines the drop size in sprays? *Physical Review X*, 8(3):031019, 2018. (document)

[41] Tristan Gilet and Lydia Bourouiba. Fluid fragmentation shapes rain-induced foliar disease transmission. *Journal of the Royal Society Interface*, 12(104):20141092, 2015. (document)

[42] Emilia Hilz, Arnoldus W. P. Vermeer, M. A. Cohen Stuart, and F. A. M. Leermakers. Mechanism of perforation based on spreading properties of emulsified oils. *Atomization and Sprays*, 22(12), 2012. (document)

[43] Clara Vernay, Laurence Ramos, and Christian Ligoure. Bursting of dilute emulsion-based liquid sheets driven by a marangoni effect. *Physical review letters*, 115(19):198302, 2015. (document), 1.2

[44] Jacob E. Wilson, Stephen W. Grib, Adnan Darwish Ahmad, Michael W. Renfro, Scott A. Adams, and Ahmad A. Salaimeh. Study of near-cup droplet breakup of an automotive electrostatic rotary bell (esrb) atomizer using high-speed shadowgraph imaging. *Coatings*, 8(5):174, 2018. (document)

[45] J.-G. Swanson and O. Langefeld. Fundamental research in water spray systems for dust control. *Mining Technology*, 124(2):78–82, 2015. (document)

[46] Herman Wijshoff. The dynamics of the piezo inkjet printhead operation. *Physics reports*, 491(4-5):77–177, 2010. (document)

[47] Osman A. Basaran, Haijing Gao, and Pradeep P. Bhat. Nonstandard inkjets. *Annual Review of Fluid Mechanics*, 45:85–113, 2013. (document)

[48] Rajat Mittal, Rui Ni, and Jung-Hee Seo. The flow physics of covid-19. *Journal of fluid Mechanics*, 894, 2020. (document)

[49] John A. Lednicky, Michael Lauzard, Z. Hugh Fan, Antarpreet Jutla, Trevor B. Tilly, Mayank Gangwar, Moiz Usmani, Sripriya Nannu Shankar, Karim Mohamed, Arantza Eiguren-Fernandez, et al. Viable sars-cov-2 in the air of a hospital room with covid-19 patients. *International Journal of Infectious Diseases*, 100:476–482, 2020.

[50] Lydia Bourouiba. Turbulent gas clouds and respiratory pathogen emissions: Potential implications for reducing transmission of covid-19. *Jama*, 323(18):1837–1838, 2020.

[51] Lidia Morawska and Junji Cao. Airborne transmission of sars-cov-2: The world should face the reality. *Environment international*, 139:105730, 2020. (document)

[52] John A. Moriarty and James B. Grotberg. Flow-induced instabilities of a mucus–serous bilayer. *Journal of Fluid Mechanics*, 397:1–22, 1999. (document)

[53] J. P. Duguid. The size and the duration of air-carriage of respiratory droplets and droplet-nuclei. *Epidemiology & Infection*, 44(6):471–479, 1946. (document)

[54] Mark Nicas and Rachael M. Jones. Relative contributions of four exposure pathways to influenza infection risk. *Risk Analysis: An International Journal*, 29(9):1292–1303, 2009.

[55] Lydia Bourouiba, Eline Dehandschoewercker, and John WM Bush. Violent expira-

tory events: on coughing and sneezing. *Journal of Fluid Mechanics*, 745:537–563, 2014. (document)

[56] Nicholas R. Jones, Zeshan U. Qureshi, Robert J. Temple, Jessica P. J. Larwood, Trisha Greenhalgh, and Lydia Bourouiba. Two metres or one: what is the evidence for physical distancing in covid-19? *bmj*, 370, 2020. (document)

[57] Leonardo Setti, Fabrizio Passarini, Gianluigi De Gennaro, Pierluigi Barbieri, Maria Grazia Perrone, Massimo Borelli, Jolanda Palmisani, Alessia Di Gilio, Prisco Piscitelli, and Alessandro Miani. Airborne transmission route of covid-19: why 2 meters/6 feet of inter-personal distance could not be enough, 2020.

[58] Swetaprovo Chaudhuri, Saptarshi Basu, Prasenjit Kabi, Vishnu R Unni, and Abhishek Saha. Modeling the role of respiratory droplets in covid-19 type pandemics. *Physics of Fluids*, 32(6):063309, 2020. (document)

[59] Emmanuel Villermaux, Alexandre Moutte, Muriel Amielh, and Patrice Meunier. Fine structure of the vapor field in evaporating dense sprays. *Physical Review Fluids*, 2(7):074501, 2017. (document)

[60] David A Edwards, Justin Hanes, Giovanni Caponetti, Jeffrey Hrkach, Abdelaziz Ben-Jebria, Mary Lou Eskew, Jeffrey Mintzes, Daniel Deaver, Noah Lotan, and Robert Langer. Large porous particles for pulmonary drug delivery. *Science*, 276(5320):1868–1872, 1997. (document)

[61] Lord Rayleigh. On the capillary phenomena of jets. *Proc. R. Soc. London*, 29(196-199):71–97, 1879. (document), 1.2, 2.1.3

[62] H. B. Squire. Investigation of the instability of a moving liquid film. *British Journal of Applied Physics*, 4(6):167, 1953. (document), 2.1.3

[63] W. W. Hagerty and J. F. Shea. A study of the stability of plane fluid sheets. *Journal of Applied Mechanics*, 1955. (document)

[64] WA Sirignano and C Mehring. Review of theory of distortion and disintegration of liquid streams. *Progress in energy and combustion science*, 26(4-6):609–655, 2000. (document)

[65] GA Ruff, LP Bernal, and GM Faeth. Structure of the near-injector region of nonevap-

orating pressure-atomized sprays. *Journal of Propulsion and Power*, 7(2):221–230, 1991. (document), 1.5

[66] Madan Mohan Avulapati and Ravikrishna Rayavarapu Venkata. Experimental studies on air-assisted impinging jet atomization. *International journal of multiphase flow*, 57:88–101, 2013. (document)

[67] Dilip Sanadi, Kuppuraj Rajamanickam, and Saptarshi Basu. Analysis of hollow-cone spray injected in an unconfined, isothermal, coannular swirling jet environment. *Atomization and Sprays*, 27(1), 2017. (document), 1.1.3

[68] L. Arnone, F. Beretta, A. Tregrossi, A. D'Alessio, and F. Ossler. Ensemble and time resolved light scattering measurements in isothermal and burning heavy oil sprays. In *Symposium (International) on Combustion*, volume 24, pages 1549–1555. Elsevier, 1992. (document), 1.5

[69] Elias Kristensson, Edouard Berrocal, Mattias Richter, and Marcus Aldén. Nanosecond structured laser illumination planar imaging for single-shot imaging of dense sprays. *Atomization and Sprays*, 20(4), 2010. (document), 1.5, 1.5

[70] E Berrocal, E Kristensson, P Hottenbach, G Grünefeld, and M Aldén. Quantitative laser imaging of a non-reacting diesel spray using slipi. *Proc. 23rd ILASS Americas, Ventura, CA*, 2011. (document), 1.5, 1.5

[71] Adel Mansour and Norman Chigier. Dynamic behavior of liquid sheets. *Physics of Fluids A: Fluid Dynamics*, 3(12):2971–2980, 1991. (document)

[72] M Ahmed, N Ashgriz, and HN Tran. Break-up length and spreading angle of liquid sheets formed by splash plate nozzles. *Journal of fluids engineering*, 131(1), 2009.

[73] El-Sayed R. Negeed, S. Hidaka, Masamichi Kohno, and Yasuyuki Takata. Experimental and analytical investigation of liquid sheet breakup characteristics. *International Journal of Heat and Fluid Flow*, 32(1):95–106, 2011. (document)

[74] Emmanuel Villermaux and Christophe Clanet. Life of a flapping liquid sheet. *Journal of fluid mechanics*, 462:341, 2002. (document), 1.2, 1.3, 2.1.3, 3.2.3, 3.4

[75] Christophe Dumouchel, Jean-Bernard Blaisot, Fakhry Abuzahra, Akira Sou, Gilles Godard, and Said Idlahcen. Analysis of a textural atomization process. *Experiments in Fluids*, 60(8):1–16, 2019. (document)

[76] Helne Malot and Jean-Bernard Blaisot. Droplet size distribution and sphericity measurements of low-density sprays through image analysis. *Particle and Particle Systems Characterization: Measurement and Description of Particle Properties and Behavior in Powders and Other Disperse Systems*, 17(4):146–158, 2000. (document)

[77] Félix Savart. Mémoire sur le choc d'une veine liquide lancée contre un plan circulaire. *Ann. chim*, 54(56):1833, 1833. 1.1.1

[78] Geoffrey Ingram Taylor. The dynamics of thin sheets of fluid ii. waves on fluid sheets. *Proceedings of the Royal Society of London. Series A. Mathematical and Physical Sciences*, 253(1274):296–312, 1959. 1.1.1, 1.1.2

[79] Geoffrey Ingram Taylor. The dynamics of thin sheets of fluid. iii. disintegration of fluid sheets. *Proceedings of the Royal Society of London. Series A. Mathematical and Physical Sciences*, 253(1274):313–321, 1959. 1.1.1, 1.1.2, 1.2, 1.2, 3.3.1

[80] G. D. Crapper, N. Dombrowski, W. P. Jepson, and G. A. D. Pyott. A note on the growth of kelvin-helmholtz waves on thin liquid sheets. *Journal of Fluid Mechanics*, 57(4):671–672, 1973. 1.1.1, 1.1.2

[81] Christophe Clanet and Emmanuel Villermaux. Life of a smooth liquid sheet. *Journal of fluid mechanics*, 462:307–340, 2002. 1.1.1

[82] Emmanuel Villermaux, Violaine Pistre, and Henri Lhuissier. The viscous savart sheet. *Journal of Fluid Mechanics*, 730:607–625, 2013. 1.1.1

[83] CJ Clark and N Dombrowski. An experimental study of the flow of thin liquid sheets in hot atmospheres. *Journal of Fluid Mechanics*, 64(1):167–175, 1974. 1.1.2, 1.1.3

[84] N Dombrowski and EA Foumeny. On the stability of liquid sheets in hot atmospheres. *Atomization and Sprays*, 8(2), 1998. 1.1.2

[85] Geoffrey Ingram Taylor. The mechanics of swirl atomizers. In *Seventh International congress of applied mechanics*, volume 2, pages 280–285, 1948. 1.1.3

[86] GI Taylor. The boundary layer in the converging nozzle of a swirl atomizer. *The Quarterly Journal of Mechanics and Applied Mathematics*, 3(2):129–139, 1950. 1.1.3

[87] AM Binnie and D Po Harris. The application of boundary-layer theory to swirling

liquid flow through a nozzle. *The Quarterly Journal of Mechanics and Applied Mathematics*, 3(1):89–106, 1950. 1.1.3

[88] Norman Dombrowski and PC Hooper. The effect of ambient density on drop formation in sprays. *Chemical Engineering Science*, 17(4):291–305, 1962. 1.1.3

[89] Norman Dombrowski and WR Johns. The aerodynamic instability and disintegration of viscous liquid sheets. *Chemical Engineering Science*, 18(3):203–214, 1963.

[90] Norman Dombrowski and David Hasson. The flow characteristics of swirl (centrifugal) spray pressure nozzles with low viscosity liquids. *AIChE Journal*, 15(4):604–611, 1969. 1.1.3

[91] NK Rizk and Arthur Henry Lefebvre. Internal flow characteristics of simplex swirl atomizers. *Journal of propulsion and power*, 1(3):193–199, 1985. 1.1.3

[92] Andrew J Yule and JJ Chinn. Swirl atomizer flow: classical inviscid theory revisited. In *ICLASS 94 Proceedings of the Sixth International Conference on Liquid Atomization and Spray Systems*. Begell House, 1994. 1.1.3

[93] David P Schmidt, Idriss Nouar, PK Senecal, J Rutland, JK Martin, Rolf D Reitz, and Jeffrey A Hoffman. Pressure-swirl atomization in the near field. *SAE transactions*, pages 471–484, 1999. 1.1.3

[94] A Radcliffe. Fuel injection, high speed aerodynamics and jet propulsion. *XID, Princeton University Press, New Jersey, Princeton*, 1960. 1.1.3

[95] AK Jasuja. Atomization of crude and residual fuel oils. 1979. 1.1.3

[96] Arthur H Lefebvre. *Gas turbine combustion*. CRC press, 1998. 1.1.3

[97] JL Santolaya, LA Aisa, E Calvo, I Garcia, and JA Garcia. Analysis by droplet size classes of the liquid flow structure in a pressure swirl hollow cone spray. *Chemical Engineering and Processing: Process Intensification*, 49(1):125–131, 2010. 1.1.3

[98] Alireza Hemmati, Meisam Torab-Mostaedi, Mansour Shirvani, and Ahad Ghaemi. A study of drop size distribution and mean drop size in a perforated rotating disc contactor (prdc). *Chemical Engineering Research and Design*, 96:54–62, 2015. 1.1.3

[99] Christophe Clanet. Waterbells and liquid sheets. *Annu. Rev. Fluid Mech.*, 39:469–496, 2007. 1.1.3, 1.1.3, 3.4

[100] Geoffrey Ingram Taylor. The dynamics of thin-sheets of fluid. i. water bells. *Proceedings of the Royal Society of London. Series A. Mathematical and Physical Sciences*, 253(1274):289–295, 1959. 1.1.3

[101] GN Lance and RL Perry. Water bells. *Proceedings of the Physical Society. Section B*, 66(12):1067, 1953. 1.1.3

[102] Jean-Yves Parlange. A theory of water-bells. *Journal of Fluid Mechanics*, 29(2):361–372, 1967. 1.1.3

[103] Henri Lhuissier and Emmanuel Villermaux. Crumpled water bells. *Journal of fluid mechanics*, 693:508–540, 2012. 1.1.3

[104] Fritz H Bark, Hans-Peter Wallin, Marcus G Gällstedt, and L Peter Kristiansson. Swirling water bells. *Journal of Fluid Mechanics*, 90(4):625–639, 1979. 1.1.3

[105] Marcus F. Heidmann, Richard J. Priem, and Jack C. Humphrey. A study of sprays formed by two impinging jets. 1957. 1.2

[106] N. Dombrowski and P. C. Hooper. A study of the sprays formed by impinging jets in laminar and turbulent flow. *Journal of Fluid Mechanics*, 18(3):392–400, 1964. 1.2, 1.2

[107] Sungjune Jung, Stephen D. Hoath, Graham D. Martin, and Ian M. Hutchings. Atomization patterns produced by the oblique collision of two Newtonian liquid jets. *Physics of Fluids*, 22(4):042101, 2010. 1.2, 2.1.3, 3.4

[108] Ri Li and Nasser Ashgriz. Characteristics of liquid sheets formed by two impinging jets. *Physics of fluids*, 18(8):087104, 2006. 1.2

[109] Emmanuel Villermaux. Fragmentation. *Annu. Rev. Fluid Mech.*, 39:419–446, 2007. 1.2

[110] JJ Cooper-White, JE Fagan, V Tirtaatmadja, DR Lester, and DV Boger. Drop formation dynamics of constant low-viscosity, elastic fluids. *Journal of non-newtonian fluid mechanics*, 106(1):29–59, 2002. 1.2

[111] AV Bazilevskii, JD Meyer, and AN Rozhkov. Dynamics and breakup of pulse microjets of polymeric liquids. *Fluid Dynamics*, 40(3):376–392, 2005. 1.2

[112] Erik Miller, Beau Gibson, Erik McWilliams, and Jonathan P. Rothstein. Colli-

sion of viscoelastic jets and the formation of fluid webs. *Applied Physics Letters*, 87(1):014101, 2005. 1.2, 1.2, 2.1.3, 3.4

[113] Sungjune Jung, Stephen D Hoath, Graham D Martin, and Ian M Hutchings. Experimental study of atomization patterns produced by the oblique collision of two viscoelastic liquid jets. *Journal of non-newtonian fluid mechanics*, 166(5-6):297–306, 2011. 1.2

[114] Henri Lhuissier and Emmanuel Villermaux. Destabilization of flapping sheets: The surprising analogue of soap films. *Comptes Rendus Mecanique*, 337(6-7):469–480, 2009. 1.2

[115] C. Marangoni. Difesa della teoria dell'elasticita superficiale dei liquidi. plasticita superficiale.(continuazione). *Nuovo cimento*, 3:97–115, 1878. 1.2

[116] Jon P Longtin, Kuniyasu Ogawa, et al. Laser-induced surface-tension-driven flows in liquids. *International journal of heat and mass transfer*, 42(1):85–93, 1999. 1.2, 2

[117] H. M. J. M. Wedershoven, C. W. J. Berendsen, J. C. H. Zeegers, and A. A. Darhuber. Infrared-laser-induced thermocapillary deformation and destabilization of thin liquid films on moving substrates. *Physical Review Applied*, 3(2):024005, 2015. 1.2, 2

[118] P. R. Garrett. *Defoaming: theory and industrial applications*, volume 45. CRC Press, 2017. 1.2

[119] Pierre-Gilles De Gennes, Françoise Brochard-Wyart, David Quéré, et al. *Capillarity and wetting phenomena: drops, bubbles, pearls, waves*, volume 336. Springer, 2004. 1.2

[120] Yves Pomeau, Emmanuel Villermaux, et al. Two hundred years of capillarity research. *Physics Today*, 59(3):39, 2006. 1.2

[121] Kimiaki Miyamoto and Yoshinobu Katagiri. Curtain coating. In *Liquid film coating*, pages 463–494. Springer, 1997. 1.2

[122] Lord Rayleigh. Some applications of photography. *Nature*, 44(1133):249–254, 1891. 1.2

[123] Athanase Dupré and Paul Dupré. *Théorie mécanique de la chaleur*. Gauthier-Villars, 1869. 1.2

[124] W. E. Ranz. Some experiments on the dynamics of liquid films. *Journal of Applied Physics*, 30(12):1950–1955, 1959. 1.2

[125] Fred E. C. Culick. Comments on a ruptured soap film. *Journal of applied physics*, 31(6):1128–1129, 1960. 1.2, 1.2, 3.3.1

[126] Nicolas Bremond and Emmanuel Villermaux. Bursting thin liquid films. *Journal of fluid mechanics*, 524:121, 2005. 1.2

[127] Anthony Altieri, Steven Cryer, and Lipi Acharya. Mechanisms, experiment, and theory of liquid sheet breakup and drop size from agricultural nozzles. *Atomization and Sprays*, 24(8), 2014. 1.2

[128] Anthony L. Altieri and Steven A. Cryer. Break-up of sprayed emulsions from flat-fan nozzles using a hole kinematics model. *Biosystems Engineering*, 169:104–114, 2018. 1.2

[129] Ali Asgarian, Martin Heinrich, Rüdiger Schwarze, Markus Bussmann, and Kinnor Chattopadhyay. Experiments and modeling of the breakup mechanisms of an attenuating liquid sheet. *International Journal of Multiphase Flow*, 130:103347, 2020. 1.2, 1.4

[130] B. Neel, Henri Lhuissier, and E. Villermaux. 'fines' from the collision of liquid rims. *Journal of Fluid Mechanics*, 893, 2020. 1.2, 3

[131] David Hasson and Ralph E Peck. Thickness distribution in a sheet formed by impinging jets. *AIChE Journal*, 10(5):752–754, 1964. 1.3

[132] EA Ibrahim and AJ Przekwas. Impinging jets atomization. *Physics of Fluids A: Fluid Dynamics*, 3(12):2981–2987, 1991. 1.3

[133] Y. J. Choo and B. S. Kang. Parametric study on impinging-jet liquid sheet thickness distribution using an interferometric method. *Experiments in fluids*, 31(1):56–62, 2001. 1.4.2, 3.2.2

[134] Y.-B. Shen and D. Poulikakos. Thickness variation of a liquid sheet formed by two impinging jets using holographic interferometry. 1998. 1.4.2

[135] M Hangyo, T Nagashima, and S Nashima. Spectroscopy by pulsed terahertz radiation. *Measurement Science and Technology*, 13(11):1727, 2002. 1.4.2

[136] Yong Yue, Christopher F Powell, Ramesh Poola, Jinn-Chyi Wang, and Johannes K

Schaller. Quantitative measurements of diesel fuel spray characteristics in the near-nozzle region using x-ray absorption. *Atomization and sprays*, 11(4), 2001. 1.5

[137] Alan L Kastengren, Christopher F Powell, Yujie Wang, Kyoung-Su Im, and Jin Wang. X-ray radiography measurements of diesel spray structure at engine-like ambient density. *Atomization and Sprays*, 19(11), 2009. 1.5

[138] Yujie Wang, Xin Liu, Kyoung-Su Im, Wah-Keat Lee, Jin Wang, Kamel Fezzaa, David LS Hung, and James R Winkelman. Ultrafast x-ray study of dense-liquid-jet flow dynamics using structure-tracking velocimetry. *Nature Physics*, 4(4):305, 2008. 1.5

[139] Kyoung-Su Im, K Fezzaa, YJ Wang, Xin Liu, Jin Wang, and M-C Lai. Particle tracking velocimetry using fast x-ray phase-contrast imaging. *Applied physics letters*, 90(9):091919, 2007. 1.5

[140] PA Galland, X Liang, L Wang, PP Ho, RR Alfano, K Breisacher, and L Liou. Time-resolved optical imaging of jet sprays and droplets in highly scattering medium. Technical report, American Society of Mechanical Engineers, New York, NY (United States), 1995. 1.5

[141] Megan Paciaroni and Mark Linne. Single-shot, two-dimensional ballistic imaging through scattering media. *Applied optics*, 43(26):5100–5109, 2004.

[142] Mark Linne, Megan Paciaroni, Tyler Hall, and Terry Parker. Ballistic imaging of the near field in a diesel spray. *Experiments in fluids*, 40(6):836–846, 2006. 2.2

[143] Jacob B Schmidt, Zane D Schaefer, Terrence R Meyer, Sukesh Roy, Stephen A Danczyk, and James R Gord. Ultrafast time-gated ballistic-photon imaging and shadowgraphy in optically dense rocket sprays. *Applied optics*, 48(4):B137–B144, 2009. 1.5

[144] GE Anderson, Feng Liu, and RR Alfano. Microscope imaging through highly scattering media. *Optics letters*, 19(13):981–983, 1994. 1.5

[145] Hiromichi Horinaka, Koji Hashimoto, Kenji Wada, Yoshio Cho, and Masahiko Osawa. Extraction of quasi-straightforward-propagating photons from diffused light transmitting through a scattering medium by polarization modulation. *Optics letters*, 20(13):1501–1503, 1995. 1.5

[146] Stavros G Demos, Harry B Radousky, and Robert R Alfano. Deep subsurface imaging in tissues using spectral and polarization filtering. *Optics Express*, 7(1):23–28, 2000. 1.5

[147] Cécile Calba, Loïc Méès, Claude Rozé, and Thierry Girasole. Ultrashort pulse propagation through a strongly scattering medium: simulation and experiments. *JOSA A*, 25(7):1541–1550, 2008. 1.5

[148] Saïd Idlahcen, Jean Bernard Blaisot, Thierry Girasole, Claude Rozé, and Loïc Méès. Ultra-fast time gated images of a high pressure spray. In *14th International Symposium on Applications of Laser Techniques to Fluid Mechanics, Lisbon, Portugal*, 2008. 1.5

[149] D Sedarsky, M Paciaroni, M Linne, J Gord, and T Meyer. Velocity imaging at the fluid/gas interface of the liquid core in an atomizing spray. *Optics Letters*, 31(7):906e8, 2006. 1.5

[150] Clarence Jay West, Callie Hull, et al. International critical tables of numerical data, physics, chemistry and technology. 1933. 2.1.1

[151] Niels Bohr. Determination of the surface-tension of water by the method of jet vibration. *Philosophical Transactions of the Royal Society of London. Series A, Containing Papers of a Mathematical or Physical Character*, 209(441-458):281–317, 1909. 2.1.3

[152] Dennis Newns, Bruce Elmegreen, Xiao Hu Liu, and Glenn Martyna. A low-voltage high-speed electronic switch based on piezoelectric transduction. *Journal of Applied Physics*, 111(8):084509, 2012. 2.2

[153] Michael D Duncan, Rita Mahon, Lawrence L Tankersley, and J Reintjes. Time-gated imaging through scattering media using stimulated raman amplification. *Optics letters*, 16(23):1868–1870, 1991. 2.2

[154] KM Yoo, Qirong Xing, and RR Alfano. Imaging objects hidden in highly scattering media using femtosecond second-harmonic-generation cross-correlation time gating. *Optics letters*, 16(13):1019–1021, 1991. 2.2

[155] Harsh Purwar, Saïd Idlahcen, Claude Rozé, David Sedarsky, and Jean-Bernard Blaisot. Collinear, two-color optical kerr effect shutter for ultrafast time-resolved imaging. *Optics express*, 22(13):15778–15790, 2014. 2.2

[156] Harsh Purwar, Saïd Idlahcen, Claude Rozé, and Jean-Bernard Blaisot. Time-resolved imaging with oke-based time-gate: enhancement in spatial resolution using low-coherence ultra-short illumination. *arXiv preprint arXiv:1502.07255*, 2015. 2.2

[157] eg PA Franken, Alan E Hill, CW Peters, and G Weinreich. Generation of optical harmonics. *Physical Review Letters*, 7(4):118, 1961. 2.2.1

[158] Valentin G. Dmitriev, Gagik G. Gurzadyan, and David N. Nikogosyan. *Handbook of nonlinear optical crystals*, volume 64. Springer, 2013. 2.2.1

[159] Chuangtian Chen, Bochang Wu, Aidong Jiang, and Guiming You. A new-type ultraviolet shg crystal——β-bab 2 o 4. *Science in China Series B-Chemistry, Biological, Agricultural, Medical & Earth Sciences*, 28(3):235–243, 1985. 2.2.1

[160] David N Nikogosyan. *Nonlinear optical crystals: a complete survey*. Springer Science & Business Media, 2006. 2.2.1

[161] R. R. Alfano. Semiconductors probed by ultrafast laser spectroscopy. volume 1. 1984. 2.3.3

[162] Mark A. Linne. *Spectroscopic measurement: an introduction to the fundamentals*. Elsevier, 2002. 2.4

[163] S Kevin Chen and Arthur H Lefebvre. Spray cone angles of effervescent atomizers. *Atomization and Sprays*, 4(3), 1994. 3.2.1.2

[164] M Suyari and AH Lefebvre. Film thickness measurements in a simplex swirl atomizer. *Journal of Propulsion and Power*, 2(6):528–533, 1986. 3.4

[165] MC Butler Ellis, CR Tuck, and PCH Miller. The effect of some adjuvants on sprays produced by agricultural flat fan nozzles. *Crop protection*, 16(1):41–50, 1997. 1

[166] FO Addo-Yobo, Martin John Pitt, and HA Obiri. The effects of particle size on the mechanisms of atomization of suspensions using hydraulic spray nozzles. *AIChE journal*, 57(8):2007–2024, 2011. 1

[167] Hironori Ohba, Morihisa Saeki, Ikuo Wakaida, Rie Tanabe, and Yoshiro Ito. Effect of liquid-sheet thickness on detection sensitivity for laser-induced breakdown spectroscopy of aqueous solution. *Optics express*, 22(20):24478–24490, 2014. 2

[168] William Firth Wells et al. Airborne contagion and air hygiene. an ecological study

of droplet infections. *Airborne Contagion and Air Hygiene. An Ecological Study of Droplet Infections.*, 1955. 3

[169] Baojiang Zhong, Kai-Kuang Ma, and Jiwen Yang. Curvature scale-space of open curves: Theory and shape representation. In *2013 IEEE International Conference on Image Processing*, pages 3671–3675. IEEE, 2013. 3.4

[170] Farzin Mokhtarian and Alan Mackworth. Scale-based description and recognition of planar curves and two-dimensional shapes. *IEEE transactions on pattern analysis and machine intelligence*, (1):34–43, 1986. 3.4

Titre de la thèse:

ANALYSIS OF LIQUID SHEET THICKNESS AND PERFORATION KINEMATICS USING CONVENTIONAL AND TIME-GATED OPTICAL DIAGNOSTICS

Résumé:

Le présent travail se concentre sur le développement et l'application d'une technique non invasive pour mesurer l'épaisseur d'une nappe liquide plane qui consiste à séparer une impulsion laser de 100 femtosecondes (fs) en une impulsion d'imagerie qui traverse la nappe liquide et une impulsion de déclenchement, qui se déplace uniquement dans l'air. Le retard temporel $\Delta\tau$ entre l'impulsion d'imagerie et de déclenchement est directement proportionnel à l'épaisseur de la nappe liquide h. Ce retard est mesuré à l'aide d'une porte temporelle basée sur la génération de seconde harmonique (SHG). Cette mesure a été appliquée à des nappes liquides planes produites par des buses de pulvérisation à simple trou avec diverses solutions eau-glycérol. La variation de l'épaisseur mesurée de la nappe en aval du point d'injection présente un bon accord avec le modèle théorique de Dombrowski jusqu'à un point correspondant au début des instabilités qui impactent le rebord et puis toute la nappe liquide. La dynamique de la perforation des nappes liquide a aussi été analysée, dans les mêmes conditions d'écoulement. Une relation explicite entre le taux de croissance de la perforation pondéré par la surface $\langle u_p \rangle$ et les paramètres géométriques des trous (A_p, P_p) a été obtenue et utilisée pour caractériser la cinématique des perforations et sa relation avec l'épaisseur locale de la nappe liquide. Un scénario pour expliquer les phénomènes sous-jacents à la perforation est proposé.

Mots clés :

Nappe liquide plane; Epaisseur; Perforation; Nappe stable et instable; Optique non linéaire; Laser femtoseconde; Imagerie rapide.

Abtract:

The present work focuses on the development and application of a non-invasive technique for measuring the thickness of a flat liquid sheet. The technique consists in separating a 100 femtosecond (fs) laser pulse into an imaging pulse which passes through the liquid sheet and a gating pulse, that travels only in air and whose path length can be adjusted using a delay line. The time delay $\Delta\tau$ between the imaging and gating pulse is directly proportional to the liquid sheet thickness h. This delay is measured using Second Harmonic Generation (SHG) based time gate. This technique was applied on flat liquid sheets produced by single-hole fan spray nozzles with various water-glycerol solutions. The streamwise variation of the measured thickness of the sheet exhibits good agreement with the therotical model of Dombrowski up to certain downstream distance from nozzle exit that corresponds to the onset of instabilities that destabilize the rim and the entire liquid sheet. The analysis of the expansion of puncture appearing on the liquid sheets at the same flow conditions was also performed. An explicit relationship between the area-weighted growth rate of perforation $\langle u_p \rangle$ and geometrical parameter of holes (area, perimeter) was derived and used to characterize the kinematics of perforations and its relation to the local liquid-sheet thickness. A scenario to explain underlying phenomena of growth rate of perforation is also proposed.

Keywords:

Flat liquid sheet; Thickness; Perforation; Stable and unstable sheet; Nonlinear optics; Femtosecond laser; High-speed imaging.